PLASMA STUDIES RELATED TO OBSERVATIONS MADE BY IONOSPHERIC 'TOPSIDE SOUNDER' SATELLITES

by

MICHAEL KENNETH ANDREWS

A thesis submitted for the degree
of Doctor of Philosophy in
the University of London

Physics Department Imperial College
London September 1969

Abstract

The work described here relates to investigations made using data from the topside sounder Alouette I. In Part I, from an examination of many transpolar ionospheric electron concentration distributions along tracks of the satellite at a fixed direction to the earth-sun line, it is found that there is an approximately characteristic profile for a given direction. It is suggested that this implies a fixed concentration distribution over the polar regions, under which the earth rotates. If it is assumed that the ionospheric trough at high latitudes is a demarcation between solar-produced ionisation lying inside the plasmasphere and aurorally associated ionisation at high latitudes, the midlatitude termination is the low-latitude wall of the trough. From a study of many topside sounder records obtained during the polar winter, the position of this termination is located at the F peak at all local times, and its motions investigated. When the trough is compared with the position of the plasmapause projected back along field lines, systematic differences in position appear, which are discussed. At higher latitudes, the pattern of ionisation over the winter pole, at least during periods of low solar activity, consists of a torus of enhanced electron density, which corresponds in position to, and is probably caused by, recently measured soft electron fluxes. Some evidence is presented which suggests the outflow of plasma along field lines connected to the geomagnetic tail.

In Part II, the observation and theory of ionogram resonance signals is reviewed, and some experiments are reported which confirm the existence of the cyclotron waves predicted theoretically. The possibilities of using these waves as a diagnostic tool in space, particularly in the measurement of electron temperatures, is considered.

Acknowledgements

I wish to thank Dr. J. O. Thomas for initially suggesting the projects reported here, and for his continuing interest and advice since that time. I would like to acknowledge also the assistance of Dr. T. A. Hall on certain practical aspects of the work described in Chapter 12, and the help of the college staff in the production of the discharge tube used in the experiments.

Financial support has been provided by an Overseas Scholarship awarded by the Royal Commission for the Exhibition of 1851.

Contents

Chapter		Page
1	Introduction	5
	PART I	
2	Earlier Polar Observations	11
3	The Plasmasphere Termination	18
4	Electron Density Distribution above the Winter Pole	37
5	The Effects of Precipitating Particles	52
6	Polar Densities and Universal Time Effects	64
7	Polar Electron Density Profiles	73
8	Conclusion	87
	PART II	
9	Resonance Observations in Space	90
10	Electrostatic Waves in an Infinite Plasma	96
11	Laboratory Experiments: Background	114
12	Laboratory Experiments: Observations	123
13	Applications of Electrostatic Waves	140
Appendix		
I	Numerical Solutions of the Bernstein Dispersion Equation	152
II	The Analysis of Low-density Topside Ionograms	157
	Publications	162
	References	163

1: Introduction

Since the discovery of the ionosphere in the first quarter of the century, it has been recognised that photo-ionisation of the neutral atmosphere by solar ultraviolet radiation would play an important part in its production and maintenance. The solar influence was put on a quantitative basis by Chapman in 1931 with an expression for the production rate of ion-electron pairs. It is this process, when combined with a suitable loss mechanism and allowance for plasma diffusion above an altitude of 200 km, which is today accepted as the mechanism for the formation of the mid-latitude ionosphere. The F_2 layer is produced by ultraviolet radiation of wavelengths between the ionisation limit of oxygen atoms, i.e. 911 Å, and about 170 Å, which is the same band that is responsible for the F_1 layer. The electron density, N, of the former is greater because the loss process, which tends to the linear form βN at F_2 altitudes, decreases upwards faster than does the production rate q. The layer peak forms at an altitude of 250 - 350 km, representing a level above which plasma diffusion and other transport processes become more important than production and loss in determining the electron distribution. The inadequacy of simple solar control of the ionisation at high latitudes, however, is dramatically illustrated by the continuance of the polar ionosphere throughout winter, when the only insolation is at grazing incidence, well above the usual altitude of significant photo-electron production. In spite of this, the electron density remains quite high, and may in fact show increases.

The polar ionosphere in winter then is of particular interest. As the region is closely coupled via field lines to the magnetosphere and solar wind, it appears reasonable that the answer to the question of the origin of the ionosphere should lie partly in this coupling. Recognising

	Alouette I	Explorer XX	Alouette II	ISIS I
Launch	Sep 29 1962	Aug 25 1964	Nov 29 1965	1969
Initial Orbit				
Inclination, deg	80.46	79.9	79.8	88.4
Perigee, km	996.0	866.0	502.0	530.0
Apogee, km	1032.0	1010.0	2982.0	3500.0
Period, min	105.4	103.8	121.4	

Table 1.1 Orbital data of the first four topside sounder satellites.

	ALOUETTE I	EXPLORER XX	ALOUETTE II
Antennas: Sounding	Crossed dipoles	Crossed dipoles	Crossed dipoles
Length tip-tip	75′ and 150′	62′ and 122′	75′ and 240′
Telemetry	Turnstile	Turnstile	
Frequency	Swept, 0·45–11·8 Mc/s at 1 Mc/s²	6 fixed frequencies. Sounding cycle (105 ms) 7·22, 5·47, 3·72, 2·85, 2·0, 1·5 Mc/s, 15 ms each	Swept, 0·2–2 Mc/s (0·15 Mc/s²) 2–14 Mc/s (1 Mc/s²)
Pulse width	100 μs	100 μs	100 μs
Repetition frequency	67 pps	67 pps	30 pps
Peak power	100 W	8–45 W	300 W
Frame period	18 sec	—	30 sec
Telemetry		136 Mc/s 2 W FM (sounder video)	
	Beacon: 136·98 Mc/s 0·25 W 136·08 Mc/s 2 W	Beacon: 137 Mc/s 75 mW CW	
Data acquisition	10 min direct	10 min direct	13 min direct
	read out on ground command		

Table 1.2 Basic electrical data of the sounder experiments in the three satellites from which data are currently available.

this, ground observations of the polar ionosphere have been made for some time, particularly during the IGY. In practice however, the ooverage afforded by these stations was not great, and while the complexity of the various phenomena was revealed by the data, it largely failed in producing a coherent picture of the region, though the auroral programme was a notable exception to this.

Topside sounders have given an enormously improved accessibility to the region, enabling its gross features to be determined, and it is to this that the first part of the thesis is directed. The first satellite carrying a topside sounding experiment, Alouette I, was launched in September 1962, and has been operated continually since that date. Subsequently, other satellites carrying sounders of various types have been placed in different orbits (Table 1.1)

In principle, a topside sounder is identical to a miniaturised ground-based ionosonde, with the crucial difference that its antennas are immersed in the ionospheric plasma. Basic electrical details of the three topside sounders from which data is currently available are given in Table 1.2. In the sounder experiment, a variable frequency pulsed transmitter is used to determine, as a function of frequency, the time taken by a short R.F. pulse to travel the round trip down to its reflection point in the ionosphere and back to a receiver in the satellite. The time delay is converted to an apparent, or virtual depth h', calculated by assuming the wave packet propagates always at the speed of light. The data, i.e. h' as a function of the sounding frequency f, is generally displayed photographically, together with calibration marks for depth and frequency. An Alouette I ionogram, plus a schematic diagram of an ionogram is shown in Fig. 1.1. The sketch illustrates the three normal electromagnetic traces, i.e. the Z-mode (corresponding to the low frequency branch of the extra-ordinary wave), the ordinary and extra-ordinary modes, together with the most commonly seen resonances. The

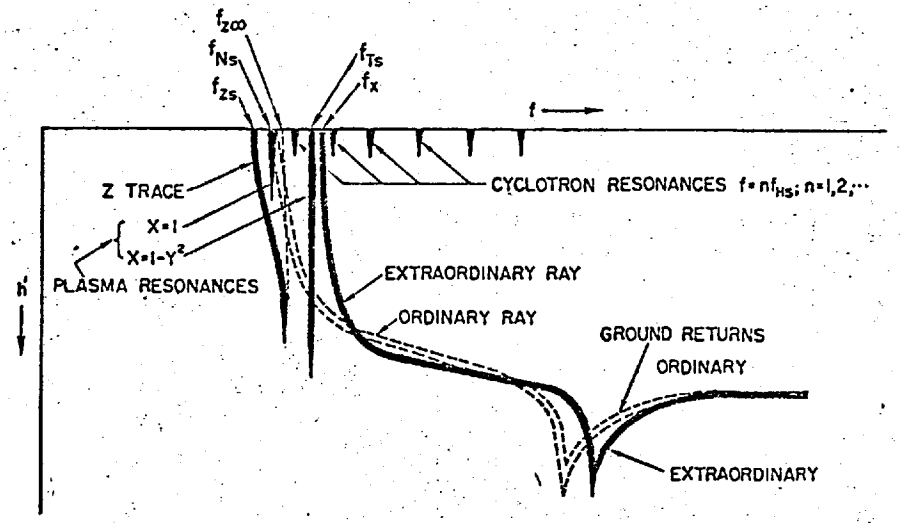


Fig. 1.1a

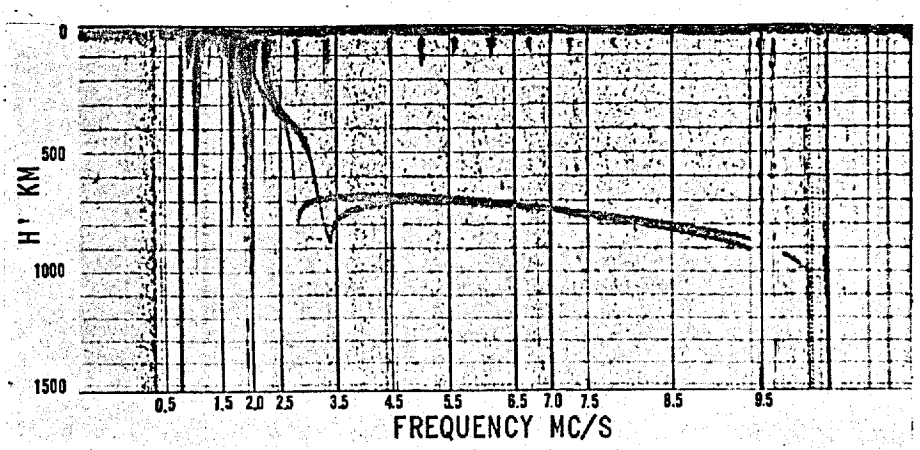


Fig. 1.1b

Fig. 1.1a Schematic diagram of an Alouette I ionogram, showing the apparent depth h' below the satellite at which a pulse of known frequency f was reflected. As well as the usual electromagnetic traces, resonance spikes, considered later, are seen.

Fig. 1.1b An actual, midlatitude ionogram, showing both depth and frequency calibration lines.
(Quito, 2009U.T., 24 Feb, 1963)

term resonance here is used to denote the condition where energy is received for some time immediately after the sounder transmitter is turned off, rather than the usual wave theory definition of an infinity in a wave refractive index. Resonance echoes are then the spike-like traces adjacent to the zero depth axis. The electromagnetic traces are well understood in terms of cold plasma theory and yield information on the ionospheric plasma many kilometres from the vehicle. Employing ionosonde data at polar latitudes, the present work has shown that the plasmasphere may be located at all times in the ionosphere, whilst at higher latitudes, a basic pattern of polar ionisation is present, which is almost certainly caused by the low-energy electron fluxes recently measured. At still higher latitudes, some experimental evidence which suggests the outflow of ionisation, or the "Polar Wind" has been found.

The basic high latitude ionogram data are frequently of poor quality and their interpretation both qualitatively and quantitatively, is often greatly helped by the use of the resonance signals. This has lead to work aimed at achieving a better understanding of resonance phenomena.

A study of the resonances in the second part of the thesis leads to the investigation of a class of electrostatic waves which are readily excited in magnetoplasmas, and which appear to have considerable potential in future space experiments, particularly in the measurement of electron temperatures. With this in mind, some experimental work on the propagation of these waves has been carried out in a laboratory plasma.

The results have been interpreted using an approach based on that of Buckley (1968). Small discrepancies between theory and experiment have lead to some estimates of the effect of streaming suprathermal electrons on the otherwise Maxwellian velocity distribution, and to measurements on sheath effects. It appears that antennas designed to launch electrostatic waves preferentially are possible. Finally, the usefulness

of the waves in space and their advantages over conventional measurements are considered in the last chapter.

PART I

2: Earlier Polar Observations

Before considering the polar ionosphere as seen by topside sounder, it is appropriate to consider briefly what has been learned of the region from ground studies. In a review of the Antarctic ionosphere during the IGY period, Penndorf (1965) was able to write that whilst the Arctic had become better known in the previous ten years, the Antarctic remained more or less unknown. The large literature now existing on the Antarctic ionosphere, primarily from the IGY, appears to have reversed the situation.

In the absence of normal photo-ionisation, there are three possible sources of polar ionisation:-

1. Downward diffusion after photo-production at great altitudes.
2. Horizontal transport from latitudes where densities are high.
3. Production by corpuscular bombardment.

Kamiyama (1966a) has considered the first process, in which most production takes place at an altitude of about 800 km due to the grazing incidence of the sun's rays. By solving the continuity equation for an oxygen atmosphere, it was shown that in equilibrium, a layer with a peak height near 400 km formed. Electron densities above 10^5/cc ($f_0F_2 > 2.8$ Mc/s) were possible for solar zenith angles below 102°, and therefore this process, though certainly present, is not dominant over the winter pole.

Rastogi (1960) concluded from the study of parameters such as layer height and thickness that the unexpected daily variations in the southern high latitude ionosphere were not due to thermal expansion or vertical drifts as had previously been suggested (Ranzi, 1957), but might be a result of horizontal transport of ionisation from lower latitudes. It was supposed that such transport might become significant in an area like the Weddell sea, where the dip angle is particularly low for its geographic

latitude. No drift-inducing mechanism other than density gradients was considered; it would seem that even in such a region of low dip, the transport of ionisation a great distance would require a considerable transport across field lines, suggesting electro-magnetic processes. Indeed, magnetic influence has been recognised for some time, as magnetic co-ordinates are consistently superior in organising polar ionospheric data (Coroniti and Penndorf, 1959).

Drift processes had been suggested by Sato (1959) to explain the shape obtained when instantaneous contours of critical frequency were constructed across the north pole. If this is done, a tongue of higher density plasma is seen to extend into the night hemisphere from the sun-lit side. This was taken up by Hill (1963) and Sato and Rourke (1964), the former being concerned with isolated enhancements in the north, which seemed to grow with a tongue-like character, and the latter with the more general average behaviour in the Antarctic. As well as providing a source of high-latitude ionisation, Sato and Rourke concluded that the universal time effects seen in various polar parameters were associated with the tongue structure. The drift theories were based on the $\underline{E} \times \underline{B}$ interaction between the near vertical magnetic field, and the electric fields in the ionosphere deduced from high latitude current systems. This interaction predicts speeds of about 100 m/s, though whether drifting ionisation could contribute a significant part to the total density has been questioned (Kamiyama, 1966b). Using laboratory values of the rate coefficients of the major loss-determining reactions, i.e.

$$O^+ + O_2 \longrightarrow O + O_2^+$$
$$O^+ + N_2 \longrightarrow NO^+ + N$$

and likely particle concentrations, the plasma should decay with a time constant of about three hours at 350 km. Drifting at 100 m/s during this time, the ionisation could travel only 1000 km, or 10° of latitude.

There does remain a discrepancy between laboratory and ionospheric measurements of loss rates (Yonezawa, 1966) which could mean that the time of three hours is short. Drifts certainly do occur, and their study will probably increase as a consequence of renewed interest in magnetospheric circulation, and its ionospheric implications (Axford, 1969).

The view has been put forward a number of times that many features of the ionosphere are a consequence, direct or otherwise, of particle precipitation. After reviewing f_oF_2 data from many stations and many years, Mariani (1963) concluded that an additional component of ionisation, probably due to precipitation, was necessary to explain the latitudinal variation of electron density. The second source, however, peaked at a latitude below the auroral zone; that is, in a region where one would not expect electron fluxes of energies suitable for producing F-region ionisation.

The existence of a corpuscular, or at least non-solar ionising source in the auroral region may be inferred indirectly from the average behaviour of the E-layer, for it is known that the variation of the critical frequency of a photo-induced layer should be expressible as

$$f_oE = A \cos^n\chi$$

where χ is the solar zenith angle and n an index equal to .25 for an α-type recombination law. The value of the exponent has been shown to drop in the auroral zone in both hemispheres (Penndorf, 1965; Maehlum, 1958); in the Antarctic, mean values of n above the auroral zone at Little America (L = 13.8) and Dumont d'Urville (L = 36.4) were 0.24 and 0.26 respectively, whilst in the zone at Byrd station, (L = 7.7), n had fallen to 0.18. This is ascribed to an additional component, such that the critical frequency is given by an expression of the type

$$f_oE = A_1 + A_2 \cos^n\chi$$

According to Patton et al., (1965) there is no corresponding corpuscular

term in the equivalent expression for the F_1 layer, though this is under the same solar control as the E-layer. One would not expect to find a similar variation at F_2 altitudes, as the ionosphere here is not exclusively under solar control. However, during an auroral display, irregularities superimposed on an enhanced background density have been observed at F_2 heights (Lund et al., 1967), indicating directly that auroral zone densities are enhanced by particle precipitation. Unexpectedly high densities at polar latitudes have been reported for many years (e.g. Meek, 1949), and the association of optical effects and density enhancements is not surprising. Obayashi (1958) ascribed the high densities during the storm of October 28, 1951 to the ionisation produced by bombarding particles associated with the excitation of aurora. A number of studies (i.e. Rees, 1963; Kamiyama, 1966b; Maeda, 1965) have been made, which give, for a particular primary energy, the ionisation produced by an incoming electron as a function of height. Measurements of the range of energetic electrons (Grün, 1959) indicate that particles with initial energies of 10 kev will produce a maximum of ionisation in the lower E-region. This ionisation will then be seen on ionograms as a thick E-layer (night E), or by some as yet unknown process, possibly similar to that proposed by Bennett and Noel (1965), it may be observed as a thin dense E-layer, or sporadic E. The energy spectrum of the injected particles is a major factor in determining the thickness of any resulting layer of ionisation, and this will increase as the precipitation becomes less mono-energetic. For overhead auroral displays, Bullen (1966) has found a quantitative relation between optical intensity and ionospheric density in the E-region. From Grün's range measurements, particles with initial energies of about 1 kev would be required to produce significant F-region ionisation, and it is only very recently that satellite instrumentation has been refined sufficiently to detect such energies by other than integral techniques. Thus while precipitating

particles, the ionisation and the auroral emissions they cause have been directly measured in the E and F_1 regions (McIlwain, 1960; Bullen, 1966), the existence of a large flux at low enough energies to influence the F-region remained speculation in the above studies.

A comprehensive review of all ionospheric phenomena thought to be related to particle precipitation has been published (Hartz and Brice, 1967), in an effort to determine the general pattern of particle precipitation. Two zones were found, one at higher latitudes, characterised by soft and variable fluxes, together with a region of more uniform hard "drizzle" throughout the day at a geomagnetic latitude of about 65°. One might therefore expect to find enhancements of density in the region of the softer precipitation.

Since the IGY period, a number of reports summarizing sometimes in great detail the behaviour at particular stations (e.g. Bellchambers et al., 1962) have been published. Reviews of the observations from a number of stations in the Antarctic have also been published for both normal conditions (Penndorf, 1965) and disturbed (Patton et al., 1965). One of the more intriguing features which arises from such studies is the universal time control of many ionospheric parameters, such as peak density and height, over large regions of the polar zone. A similar effect had been detected earlier in the Northern hemisphere by Dieminger (1959), who observed a longitude dependence in the time of a maximum value of critical frequency. He did not, however, point out that this peaking of the F-region density occurred everywhere at 2000 UT. Convincing evidence for an analogous effect in the south was provided by Knecht (1959) who performed a harmonic analysis of critical frequencies observed during the winter at the south geographic pole. Although variations in the solar zenith angle were negligible, the diurnal variation in the F_2 layer peak density showed a maximum at about 0700 UT. A general review of the universal time control of the Arctic and Antarctic regions has been given

by Duncan (1962). The equivalent, though much less pronounced UT enhancement in the Arctic occurs at about 1800 UT. The significance of these times in the North and South would seem to be that this is when the eccentric magnetic poles are towards the sun. If this fact is relevant, then one might anticipate greater effects in the south on account of the greater separation of geographic and geomagnetic poles there. Sato and Rourke (1964) consider the UT effect to be related to an enhancement of the tongue structure mentioned earlier.

An alternative explanation was proposed by King et al. (1968). This involves the interaction of neutral winds on a global scale with F-region ionisation. Basically, such winds blow across the pole from a local time of about 1400 hrs, and effectively drag the ionisation up or down magnetic field lines, depending on the dip angle, so modulating both the height of the layer and its peak density. The theory has been developed assuming a uniform electron density over the earth, and therefore applies more to summer conditions. Good simulation of the f_oF_2 and h_mF_2 curves for individual stations has been achieved. It may be said that this is not a true universal time effect. In the south, the density at all stations is enhanced around 0700 UT simply because all except Macquarie Island lie on the same side of the dip pole. Excepting this latter station, the relationship between the wind and the field at all stations is such that ionisation is being raised (and therefore N_mF_2 increased) at this time. On this theory, however, Macquarie Island, being on the opposite side of the dip pole, should have its density depressed at 0700 UT. According to Duncan (1962), this was probably not the case, though experimental difficulties involved precluded a positive answer.

A further suggestion for the cause of the UT variation has been advanced most recently by Maelhum. This is based on the observed changes in position of very low energy precipitating electrons, which now seem likely to be responsible for the formation of the polar F-region in

winter. The role of this flux is discussed further in a later chapter.

The polar ionosphere often appears from ionograms to be very disturbed, but the sharpness of the transition from a smooth region to one populated with irregularities of ionisation becomes apparent when sequences of topside ionograms are considered. The regions of disturbance also show up clearly as scintillation patches in the records of Faraday fading of a radio signal which has traversed the ionosphere. Titheridge and Stuart (1968) have examined such records from the Ionospheric Beacon S-66, which is in a polar orbit at 1000 km altitude. They found completely scintillation-free passes were possible, though infrequent, but then extremely large horizontal density gradients were seen. More generally, irregularities were present which persisted in the same position for a number of passes, while there were some locations, notably between the geographic and geomagnetic poles, which showed continuous disturbance. This observation of the repeatability of effects over several passes has been a feature of the present work, and it is suggested it is very significant.

The spatial and temporal resolutions (normally not better than 15 mins) provided by ground ionosondes are severe limitations at polar latitudes, where much fine structure is evidently present. Satellite-borne instruments now enable a more detailed study to be made of the polar plasma by providing a virtually continuous record of the electron density along the track of the vehicle. In the case of Alouette I, data from which is now considered, the spatial resolution corresponds to about 100 km, or a degree of latitude.

3: The Plasmasphere Termination

3.1 Introduction

A consistent feature seen on satellite records at high latitudes is an abrupt decrease in the electron concentration as measured at a particular altitude, by up to an order of magnitude in north-south distances of sometimes less than 100 km. This is followed by a recovery (sometimes very rapid) to larger values at higher latitudes. This effect has been noted independently in a number of experiments, and the feature has been termed the main trough (Muldrew, 1965).

Thomas and Dufour (1965) suggested that the trough was a demarcation between the solar and aurorally produced ionization and commented upon the possible association between the trough and the plasmapause, or knee in the equatorial electron concentration profile at a geocentric distance of about 4 earth radii (Re). In view of the success of theories predicting protonospheric electron concentrations from the assumption that diffusive equilibrium prevails along geomagnetic tubes of force (e.g., Angerami and Thomas, 1964), and the observation of field aligned density structures (Sayers, 1964) it appears reasonable that any association would be via field lines. Rycroft and Thomas (1967) have used whistler and topside measurements to investigate such a link on the night side of the earth, and found that for quiet magnetic conditions, the centre of the trough appeared to lie on the same L shell as the midpoint of the plasmapause. This work is now extended, and it is suggested that it might be more meaningful in any attempt to correlate the plasmapause and trough positions to associate the midpoint of the lowlatitude 'wall' of the trough with the centre of the plasmapause as observed in whistler data.

3.2 Data Analysis and Observation Programme

The basic data used in this survey were electron densities both at the F-layer peak, and the vehicle height, derived usually from the extraordinary ray trace on successive topside ionograms.

The electron concentration N at the altitude at which the frequency f_x is reflected in the extraordinary mode is given by

$$N = 1.24 \times 10^4 (f_x^2 - f_x f_H) \qquad (3.1)$$

where f_H is the electron gyrofrequency at that altitude. In this formula, N is given in electrons/cc, and f_x and f_H are measured in Mc/s. Thus the electron concentration, N_s, at the satellite (1000 km above the earth) is derived by putting $f_x = f_{xs}$ and $f_H = f_{Hs}$ in (3.1), where f_{xs} is the frequency at which the extraordinary ray has zero range (i.e., is reflected back from the immediate vicinity of the vehicle), and f_{Hs} is the electron gyrofrequency at the altitude of the satellite. The latter can be derived either from the known magnetic field at the orbital location of the satellite, or directly, from the observed gyroresonance signals that occur at integral multiples of the electron gyrofrequency at the satellite. Similarly, $N_m F_2$, the maximum electron concentration in the F region, occurring at an altitude $h_m F_2$, is obtained by putting $f_x = f_x F_2$ (the extraordinary ray critical frequency measured on the ionogram) and $f_H = f_H(h_m F_2)$ in (3.1).

To derive the electron gyrofrequency $f_H(h_m F_2)$ at the height of the F peak, it is strictly necessary to carry out a full real height analysis, i.e. to derive the electron concentration distribution with height from the observed virtual height-frequency traces recorded on the topside ionograms. However, the altitude of the layer peak is known to occur at about 300 km and f_H is not strongly altitude dependent, so that if f_x does not approach f_H too closely (Thomas and Sader, 1964), values of N derived from (3.1) are likely to be accurate to within ~5%. The

quantities f_xF_2 and f_{xs} are included in tabulated numerical data published by the Canadian Defence Research Establishment (Alosyn) and have been used to derive N_s and N_mF_2, the electron concentration parameters used here.

Fig. 3.1 shows the distribution of telemetry receiving stations affording cover of the northern polar cap and also the approximate range of each station (after Thomas et al., 1966). Something like one-half of the western hemisphere, which includes the magnetic poles, has continuous coverage. On a projection such as this, the tracks of successive transits appear very nearly as straight lines, each rotated some 25° further westward as shown, due mainly to the eastward rotation of the earth. All tracks are tangential to a latitude of 80.5°, equal to the vehicle's orbit plane inclination. Because of the high vehicle speed, the time occupied by a transit is small, and any changes in the ionosphere found along a path are reasonably assumed to be spatial rather than temporal variations.

While this method of displaying successive passes is useful, a better physical picture is that of the orbit plane fixed in space with respect to the earth-sun line, or actually precessing slowly westward, while the earth, with its eccentric magnetic poles, rotates inside the orbit. This shows clearly that over a period of time during which precession is small, the satellite will reach a given latitude at two fixed local times, one on the prime and one on the return sweep. Such a picture serves to illustrate a major difficulty in satellite studies. The slow precession of the orbit, in this case one hour of local time per week at a given latitude, means that a period of three months is required to obtain a 24-hour local-time coverage. During this interval, it is possible that seasonal effects will obscure diurnal variations.

The survey was started with data for the northern winter of 1962 since, in this season, nonsolar effects will be relatively more pronounced

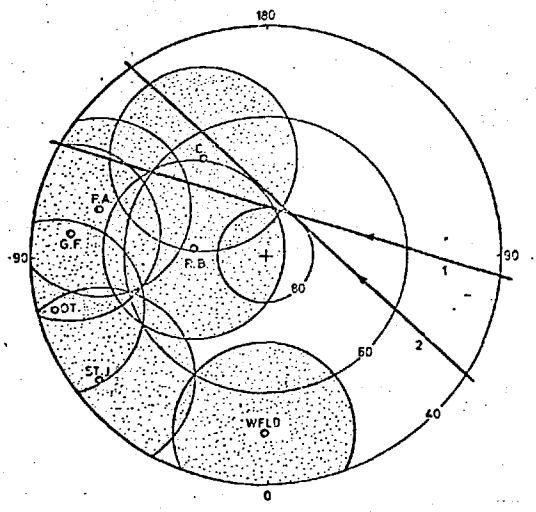


Fig 3.1 Location of the Alouette receiving sites and their approximate coverage over the polar regions in the northern hemisphere. The tracks of successive passes appear as straight lines, marked one and two, and are rotated progressively westward with respect to a fixed point on the earth.

PA	Prince Albert	OT	Ottawa
RB	Resolute Bay	C	College
WFLD	Winkfield	GF	Grand Forks
ST J	St Johns		

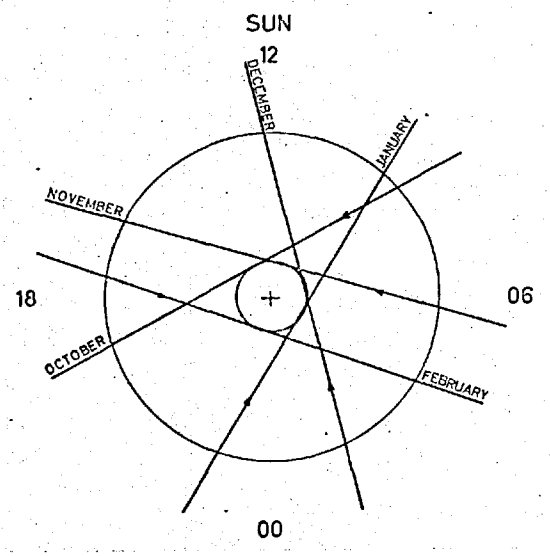


Fig. 3.2 Approximate positions with respect to the sun of the transpolar satellite tracks considered in this survey. All tracks are tangential to a geographic latitude of 80.5°, shown as the inner circle in the diagram.

because of the absence of ultraviolet radiation. It was also a time of low solar activity, so that any results should represent the typical, quiet-time ionosphere. The results have come from a detailed survey of all passes recorded in the first two weeks of each month from October 1962 to February 1963, by which time the diurnal coverage was complete and included an overlap as a check on seasonal variations.

Utilizing the concept of the orbit plane precessing about the earth-sun line, Fig. 3.2 shows the average position in space and local time of the various groups of passes. During each of the two-week intervals, in which the orbit plane rotates through 2 hours of local time, the polar behaviour was taken as applying to the mean position of the tracks, which is drawn in the figure.

3.3 The Plasmasphere Termination

In this section, the electron concentration troughs and, in particular, the changing position of the trough boundaries are considered in some detail. Electron concentration troughs in the topside ionosphere were evident in the Alouette I nighttime observations of Thomas and Sader (1963, 1964), which were further processed to reveal the trough in contours of density at 1000 km by Dayharsh and Farley (1965). Muldrew (1965) observed the same effect in the northern hemisphere from a sudden drop in the F-peak critical frequency at a latitude of about 60°N, indicating a rapid fall in the electron concentration at an altitude of about 300 km. From a real height-density analysis of a sequence of topside ionograms, Thomas et al. (1966) were able to show the presence of the trough simultaneously at all altitudes from the F-layer peak up to the vehicle. By use of ion traps, Sharp (1966) detected the presence of the trough at various heights in the F region from variations in the positive ion concentration. More recently, using differential Faraday rotation measurements from the Beacon satellite S-66, Liszka (1967) has shown that the trough is present in

total electron content measurements, confirming that the phenomenon is not simply a redistribution of ionization.

It has been pointed out (Thomas et al., 1966; Calvert, 1966) that the spread nature of echoes on topside ionograms poleward of the midlatitude trough indicates that the ionosphere here is more disturbed than at low latitudes. Recently, results from the Alouette II topside sounder (Nelms and Lockwood, 1967; Hagg, 1967) have shown that at altitudes of 2000 - 3000 km there is a fall in electron concentration at a latitude approximately equalling that of the F-region main trough, but that polewards of this there is usually no recovery to higher concentration; the ionosphere above 60° magnetic latitude is rather depleted in electron concentration.

These two observations suggest that the ionosphere should be considered in two parts; the low-latitude, predominantly solar-controlled region, which terminates fairly abruptly at an L value of 4 - 5, and the polar ionosphere at higher latitudes, containing enhancements of ionization as a result of some process as suggested by Thomas and Dufour (1965). If the enhancement is in the form of a broad peak, commencing slightly above the midlatitude termination of the solar-controlled ionosphere, the resulting curve of electron concentration versus latitude may well show a trough around L = 4. On this interpretation, perhaps the most physically meaningful parameters of the trough would be the positions of its boundaries rather than its centre.

Data obtained from a November pass and converted to electron concentration through equation (3.1) are plotted in Fig. 3.3 and serve to illustrate the division of the ionosphere into two parts, an abruptly terminating midlatitude region together with additional ionization at higher latitudes. It is also apparent that during the afternoon hours, the equatorial boundary of the trough is very steep, while the high-latitude side is less steep, that is, the concentration gradients are

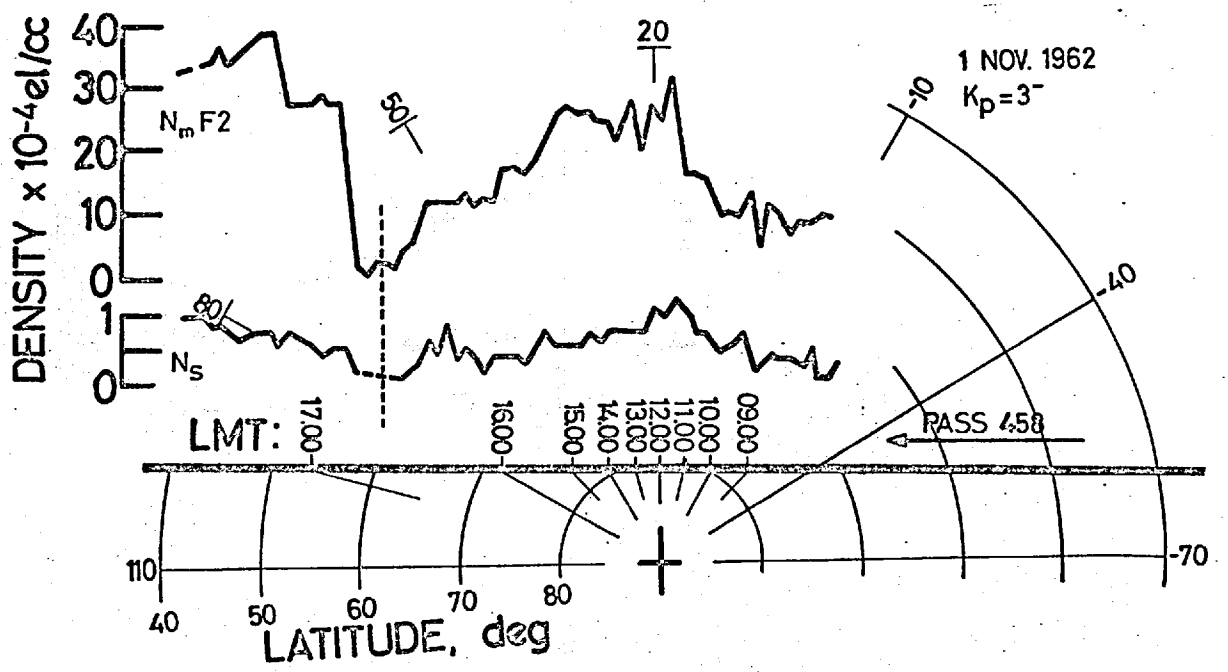


Fig. 3.3 The electron density at the F2 peak ($N_m F2$), and at the satellite (N_s), calculated from the extraordinary ray for one pass. The local times along the track and circles of geographic latitude are shown. Densities at all heights from the layer peak to the vehicle show the same trends.

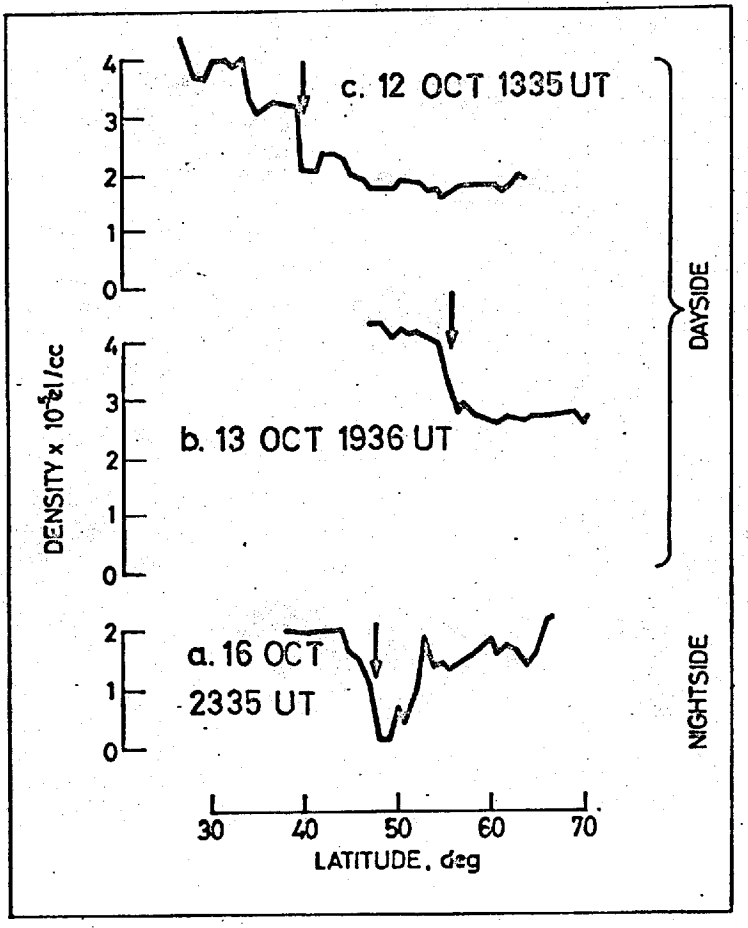


Fig. 3.4 The electron density $N_m F2$ plotted against geographic latitude on three occasions in October 1962. Curve a. shows the narrow 'cleft' which forms the trough (the low-latitude boundary of which is arrowed) in the evening sector, while b. and c. indicate the feature associated with the trough boundary during the morning hours.

greatest on the low-latitude side. This is the reverse situation to that described by Rycroft and Thomas (1967) for the night hours, where the polar side of the trough was steep enough to be described as the auroral cliff. It is significant that in the transit of Fig. 3.3, the solar zenith angle varies only between 93° and 98° over the whole pass. The sudden changes in electron concentration are thus very unlikely to be related to photoionization effects.

From October passes, it is clear that, as noted by Muldrew (1965), the trough is absent during midmorning. The distinctive feature on successive passes seems to be a consistent falloff in F-peak concentration from midlatitude values over a period at least as long as such passes are available, that is, 9 - 10 hours. However, this uniform falloff frequently terminates in a 'corner', which leads into a flatter region identified here as the polar zone. The corner, or step, was taken to be the feature corresponding to the cliff-like concentration gradient of the low latitude boundary of the midafternoon trough. The view that there is a feature at this local time which can be associated with the trough is supported by the continuing presence at this latitude of an anomaly in the Faraday rotation of moon echoes, which has been linked with the trough (G. N. Taylor, private communication, 1969). The evening trough at about 1900 LT is quite marked and similar in shape to, but wider than, that found in midafternoon. Examples of the regions identified with the trough for morning and evening are shown in Fig. 3.4. The high-latitude troughs of Muldrew (1965), which are to be seen most frequently during the evening hours, appear superimposed on the main features (see, for example, Figure 6 in the above reference) and have not been considered in this survey.

The dayside passes recorded in December covering local times near noon show the same rise in density toward midlatitudes as was evident in the October records, except that the rise was greater and usually steeper

than in midmorning. This probably reflects a transition to the cliff-like trough walls characteristic of midafternoon.

3.4 Movements of the Trough Boundaries

It has been noted elsewhere (Thomas et al., 1966) that the positions of the troughs of ionization on successive transits appear to follow L shells rather than geographic latitude. This does not imply that the position of the trough in local time is similarly aligned; the day-side phenomena occur at obviously higher L values than the night-side phenomena; rather it implies that at a given local time the trough moves about in conjunction with the eccentric magnetic poles. Thus in Fig. 3.5, which shows computed L curves superimposed on a north polar geographic grid, a trough at a fixed local time, i.e. position with respect to the sun, would appear constrained to move along an L contour as the earth rotated beneath it. Such movements have been examined both as a function of universal time and Kp for all, rather than individual days.

The object of this was to look statistically for a link between the plasmapause in the equatorial plane and the trough at high latitudes. Since it is the midpoint of the knee that is located by whistler techniques, ideally the corresponding point measured in the ionosphere should be the midpoint of the low-latitude wall of the trough. In practice this point is frequently ill-defined, particularly during the night hours. The procedure adopted was to measure the position of the base of the equatorial wall of the trough, as this is generally the point most clearly defined. It was identified and measured on a number of transits during each monthly interval, giving two sets of trough data per month, each set spanning a local-time sector of two hours as a result of orbital precession.

For each time sector, a polynomial was fitted to the trough base position, measured in both geographic and invariant latitudes, as a

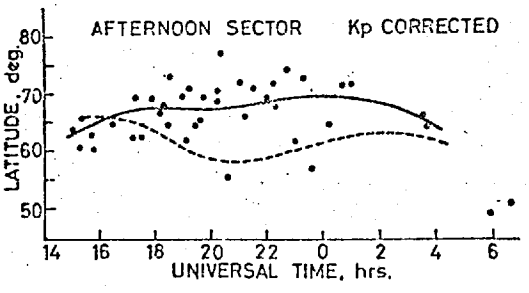


Fig. 3.6 UT variations of the low-latitude boundary of the troughs recorded during November 1-15, 1962. The points are the positions in invariant latitude, for Kp=2, and the solid line a fifth degree curve fitting them. The broken line is the equivalent curve through the same data plotted in terms of geographic latitude.

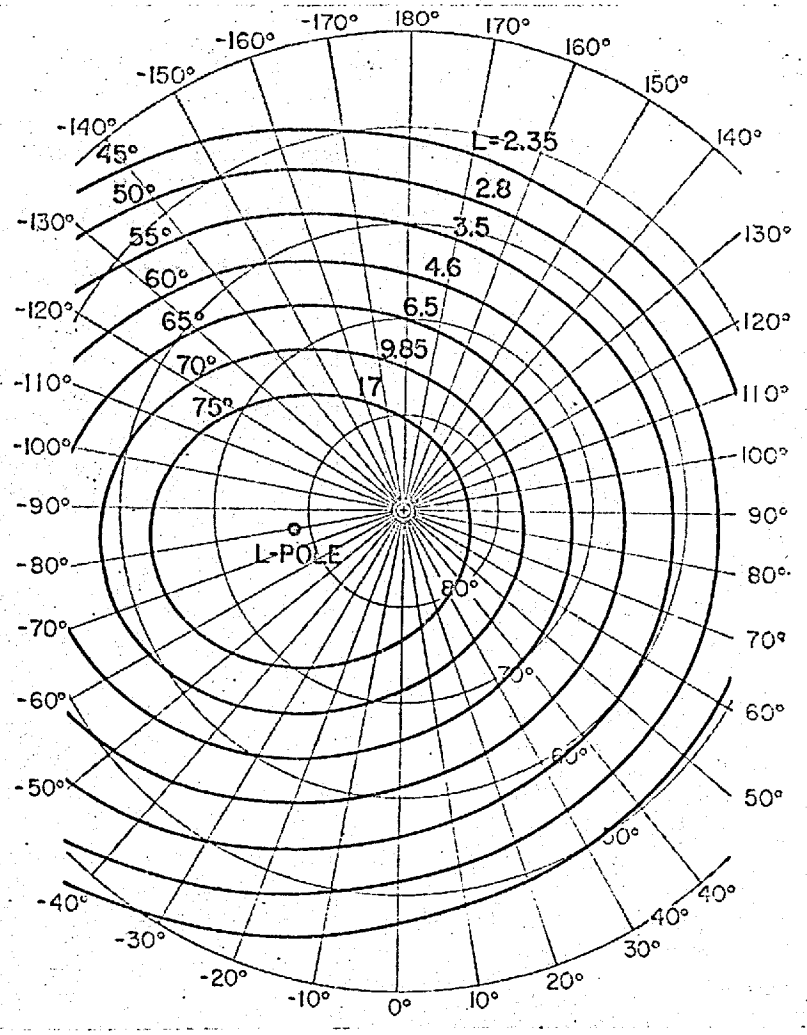


Fig. 3.5 Computed contours of constant L value and the corresponding generalised invariant latitude Λ' (defined by $\Lambda' = \cos^{-1}\sqrt{(1+h/Re)/L}$ at a height h) for an altitude of 1000km, superimposed on a north polar geographic grid. (From Thomas et al., 1966)

function of universal time. In every case, the geographic latitudes of troughs observed at a given local time, showed a movement to or from the equator. The trough is closest to the equator at the universal time when the eccentrically rotating L pole enters the local-time sector concerned. The troughs are thus moved toward and away from the equator in synchronization with the rotating L pole. The use of invariant latitude Λ' removed this effect, and also reduced slightly the standard deviation of the fitted curve, indicating magnetic control. An example is shown in Fig. 3.6 in which the trough positions have been normalized to a Kp value of 2 using regression lines similar to that shown in Fig. 3.7. A slight curvature remaining in the invariant latitude locus indicates that the troughs do not follow exactly the computed L contours, which are calculated from a diurnally averaged model of the magnetic field. The true locus, then, lies somewhere between a contour of geographic and invariant latitude, but closer to the latter. Had dip, rather than invariant, latitude been used in this analysis, the peaking of the invariant latitudes in Fig. 3.6 near 2100 LT (when the magnetic pole is in the local time sector of the observations) would have been greater, as the contours equivalent to those of Fig. 3.5 in terms of dip latitude are rather more eccentric (Thomas et al., 1966). Thus invariant latitude (suggesting distant magnetic influences) results in a better organisation of the data than dip latitude (suggesting local ionospheric control). The trough is at its highest latitude near the local times of Fig. 3.6, i.e. midafternoon. An invariant latitude of 70° at 300-km altitude is equivalent to an L of 9.

To examine movements with magnetic activity, first linear and then parabolic regression lines were calculated for the position of the trough edge as a function of Kp in each local time position. The scatter in the plots is quite large, and the improvement in fit gained by the use of the second-order curve was negligible. An example, the regression of the

troughs in the evening (~1800 LT) sector, is shown in Fig. 3.7. For the evening troughs, the positions were correlated with the Kp index up to 30 hours before and 24 hours after the event in question. The correlation coefficients obtained are presented in Fig. 3.8. The correlation between trough wall position and Kp index is here highly significant. A similar correlation analysis carried out for the other local-time sectors showed that while the highest correlation was obtained using the Kp value within six hours of the time of the trough observation, the curves corresponding to Fig. 3.8 were less sharply peaked. In addition, the maximum correlation observed fell progressively from the high values illustrated on the dusk side to rather lower and less significant values toward the dawn side of the earth. The linear regression equations found at various local times are listed in Table 3.1. Thus, while the trough at all positions moves equatorward with increasing magnetic agitation, the rate at which it does so and the degree to which it is correlated with Kp vary, both being greatest in the evening sector.

TABLE 3.1

Local-Time Sector	Regression Equation	No. of Points
0600	$\Lambda' = 57.28 - 1.07$ Kp	22
1000	$62.09 - 1.01$ Kp	49
1200	$70.67 - 1.85$ Kp	22
1500	$69.34 - 1.86$ Kp	40
1800	$69.59 - 2.44$ Kp	42
0100	$55.32 - 0.03$ Kp	20

3.5 Link between Plasmapause, Trough, and Auroral Oval

Plasmapause measurements by whistler techniques have all been made in the equatorial plane. Since some features of the polar ionosphere are best organized by the use of the magnetic shell parameter L, it is

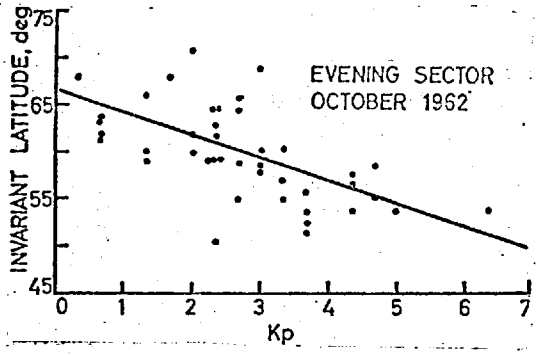


Fig. 3.7 The invariant latitude of the low-latitude boundary of the trough for different values of the magnetic disturbance index Kp. The boundary moves towards the equator as Kp increases.

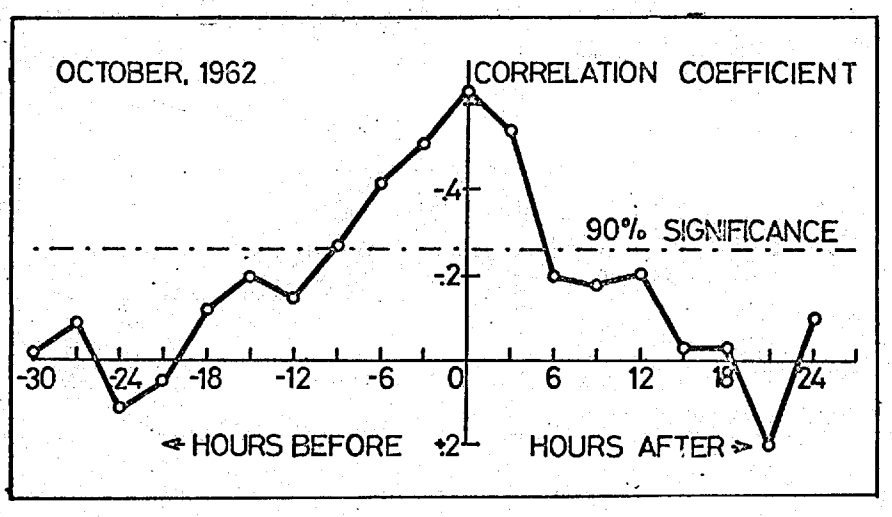


Fig. 3.8 The correlation of the position of the low-latitude trough boundaries in the evening sector with Kp up to 30 hours before and 24 hours after the time of the trough measurement. The peak correlation is statistically highly significant for the 42 troughs considered.

of interest to determine the L shells linking the position of the plasmapause and the high-latitude ionosphere. The position in earth radii of a point in the equatorial plane and the location, in geographic latitude, of the point at 300-km altitude to which it is connected via a field line was computed at different longitudes. Assuming that the ionosphere is in equilibrium along a tube of force, the width of a trough boundary at 300 km in the ionosphere that results in a knee width of 0.5 Re, or vice versa, is estimated to be 2°, or twice the resolution of the Alouette sounder. As some trough sides are steeper than this, the figures linking the widths of the plasmapause and trough sides are of the correct magnitude in the equatorial plane and at the F region. Against this must be set the fact that the electron concentrations at 1000 km (e.g., Fig. 3.3) plus a few results from passes by Alouette II (Nelms and Lockwood, 1967) and Explorer 31 (Donley, 1967) do not show the steep concentration gradients required at intermediate heights. There remain, however, gross similarities in the two phenomena, such as the equatorward motion accompanying magnetic activity. Rycroft and Thomas (1967) have observed similar motions of the knee and trough throughout the local night. In addition, theories of plasma convection within the magnetosphere predict the strongest interaction between the corotating plasmasphere and the convecting magnetospheric plasma in the evening hours (e.g., Dungey, 1967), and it is at this time that the knee is observed to be most unstable. Thus the present conclusions that this is also the time at which the trough is most clearly defined, correlated with and sensitive to Kp changes is evidence that the trough has a magnetospheric link.

The relative positions of the knee, the equatorial side of the trough, and the auroral oval are shown in Fig. 3.9. The auroral oval is that given by Feldstein (1963) for fairly quiet conditions, and the plasmapause position is that given by Carpenter (1966) as the average

position for days with Kp indices between 2 and 4. These data have been converted from an equatorial radius to an invariant latitude at an altitude of 300 km. On such a projection, the evening bulge in the equatorial plane is seen as a small flattening poleward. The trough position is for a Kp value of 3 and, on the nightside, is approximate, as data are available only for the 0100 hr local-time sector. Several features are apparent:

1. Both the trough edge and the plasmapause occur below the auroral oval.

2. While the auroral oval and the trough are eccentrically placed about the magnetic pole, the knee is approximately symmetric. The position of the trough edge is in good agreement with the zone of polar low concentrations found at all local times at an altitude between 1500 and 3000 km (Hagg, 1967).

3. Considering only the trough and the knee, although they are displaced and there is no trough evening bulge to match that of the knee, the two loci are approximately the same size. The results of Rycroft and Thomas (1967) for troughs found in the summer night were substantially in agreement with the present conclusions; namely that the equatorial trough edge at night occurs at a significantly lower latitude than the equivalent latitude of the knee.

The reverse is true on the dayside. If a correction is made for the fact that we have measured the base of the trough edge, rather than the midpoint of its low-latitude wall these conclusions are unaffected. The effect of a correction would be to expand the trough locus slightly equatorward, preferentially on the night side.

The displacement of the two loci suggests that the effect might, in part, be due to field line compressions on the day side and expansion on the night side. This gives rise to two discrepancies which are cumulative. In the first, the effect of a day side compression is to

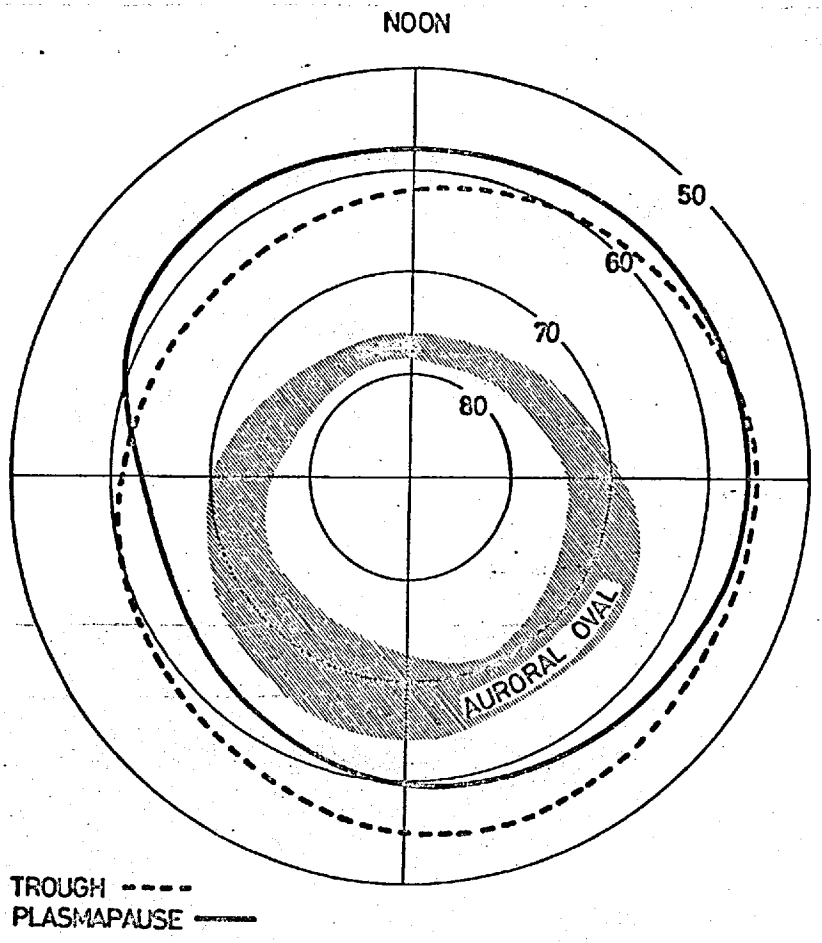


Fig. 3.9 The relative positions, in invariant latitude, of the trough boundary (or plasmasphere termination), the auroral oval, and the plasmapause projected back along a field line to the ionosphere. The positions given are those expected for moderate magnetic activity (Kp = 3). There is a significant displacement between the plasmapause and trough positions.

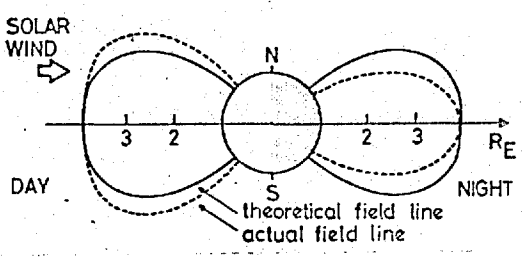


Fig. 3.10 Field line distortions which would give rise to the discrepancy between the plasmapause and trough positions illustrated in the previous figure.

bring the knee to a lower Re, while the compressed field line reaches the earth at a higher latitude than the diurnally averaged field maps indicate. The day-side troughs, if linked via the distorted field line to the plasmapause, then appear at apparently high L values. The reverse would occur on the night side. This is illustrated in Fig. 3.10. The second point arises in the whistler determination of the knee position. Whistler ducts are located basically by identifying the magnetic field strength at their equator crossing point. The assumption of a particular field model then enables the geocentric radius to be determined. In deriving the plasmapause data from which Fig. 3.9 is constructed, Carpenter (1966) used a centred dipole model geomagnetic field. If in fact the true field was compressed, a particular field strength would be obtained at a greater radial distance than is indicated by a simple dipole field; i.e. the knee would be placed at too small an L value, or on a field line intersecting the earth at too small a latitude. Once more, the reverse is the case in the extended geometry of the night field, and the errors might again contribute to the discrepancy between trough and plasmapause positions if they are directly linked via field lines.

Though there is other experimental evidence of large field distortion at low altitudes, particularly with varying solar wind attack angles (Maelhum, 1968), theoretical calculations of the effect of solar wind pressure suggest that compressions on the dayside amount to only about .1 Re at 5 Re (Mead, 1964), too small to explain the present discrepancy. These computations were for a dipole perpendicular to the solar wind and as yet only preliminary reports have been made of the effect of tilting the dipole (Olson, 1969). Experimentally, Mead and Cahill (1967) have reported that at above several Re, the dayside magnetic field can be severely distorted from the direction implied by the field models commonly employed and that, under disturbed conditions, the

field magnitude near 3 Re can be altered by inflation, due to the existence of ring currents.

The plasmapause locus has been found from whistler data from one longitude (Carpenter, 1966). This means that the position found at a particular local time is also at a defined universal time, so that it is not possible to investigate whether or not the radial distance is a function of UT as is suggested by the trough measurements of Fig. 3.6. An experiment designed to do this would be very desirable. A positive result would imply that field line distortions at geocentric distances of 5 Re are possible, while no movement of the knee with UT would indicate that the failure of the trough to follow completely a contour of fixed invariant latitude is a feature local to the ionosphere.

On the evidence to date it seems that the latter is probably the major contributor to the UT motion of the trough. From Fig. 3.6, in order to follow a constant L contour as the earth rotates, the trough would have to migrate several degrees nearer to the equator than it does. In the absence of any apparent reason why the ionisation should recombine at lower latitudes to form the trough there, it must form either by ionisation flowing upwards from the ionosphere, or by moving the trough bodily equatorwards, which would compress the ionisation at latitudes below the trough. This is the mechanism which might be expected from magnetospheric circulation theories of the trough origin (Nishida, 1966), and some support for this is seen in that the mid-latitude electron density often appears higher when the trough is closest to the equator. This effect would be greatest on the dayside near noon, since here solar ultraviolet production reaches its highest latitudes. The greatest equatorwards motion and compression would then occur near 1800 UT in the north, and might be the cause of the universal time control of the topside density seen at mid-latitudes (Rothwell, 1965). If the ionosphere were a perfect collisionless plasma and no electric fields acted, the

trough would remain "tied" to a particular field line. In the absence of field line distortion, it is suggested that the small but finite electron-neutral collision frequencies near the F-layer peak (which from N(h) analysis was very low during this period) may have been sufficient to allow significant cross-field diffusion, producing the quasi-magnetic control of the trough boundary in Fig. 3.6.

4: Electron Density Distribution above the Winter Pole

4.1 Transpolar Passes

In the previous chapter, reasons were discussed for considering the ionosphere to be made up of two parts, the part at low latitudes predominantly solar controlled, and the region at high latitudes aurorally associated. Transpolar satellite passes which regularly sample the second medium are now considered. These passes show that the high latitude electron densities tend to be rather variable but to a first order, a pattern may be extracted. The results of the study will be discussed primarily with reference to the series of about 100 passes obtained in November 1962. As illustrated in Fig. 3.2, the satellite entered the polar zone around 0600 LT and left in midafternoon during this month.

The effects occurring across the polar cap during the November local-time section were quite regular and, for a particular transit, the latitudinal distribution of ionization was observed to follow the same pattern both at the F-region peak and at the satellite. At a given altitude within this range (~300 - ~1000 km), the results fall into two groups, corresponding to two basic patterns along a track. The first group exhibited two broad peaks of ionization at high latitudes, separated by a region of depletion over the polar cap itself, the second only a single broad peak. A good example of the first group is shown in Fig. 4.1 in which the electron concentration at 1000 km on a sequence of consecutive passes on one day is shown. This method of display is in a geographical reference frame (Fig. 3.1), causing the passes to appear displaced relative to each other, but this is only due to the earth's rotation. Each track lies at nearly the same angle to the earth-sun line (Fig. 3.2), so that the same range of local times is being sampled by each pass. The pairs of enhancements observed along each track were

equally noticeable at the F-region peak at these times. The local time at the two enhancements along the track differs by about 10 hours. An example of the second group, showing only a single broad peak over the polar regions, is shown in Fig. 4.2. The vertical cutouts in this figure show the general form of the transpolar variation of electron concentration at the F-region peak, though the actual quantity plotted is the extraordinary ray critical frequency f_xF_2, which is related to N_mF_2 through equation (3.1). Again for these particular consecutive transits the variation of N_s was similar. Fig. 4.2 illustrates particularly well the midlatitude ionosphere termination discussed earlier for several passes.

It is emphasized that the transits of Figs. 4.1 and 4.2 do not constitute instantaneous models of electron concentration over the polar cap but represent a sampling of the ionosphere along a fixed direction to the earth-sun line at different universal times. It seems highly significant that the ionosphere can be represented in this manner, for it suggests that longitudinal variations in the ionosphere are less important than local-time effects, that is, the position with respect to the earth-sun line. This representation shows also that the electron concentration along a particular track can be highly repeatable over a period of at least 10 hours, which in turn suggests there may be an approximate but characteristic distribution of polar ionization under which the earth rotates.

It was possible to classify almost all of the November passes into the two patterns described (Figs. 4.1 and 4.2), with the twin-peaked group predominating by a factor of 2 over those exhibiting a single peak. The single peaked distribution was more characteristic of the first week of the sample (November, 1 - 7), whilst the twin-peaked variety became predominant in the second week. The significant feature here is probably the steadily changing angle (by 30° over the whole two week sample) the

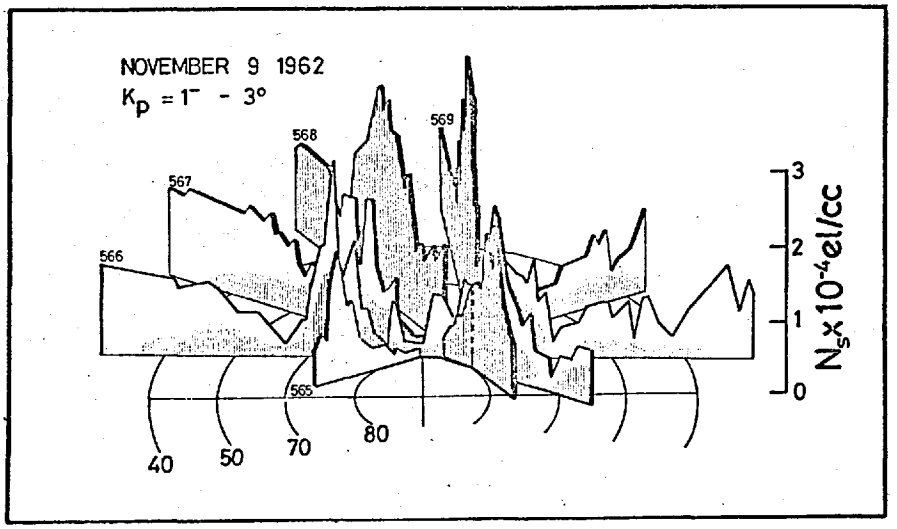


Fig. 4.1 Three-dimensional scale model of the electron density N_s at the Alouette I orbit (1000km altitude) for a series of consecutive passes (565-569) above the north pole on November 9, 1962. Each pass shows the same twin peaks of density at high latitudes. Circles of geographic latitude are indicated.

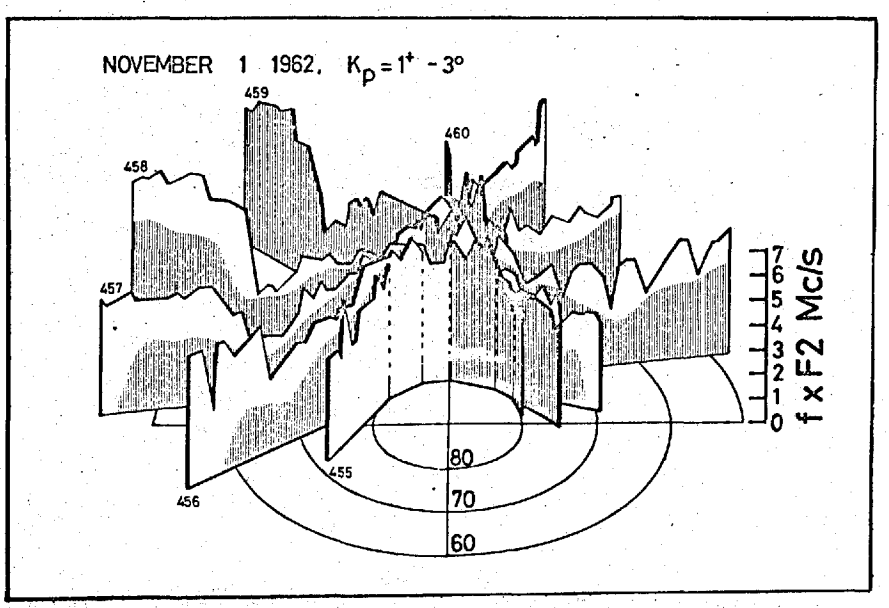


Fig. 4.2 Three-dimensional scale model of the extraordinary ray critical frequency of the F_2 layer for a series of consecutive passes (455-460) in November, 1962. The quantity f_xF_2 indicates the actual variation of electron density at the peak of the F layer (300km altitude). Circles of geographic latitude are also shown.

orbit plane made with the earth-sun line.

The ability to so classify the pass types indicates again that both density distributions are stable, and to a first order are independent of longitude. Any model of concentration must be able to explain these two entirely different, yet both stable and repeatable profiles obtained along approximately the same satellite track.

Passes occurring during February crossed on the night side of the pole on a track approximately parallel to those of the November group and generally also showed two high-latitude peaks, rather less dense than those of November, separated consistently by a region of very low concentration over the polar cap. In addition, the starts of these passes on entering the auroral zone at about 1800 LT overlap the region investigated in October, four months earlier. Despite the large time difference of four months between the October and February observations, the passes showed close similarity at corresponding local times. An example of the very low values of N_mF_2 at highest latitudes is given in Fig. 4.3. Unfortunately, accurate densities at the vehicle are not usually available from ionograms taken in such low density regions.

4.2 A Model of the Polar Ionosphere

On the basis of these measurements, it is possible to formulate a tentative model of the instantaneous electron density distribution over the polar region. Although features may become indistinct or absent on particular passes, the fact that it is possible to detect an average shape along a particular line indicates that a characteristic distribution of density exists, however perturbed it may become at times.

The features of a stationary density distribution in the upper F-region consistent with those found on intercepts in different directions are shown diagrammatically in Fig. 4.4 where darker shading represents a greater electron density. The picture suggested is a crescent-shaped

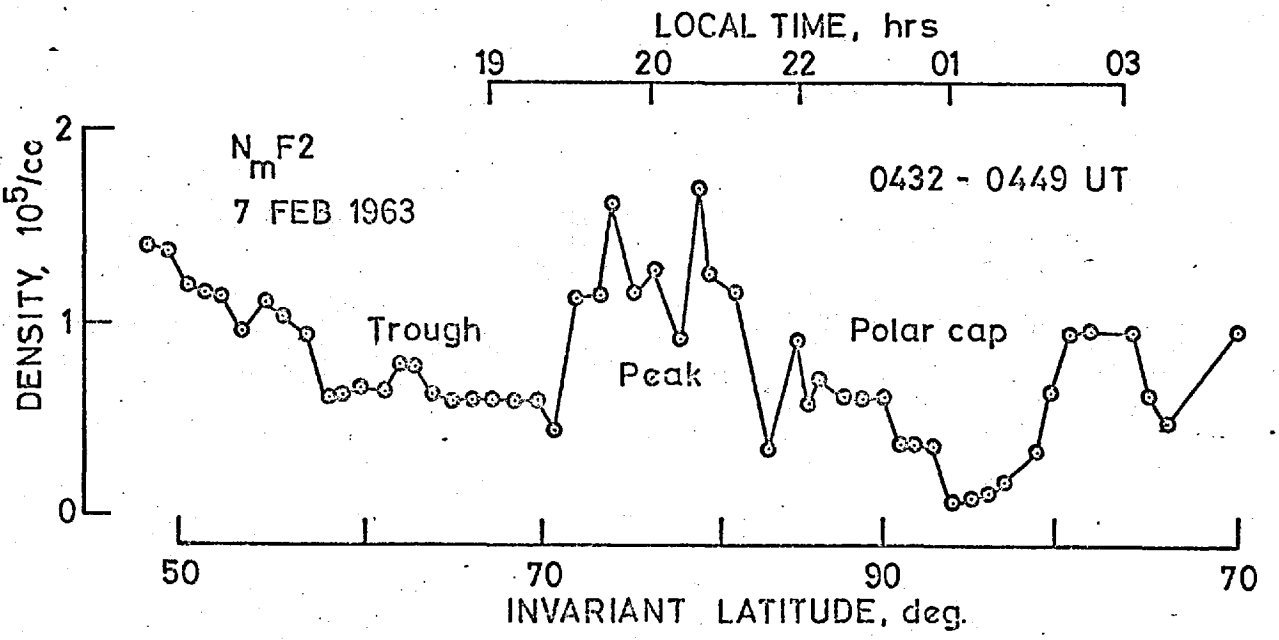


Fig. 4.3 The electron density at the peak of the F_2 layer along a track which passed behind the geographic, and over the L pole. In addition to the trough between invariant latitudes of 60 and 70 degrees, extremely low densities are visible above 80°, in the polar cap region.

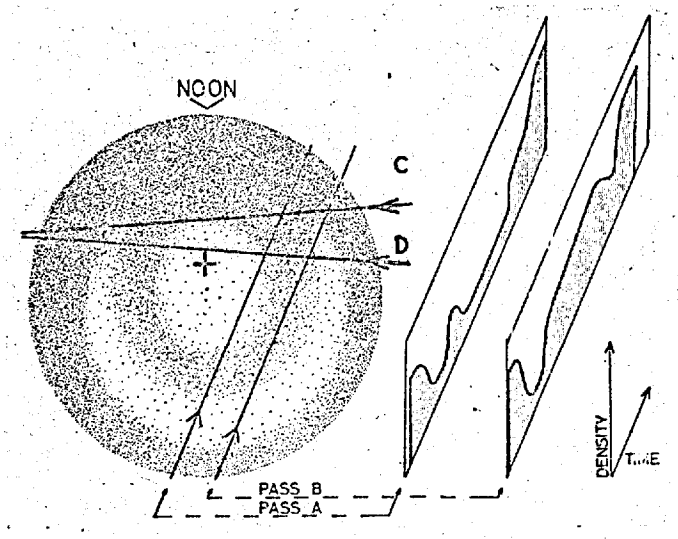


Fig. 4.4 Idealised distribution of electron density in the altitude range 300-1000km above the winter pole, in which darker shading represents a greater particle density, showing the polar cap depletion and the trough. The sketch (right) shows two possible density records which may be obtained from the same pattern if the whole distribution moves with respect to geographic co-ordinates, as it might, if for example, it followed magnetic control as the earth rotates. Compared with the density pattern, i.e. magnetic co-ordinates, the tracks A and B appear displaced. Passes C and D relate to the two types of pass seen in November, as explained in the text. The cross indicates approximately the magnetic pole.

trough of low density plasma surrounding the pole, narrow on the evening side, wide during the morning hours, together with a large depression of density over the polar cap itself, elongated and displaced in the midnight direction. Alternatively, if the ionosphere is considered in two regions, this pattern could be described as a relatively steep-sided ring of ionization about the pole, surrounded eccentrically by the low latitude ionosphere which terminates rather abruptly, particularly during the afternoon hours. The noon portion of the mid-latitude ionosphere is here assumed to overlap the central core of ionization so that the trough disappears.

The range of density, N_mF_2, within the polar cap is rather large. The average density seen towards the nightside of the polar cap depletion and in the trough was $0.5 \times 10^5 cm^{-3}$. Densities within the high-latitude peaks were rather variable and did not always correlate with magnetic activity, as indicated by Kp. On the nightside, typical densities lay in the range $1.5 - 2.5 \times 10^5 cm^{-3}$, rising to $3.5 - 4.5 \times 10^5 cm^{-3}$ on the dayside. These densities are representative of conditions at minimum solar activity. Features usually seemed to be most clearly defined in quiet magnetic conditions, and indeed appeared to "wash out" with appreciable magnetic disturbance. Locally increased densities associated with storms and substorms are seen (V. Wallington, unpublished results), not necessarily in the ring-region, indicating that the latter corresponds to the second zone of enhancements reported more recently (Sato and Colin, 1969).

Using this model, it is possible to suggest qualitatively reasons for some of the apparent variability of the ionosphere from one pass to the next, even during magnetically quiet periods, if it is assumed that the whole ionization distribution can move relative to the Earth with, for example, universal time. The apparent production of ionization during the sequence of Fig. 4.5 in which a peak and a plateau of ioniza-

tion were seen to approach each other, is simply explained geometrically if the ionization moved slightly towards the dusk side with respect to the satellite track. Relative to the ionization, the tracks seem displaced and the rather different profiles indicated in Fig. 4.4 would be obtained.

In a similar way, possible explanations can be offered for the radically different sequences of Figs. 4.1 and 4.2, exhibiting either single or twin density maxima. The observations are that for a given day during November 1 - 15, either distribution was possible, but twin peaks were seen with increasing frequency as the orbit-plane precesses.

The long term increase in twin-peaked passes is clear from Fig. 4.4, where passes C and D represent tracks at the beginning and end respectively of the November data period. The day to day possibility of observing either distribution could be explained by a shift of the ionization a small distance towards the night hemisphere with respect to the November passes, such that the vehicle was only just encountering or avoiding the polar cap depletion region. An indication that twin peaks are seen in November near magnetic noon (1800 UT), when the pattern (if magnetically controlled) is towards the dayside, is also compatible with the model.

The statistical position of the boundaries of the enhancements of density at high latitude has been investigated. Because of the high latitudes involved, large differences can occur between the local solar time and the local magnetic time at a point in space. For each point, the coordinates used were the eccentric dipole time (Cole, 1963) and the generalized invariant latitude, both calculated at an altitude of 300 km. Where polar enhancements were seen in the records of N_mF_2, the position of the mid-point of the density rise was noted. From 276 observations, the position of the low latitude boundary was computed in two hour sections of time, as a function of Kp index from thirty hours before to thirty hours after the time of observation.

Somewhat fewer data are available on the high latitude boundaries

of the peaks. From 187 observations, the location of the upper boundary has been calculated, again for each two hour interval of eccentric dipole time.

The contours representing the smoothed boundaries of the ring are drawn in Fig. 4.6 for a Kp index of 3. Also shown on the same figure is the auroral oval for a 75 - 90 per cent occurrence of aurora (Feldstein, 1963), together with the contour above which latitude the flux of 40 kev electrons is less than $10^4 cm^{-2} s^{-1}$ (Frank et al., 1964), and the position of the low-latitude boundary of the trough. The flux contour is identified with the average boundary of the trapping zone. The position of the ring lower boundary is statistically more accurate on the nightside, where the density rises very sharply (see, for example, Fig. 4.5), and rather less accurate on the dayside, largely as a result of the poorer definition (smaller density gradients) near the point being measured. The position of the upper boundary of the ring showed considerable variability, and the position shown on the figure has been smoothed considerably. At such latitudes, the use of invariant latitude in organizing data ceases to have any physical justification.

From the regression equations calculated for each sector, the lower boundary of the ring was shown to move towards the equator with increasing magnetic activity. No time lag of any significance was seen between the time of the observation and the time of the magnetic index showing the best correlation with the regression. The correlations obtained, however, were in general not highly significant, reflecting the great variability of the high latitude ionosphere. Nevertheless, one of the more significant correlations and regressions towards the equator comes from the 0 - 0200 hr time sector, where from the December data for 16 clear peaks the equation for the position Λ' in invariant latitude of the lower boundary was

$$\Lambda' = 65.3 - 2.3 \text{ Kp}$$

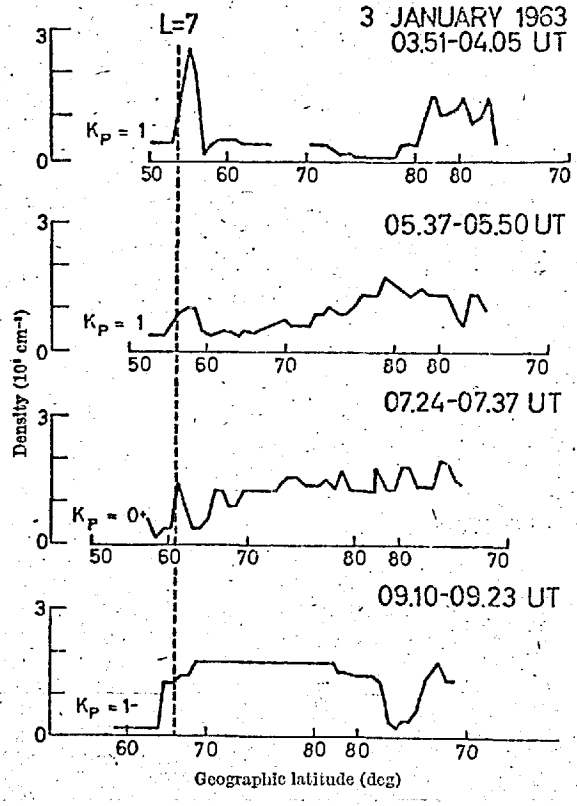


Fig. 4.5 The density N_mF_2 of the F layer peak seen on four successive passes during a very quiet magnetic period when the vehicle was travelling in the direction of the passes A and B of Fig. 4.4. A rise to higher densities is consistently seen about L = 7, but at higher latitudes a large apparent production of ionisation occurs as time increases. This may be related to an effective track displacement as indicated in Fig. 4.4.

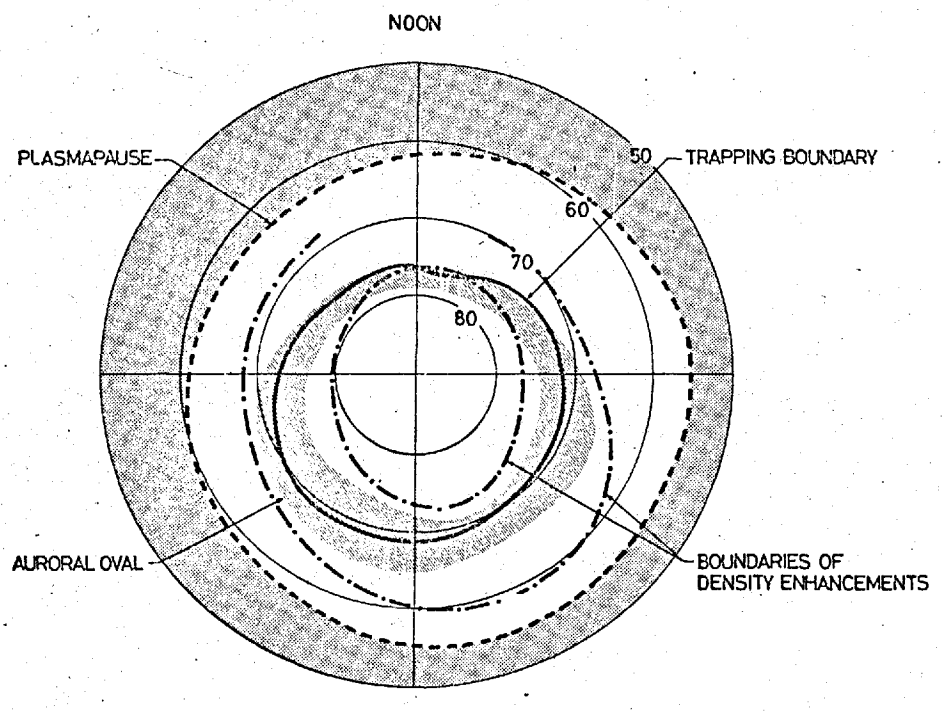


Fig. 4.6 The relative location of various high latitude phenomena in terms of invariant latitude and local time for a Kp value of 3. The plasmapause in the ionosphere is taken to be the low latitude boundary of the trough. The smoothed upper and lower boundaries of the high latitude ring of enhanced electron density are shown, and are seen in relation to the visual auroral oval.

and the correlation coefficient was 0.70. This is in contrast with the low latitude boundary of the trough, where the correlation of position with magnetic activity was highest in the evening sector and almost zero at midnight. This behaviour underlines the essentially different nature of the ionosphere at high latitudes compared with that at latitudes below the trough.

The density distribution discussed is applicable only to the winter hemisphere. During the summer months, the whole of the polar cap is illuminated continuously and there is little evidence of the peaks and depletions seen in winter. This is not to say that there are no differences between the polar and mid-latitude ionospheres. As over the winter-pole, the summer high latitude ionograms show more trace spreading and are generally more disturbed than those from lower latitudes; again, the transition from one type to the other may take place over a narrow range of latitude. The evidence of the continuing disturbance of the ionosphere, together with summer-time measurements of electron precipitation (Maelhum, 1968) probably indicates that the absence of the peak structures at this time is a result of the increased photo-production of ionization.

4.3 Comparison with other Results

The distribution of ionization above the winter pole derived in this survey may be compared with results reported by workers using different techniques.

Using results from Alouette I N(h) analyses published by the Canadian Defence Research Establishment, Nishida (1967) has produced computer averages of electron density over the north polar cap in the form of density contours on maps of corrected local time and corrected geomagnetic coordinates (Hakura, 1965). The crescent shaped trough on the nightside is apparent, but the chief difference is that there is no

suggestion of a polar depletion region. The difference could arise in that automatic averaging will lose features which do not occur consistently at a particular latitude. The mesh size used by Nishida was fairly large: 2hr of local time and 4^{o} of latitude. A grid of these dimensions is necessary in practice to encompass sufficient data points so that the standard deviations in the averaged quantities are low. To avoid these inherent difficulties, we have considered the density variations along individual tracks inclined at approximately the same angle to the Earth-Sun line, and built up a model from the characteristic shapes observed. Probably of more significance in explaining Nishida's result is the fact that the Canadian data was biased in favour of high density ionograms (G. L. Nelms, private communication, 1969).

Comparison with ground-based data is difficult because of the scattered nature of the sounding stations. Results comparable with these are contours of constant critical frequency at various universal times for winter days in the southern hemisphere (Sato and Rourke, 1964), and similar contours, though in the form of monthly averages, for several universal times over the North Pole region (Sato, 1959). A comparison of the data in these two references shows that in essence the same density configuration is present in both hemispheres, in spite of the fact that the relationship between magnetic and geographic coordinates differs considerably in the two regions. This configuration was described as a tongue of ionization extending into the polar cap from the solar direction. A diagram from the first reference is redrawn in Fig. 4.7. Although the results are in terms of geographic latitude, the crescent-shaped trough is evident and is wider on the dawn side than on the dusk side. Although, again, no polar cap depletion is shown, the tongue structure seems equivalent to the high latitude ring of ionization. This data relates to the I.G.Y., which was characterised by much more solar activity than the quiet 1962-63 period, and it is not impossible, on the evidence

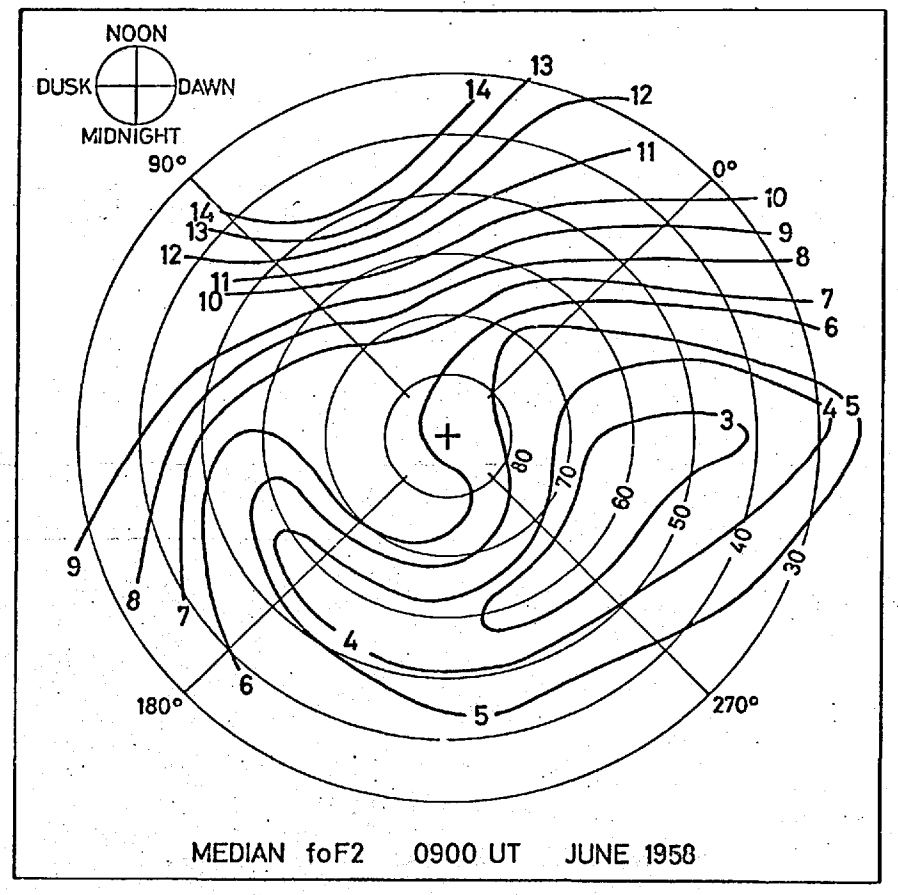


Fig. 4.7 Contours of monthly median critical frequency f_oF_2 (in Mc/s) at a particular universal time across the south pole (from Sato and Rourke, 1964). The tongue of high density plasma entering the the cap from the dayside corresponds to the present high latitude ring of ionisation, and the elongated depression of density on the nightside is the ionospheric trough. Geographic latitude and longitude are indicated.

of optical data (Eather, 1969) that under the extreme I.G.Y. conditions, the polar depletion was not present.

The approximately stationary density distribution above the poles described here should give rise to detectable effects in the ionosphere data of stations rotating beneath it. This may be investigated using f-plots, or daily graphs of frequency data read from ionograms.

College, Alaska, at a magnetic latitude of 65°, is an auroral zone station; that is, it lies inside the position of the auroral oval and within the zone where, from topside studies, density enhancements might be expected. Winter f-plots show that the dayside records are normal, with the density peaking shortly after noon, but that during the night hours, if the station is not covered by a layer of blanketing sporadic E, reflexions may be obtained from anomalously dense layers. Such reflexions may commence suddenly and are frequently spread, suggesting an irregular reflecting medium.

Resolute Bay, at 83° magnetic latitude, lies above the auroral oval. The geographic latitude of this station (75° N) ensures that the sun does not rise below an altitude of 70 km during mid-winter, at which time the minimum solar zenith angle is $98^{\circ} - 99^{\circ}$. f-Plots for this station during winter 1962 - 63 show that the night enhancements of F-region density are rarely seen, but that frequently the overhead density peaks around noon. The values of f_0F_2 are commonly 6 MHz, which is excessively high for photoionization at zenith angles of the order of 100°. It has been found that this daytime peak density correlates slightly negatively with magnetic activity, i.e. the density is greatest for quiet conditions. On the other hand, it will be shown that the density enhancements on the dayside correlate positively with Kp. Such diurnal behaviour is what might be expected from a station rotating predominantly inside the eccentric central core of density (which expands equatorwards with increasing Kp), and intersecting it slightly on the dayside. King et al. (1968)

have suggested that many of the density fluctuations at high latitude stations are caused by the component of a horizontal neutral wind forcing ionization along field lines. Such an explanation must be inadequate for the large density fluctuations seen at Resolute Bay, for the near-vertical field (dip=89°) would give a negligible force component along the field lines.

It seems likely that the phenomenon of layer replacement such as that noted at Halley Bay (Bellchambers et al., 1962), in which a denser layer appeared over the ionosonde during the night hours, is the same effect as that described previously for an auroral zone station. Bellchambers et al. noted that if the new layer was considered to be at the same height as the old, then a relative speed of advance could be deduced for it. This consistently appeared as 70 m/s, with extreme values of 40 and 150 m/s. The geographic latitude of Halley Bay is 75.5° S, so the radial speed of the station is 116 m/s. Measurements show the low latitude boundary of the inner ring of ionization moves towards the equator with increasing magnetic activity; from the consideration of oblique echoes, Bellchambers et al. conclude that in very quiet conditions the replacement layer did not extend over Halley Bay, and on disturbed days the layer was seen "abnormally early". These facts are consistent with the passage of the station under a pattern of higher density which expands with magnetic activity.

The position of the polar cap boundary in Fig. 4.6 is an averaged one. From data examined, it is clear that while a depletion is usually seen at high latitudes on the night-side, some dayside passes show enhanced densities extending to the magnetic pole. While the basic ring of enhanced density is similar in position to the auroral oval (Feldstein, 1963), or to the zone of inferred soft particle precipitation (Hartz and Brice, 1967), both of which are at their highest latitudes on the dayside, the latter do not show ovals extending as far as the pole itself. It is

thought the explanation may be linked with drifts. Magnetospheric circulation implies that there is, possibly at all times, a distant convectionpattern which is responsible (via the motion of field lines across the polar cap from a direction somewhat west of the sun) for the setting up of the DP2 current system in the lower ionosphere (Nishida, 1968; Axford, 1969). At F-region altitudes, the field line motion should cause ionospheric drifts by convecting exospheric ionization along with the lines of force. The effect of this would be both to obscure the morning trough by introducing plasma from lower latitudes, and to drag the ionization formed in the ring enhancements to higher latitudes.

Certainly, the relative positions of the auroral oval (the significance of the boundary of which is merely a certain percentage probability of the occurrence of aurora) and the lower boundary of the density ring naturally suggest that the higher densities are the result of soft particle bombardment. Some support is lent to this view by the very irregular nature of the ionosphere in the peaks as inferred from ionograms, and from the thin sheets of ionization seen at high latitudes which suggest collision ionization. If, however, auroral region precipitation is the basic cause of the high latitude ring of ionization, it remains to be explained quantitatively why densities in the afternoon are greater than at night, and why it is that the densities in the midnight sector, which experiences most auroral activity, are not greatest. This is probably related to the energy spectrum of the precipitating flux. Recent measurements on low energy (< 5 keV) electrons (Maelhum, 1968, Burch, 1968) indicate that these particles, which would cause F region ionization, show a "polar cavity"; that is, there is no flux at very high latitudes.

There is in addition a day-night asymmetry in the high latitude boundary of the flux. A quantitative estimate of the ionization these fluxes would produce is made later.

5: The Effects of Precipitating Particles

5.1 High Energy Fluxes

The role of particle precipitation in ionospheric processes has been the subject of considerable speculation, and apparently conflicting effects have been suggested. This arises from the possibility of both ionisation production, and of increased losses as a result of energy dependent loss processes.(Thomas and Norton, 1966). Probably the energy spectrum of the incoming particles will determine which effects will predominate. Rees (1963) showed that electrons of initial energy below 1 kev will deposit most of their energy above 150 km, and might therefore be expected to cause appreciable F-region ionisation. On the other hand, most of the energy of a 40 kev electron is absorbed near 100 km and so will produce most effect here, though it may have secondary effects at greater altitudes.

The fact that Alouette I carried both a charged particle detector and a sounder enables a search to be made simultaneously for precipitation and its effects. A limitation lies in the fact that the detector had a 40 kev threshold for electrons, so that it measured only the energetic tail of any flux which might be absorbed by the ionosphere. In particular, ionospheric effects were sought related to the narrow and isolated "spikes" of 40 kev electrons found on the nightside of the polar cap (McDiarmid and Burrows, 1965), and thought to be related to the islands of flux observed in the earth's magnetic tail (Anderson et al., 1965). That intense bursts of low energy electrons have not been detected at these latitudes suggests they were primarily a high energy phenomenon; indirect evidence indicates that at least some of the electrons were untrapped.

Of 36 documented events (J. R. Burrows, personal communication),

40% showed isolated sporadic E patches on topside ionograms, usually within a degree (or one ionogram) of the spike. No quantitative relation was seen between the E_s top frequency and the flux, but this is not surprising given the nature of E_s reflections, and the fact that the flux measurement is an integral one, including particles penetrating well below the E-region.

Though topside ionograms often showed anomalous disturbances and absorption near the fluxes, no single effect was observed. Indications are that hard precipitation can at times cause a localised drop of N_mF_2, together with increased scale heights throughout the topside which may result in an increased density at 1000 km. This suggests both raised temperatures and greater loss rates, both of which have been anticipated (Cole, 1967, Thomas and Norton, 1966).

5.2 Fluxes of Low Energy

Measurements of low-energy fluxes of electrons at high latitudes were made first by the Lockheed group (Evans et al., 1966) and more recently by Burch (1968) and Hoffman (1969), who extended the observations away from the noon-midnight meridian. The significant feature of all these experiments has been the detection of high fluxes of soft electrons extending to latitudes somewhat above the optical auroral zone, before they fall (by typically two orders of magnitude) over the polar cap itself. The fluxes as seen by satellite have a burst-like appearance, but it is not clear whether this represents a spatial or temporal effect. The Lockheed experiment could also detect protons above 4 kev. They report (Sharp, Carr and Johnson, 1969) that the proton energy is about 10% of that carried by the electrons. Sandford (1969) has deduced from optical data that under quiet conditions, electrons carry 99% of the incoming energy over the entire polar cap.

The Aurora I satellite (Burch, 1968) measured differential energy

spectra, with a lowest channel of 48 - 280 ev, and clearly showed that spectra in the optical auroral zone are harder than in the higher latitude, 'soft' zone. The average soft zone spectra found were (Burch, 1969)

$$J = 2.7 \times 10^{7} E^{-1.48} / cm^2 / ster / kev / sec \qquad \text{(Nightside)}$$

$$J = 3.0 \times 10^{7} E^{-2.26} / cm^2 / ster / kev / sec \qquad \text{(Dayside)}$$

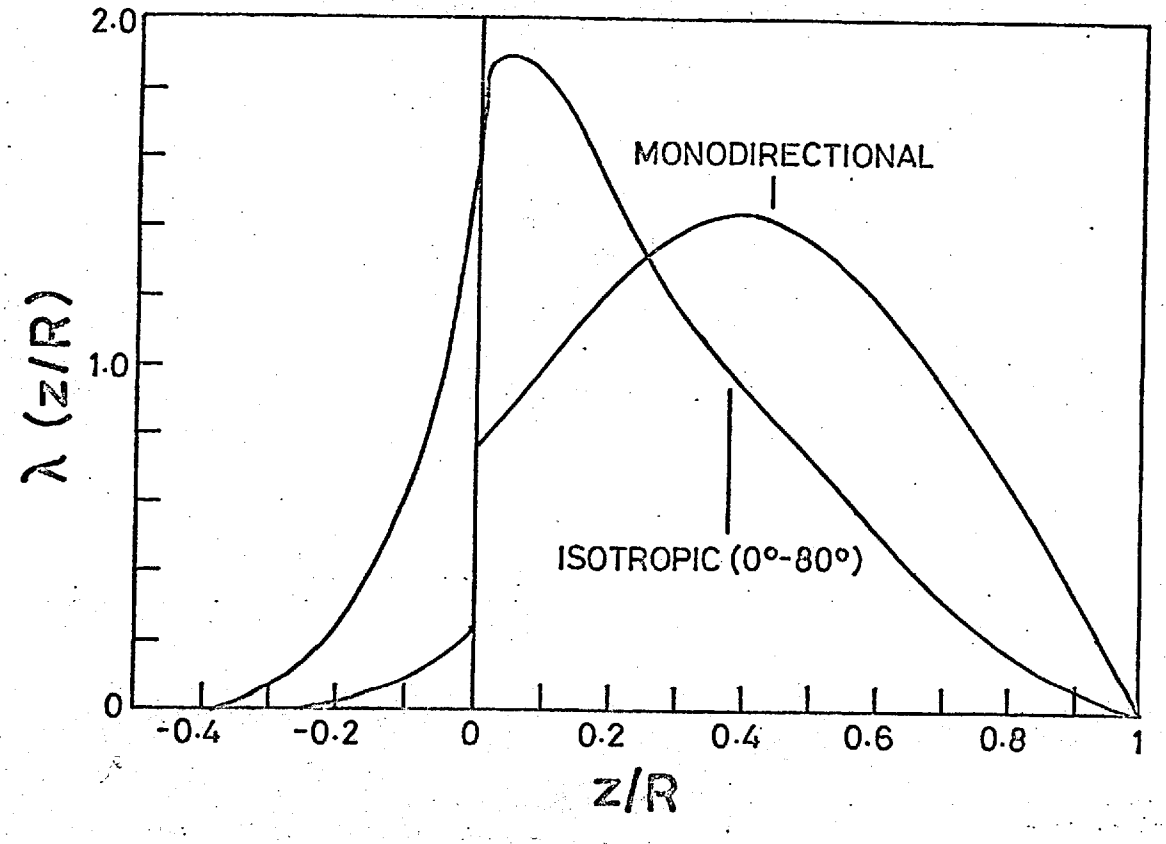
though individual fluxes may be much greater.

The mean polar boundaries of the soft electron fluxes observed over North America (from Maelhum, 1968) are compared in Table 5.1 with the present electron density measurements. Λ_D and Λ_N are the invariant latitudes of the day and night limits of the polar cavity in the noon-midnight meridian, measured in degrees.

TABLE 5.1

Observation	Λ_D	Λ_N	$\Lambda_D - \Lambda_N$	Cavity size
electrons, .08 - 21 kev, winter 1963	78	72	6	30°
electrons, .05 - 1 kev, summer 1967	83	72	11	25°
plasma density, Kp=3, winter 1962	76	73	3	31°

The agreement is reasonable, particularly when allowance is made for the fact that Λ_D for the plasma density is low. This arises because dayside passes which show only a single peak of density do not enable the boundary (implied at a very high latitude) to be determined. Table 5.1 strongly suggests that the soft precipitation is responsible for much winter polar ionisation, and an effort has been made to estimate quantitatively the ionising effect of these fluxes. There are some uncertainties in this, relating principally to the lack of pitch angle information in calculating production rates, and to some confusion over the recombination rates of the ions formed.



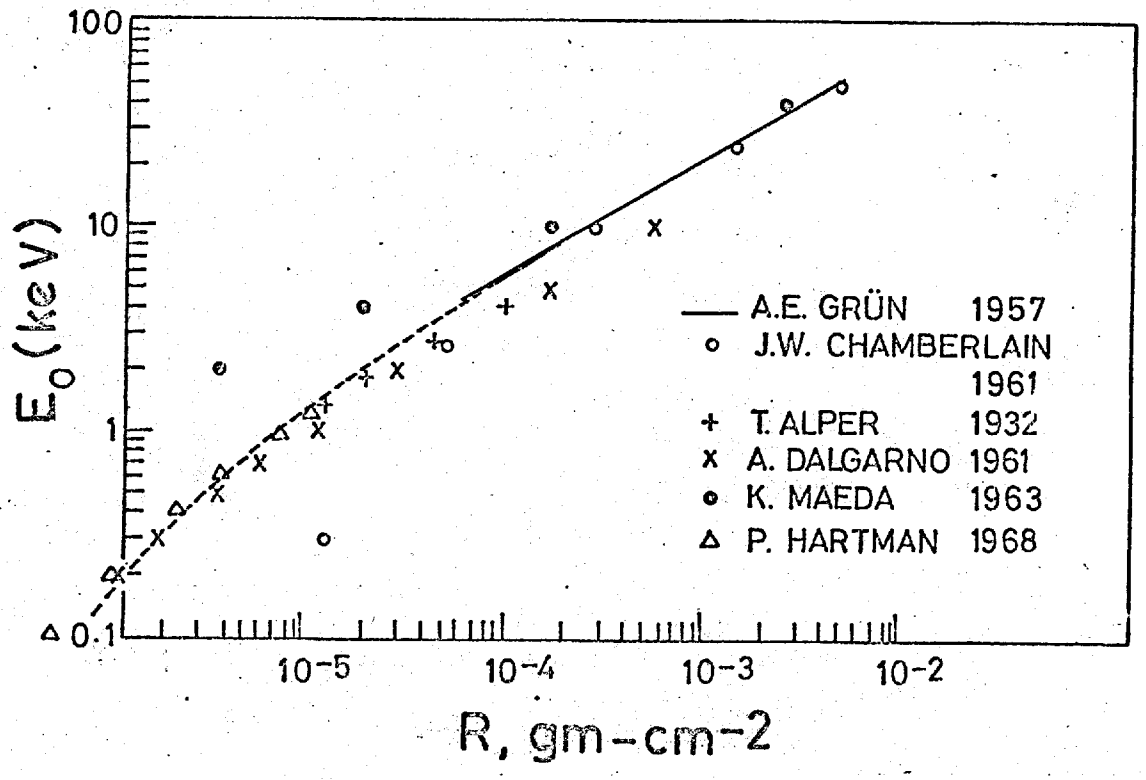


Fig. 5.1 Upper: The energy dissipation distribution function λ as a function of the penetration fraction z/R for two incident angular distributions of electrons. Lower: The range R of a primary electron of initial energy E_o.

(From Rees, 1964)

5.3 Estimated Production Rates

The theoretical calculation the atmospheric absorption of an energetic electron is a lengthy process which must be approached by a Monte Carlo technique (Maeda, 1965). Rees (1963) introduced a much simplified technique based on the measured absorption of a mono-energetic beam of electrons as it traversed a gas. In this way, all orders of scattering are included, and the question of collision cross-section is avoided. The production calculation is based on the experimentally synthesised, normalised energy dissipation distribution function, $\lambda(z/R)$, (Grün, 1959). This gives the energy fraction deposited at a depth z in the atmosphere by a mono-energetic flux which penetrates maximum distance R, the range. Grün found λ was substantially independent of the particle energy, though Maeda (1965) has questioned this at low energies. The values of R used here are those given by Rees (1964), together with some new results (Hartman, 1968) which extend the energies to 100 ev. The function λ, and the range data are shown in Fig. 5.1.

The effect of the magnetic field is neglected. This is permissible for an extended precipitation source in a uniform field (Rees, 1964), but in any case, in the absence of pitch angle information, the proportion of particles magnetically reflected before suffering atmospheric collisions is unknown.

The model atmosphere used is CIRA 1965, 1400 hrs, for a solar 10.7 cm flux of 150×10^{-22} w/m^2/c/s, which is somewhat higher than that prevailing in 1962 - 63. Atmospheric models, however, are constructed for mid-latitudes, and these parameters were selected to approximate to low solar activity, but higher temperatures corresponding to polar latitudes. Properties of the atmosphere are listed in Table 5.2. Depths in the table are in units of gm/cm^2, which for a homogeneous absorber is (density x length). For the inhomogeneous atmosphere, at altitude h, the depth is given by

$$z = \int_h^\infty \rho \, dh \qquad \text{where } \rho \text{ is the density}$$

$$= \frac{1}{g} \int \rho g \, dh \quad = \quad \frac{P}{g}$$

i.e. the ratio of the pressure at h to gravity , if g is constant.

The energy deposited between depths z and z + dz from electrons of initial energy E is by definition

$$\delta E = J \frac{E}{R} \lambda(z/R) \, dz \, dE \text{ ev/cm}^2\text{/sec},$$

where J.dE = flux component with initial energy between E and E + dE

R = range of particle with energy E, in gm/cm^2.

From the definition of z,

$$dz = \rho(z) dh,$$

so that the energy is deposited per true distance dh = dz/ρ(z), and the energy deposited per unit volume is

$$\delta E = J \frac{E}{R} \lambda(z/R) \rho_z \, dE \text{ ev/cc/sec}$$

For primary energies above 100 ev, 35 ev is required for the production of one ion-electron pair. As the major constituents above 200 km are O and N_2, the ions formed will be O^+ and N_2^+. The latter rapidly recombines, (and therefore the emitted radiation is a good experimental indication of production rates) consequently making little contribution to the steady-state density. We are then concerned only with the production of oxygen ions, and make the assumption that within a volume, the production of an ion species is proportional to its contribution to the total mass density. This is not quite true, as each species does not exhibit quite the same ease of ionisation (Rees, 1969). In addition, Fite and Brackman (1959) concluded that approximately $\frac{1}{3}$ of oxygen molecules produce O^+ on electron bombardment by the process

$$O_2 + e \longrightarrow O^+ + O + 2e$$

HEIGHT Km	$\log_{10}\rho$, (gm/cc)	P, (dynes/cm^2)	$\log_{10}z$, (gm/cm^2)
80	-7.739	9.74×10^{0}	-1.9914
85	-8.127	3.98	-2.3788
90	-8.515	1.63	-2.7670
95	-8.929	6.97×10^{-1}	-3.1343
100	-9.396	3.09	-3.4868
105	-9.662	1.48	-3.8069
110	-9.992	7.69×10^{-2}	-4.0904
120	-10.602	2.73	-4.5391
130	-11.073	1.33	-4.8508
140	-11.409	7.91×10^{-3}	-5.0731
150	-11.674	5.20	-5.2541
160	-11.839	3.65	-5.4067
180	-12.239	2.04	-5.6576
200	-12.513	1.25	-5.8697
220	-12.745	8.21×10^{-4}	-6.0462
250	-13.040	4.66	-6.2882
300	-13.453	2.04	-6.6421
360	-13.876	8.58×10^{-5}	-7.0101
400	-14.126	5.04	-7.2351
500	-14.690	1.49	-7.7520
600	-15.197	5.01×10^{-6}	-8.2125
700	-15.662	1.86	-8.6308
800	-16.094	7.80×10^{-7}	-9.0250
1000	-16.824	1.60	-9.6615

HEIGHT Km	N	$n(N_2)$	$n(O_2)$	n(O)	n(He)	n(A)
80	14	2.963	0.795	-	-	0.035
85	14	1.212	0.325	-	-	0.014
90	13	4.965	1.33	0.01	-	0.06
95	13	1.94	0.52	0.03	-	0.02
100	12	8.18	1.99	0.50	-	0.01
105	12	3.45	0.79	0.36	-	0.04
110	12	1.62	0.35	0.20	-	0.02
120	11	4.00	0.74	0.76	-	0.04
130	11	1.34	0.23	0.35	-	0.01
140	10	6.10	0.95	2.03	-	0.04
150	10	3.25	0.47	1.32	-	0.01
160	10	1.92	0.26	0.92	-	0.01
180	9	8.20	1.02	5.25	-	0.02
200	9	4.11	0.47	3.37	-	0.01
220	9	2.26	0.24	2.33	-	-
250	9	1.03	0.10	1.44	-	-
300	8	3.17	0.26	7.17	0.04	-
360	8	0.86	0.06	3.38	0.04	-
400	8	0.38	0.02	2.10	0.03	-
500	7	0.51	0.02	6.68	0.25	-
600	7	0.07	-	2.22	0.19	-
700	6	0.11	-	7.65	1.46	-
800	6	0.01	-	2.71	1.13	-
1000	5	-	-	3.50	6.60	-

Table 5.2. CIRA 1965 for conditions given in the text.
The lower table gives the particle concentrations per cm^3, when multiplied by 10^N (column 2)

This was not taken into account as the molecular oxygen concentration is low at F-region altitudes. With these assumptions, the production rate of ions of the i-th species due to all incident energies is

$$Q_i(z) = \frac{1}{35} \int_E J \cdot \frac{E}{R} \lambda(z/R) \rho_z \frac{\rho_i(z)}{\rho_z} dE$$

Assuming that the fluxes found by Burch (1968) were isotropic over the lower hemisphere, the maximum production rates of O^+ in the soft zone due to electrons with initial energies between .1 and 10 kev were estimated as follows

	Q_{max}, cm^{-3} sec^{-1}	Altitude, km
Day	255	235
Night	270	180

Because of the softer dayside spectrum, the dayside production above 300 km is twice that on the nightside. These peak rates may be compared with the measured photon flux at mid-latitudes at a similar solar epoch (Hinteregger and Watanabe, 1962), from which Yonezawa (1966) estimated the maximum production of all species to be 800/cc/sec. Hoffman (1969) reports some fluxes are strongly mono-directional, which would have the effect of raising production rates near the F-layer peak.

5.4 Electron Densities

To estimate the electron densities these production rates produce, it is essential to include the effects of ambi-polar diffusion above 200 km altitude. For ease of solution, diffusive equilibrium was assumed to exist at 1000 km, though as discussed subsequently, this may well break down over certain regions of the polar cap.

The coupled equations of motion of the ions and electrons in a vertical magnetic field at a level z (positive downwards for reasons of computation) are (e.g. Nisbet, 1963)

$$m_i \nu_{in} v_i = m_i g - qE - \frac{k}{n_i} \frac{d}{dz} (n_i T_i) \qquad (5.1)$$

$$m_e \nu_{en} v_e = m_e g + qE - \frac{k}{n_e} \frac{d}{dz} (n_e T_e) \qquad (5.2)$$

Here q = modulus of the electronic charge

E = electric field due to charge separation in the ionosphere, and all other terms have their usual significance. A single ion constituent (O^+) has been assumed, the justification for which is considered later. These equations are valid while the inertial terms due to ion and electron acceleration are small compared with the collision terms. This is reasonable for a minority constituent where the collision time is not too large, such as ions moving through the topside ionosphere, but for greater altitudes, the full momentum equations must be used (Banks and Holzer, 1968).

Assuming charge neutrality,

$n_e = n_i = N$, the charged particle density

and so $v_i \simeq v_e = v$, the diffusion velocity

Since $m_i \nu_{in} > m_e \nu_{en}$, the ambipolar diffusion flux may be written approximately as

$$Nv = - \frac{Hg}{\nu_{in}} \left[\frac{N}{H} \left(1 - \frac{dH}{dz}\right) - \frac{dN}{dz} \right] \qquad (5.3)$$

where $$H(z) = \frac{k(T_i + T_e)}{m_i g}$$

and $\frac{Hg}{\nu_{in}}$ is the ambipolar diffusion coefficient Da for a vertical magnetic field.

The steady state continuity equation, in the absence of horizontal movement, at level z is

$$Q - L - \frac{d}{dz} (Nv) = 0 \qquad (5.4)$$

where Q and L are the rates of production and loss per unit volume.

Equations 5.3 and 5.4 yield a second order differential equation, which has been solved by a fourth-order Runge-Kutta technique from an altitude of 1000 km, where diffusive equilbrium was assumed (i.e. Nv = 0 in 5.3) to a level where diffusion is again small, here 180 km. This introduces a second constraint, namely that within these limits, the integrated production and loss rates must be equal.

The scale height H was matched to experimentally derived polar values, where O^+ is the dominant ion, by a linearly increasing function, rising from 80 km at a height of 150 km, to 200 km at 1000 km. The latter corresponds to $T_i + T_e = 3780^oK$ if $g = 980$ cm/sec^2.

An altitude dependent scale height introduces an extra height dependence into the diffusion coefficient, but this is partly compensated by a similar temperature dependence of the collision frequency ν_{in} (Dalgarno, 1964). These variations are much smaller than that introduced by the exponentially falling neutral density. The value assumed was

$$Da = 2 \times 10^{-19}/(\text{neutral density}) \qquad (\text{cm}^2\ \text{sec}^{-1})$$

(Dalgarno, 1964; Yonezawa, 1966)

The loss processes at the altitude concerned were taken to be dissociative recombination with the rate determining interchange processes

$$O^+ + N_2 \longrightarrow NO^+ + N \qquad (\text{rate } k_1)$$

$$O^+ + O_2 \longrightarrow O_2^+ + O \qquad (\text{rate } k_2)$$

$$N_2^+ + O \longrightarrow NO^+ + N \qquad (\text{rate } k_3)$$

Torr and Torr (1969) have reviewed the laboratory data on the rate coefficients and concluded that at ionospheric temperatures, representative values, in cm^3/ sec are:

k_1	k_2	k_3
2×10^{-12}	2×10^{-11}	2.5×10^{-10}

The high value of k_3 ensures the rapid removal of N_2^+ ions, and

justifies the omission of this species in the transport equations. The rate of removal of oxygen ions (assuming the dissociative recombination processes go quickly enough to ensure that $[O^+] = N$, the electron density) becomes

$$L = k_1 \cdot [N_2] \cdot N + k_2 \cdot [O_2] \cdot N$$

Throughout most of the F-region, molecular oxygen densities are well below those of nitrogen, and this leads to an approximate expression

$$L = 2 \times 10^{-12} \times (\text{molecular density}) \times N \qquad (5.5)$$

There is therebye a discrepancy between this laboratory rate and that inferred from the ionosphere, e.g. Yonezawa (1966). From the latter, the numerical coefficient in (5.5) is $.65 \times 10^{-12}$. Both values have been used in the computations, the results of which are presented in Fig. 5.2 and Table 5.3 for production rates corresponding to the day and night zones of soft electron precipitation.

TABLE 5.3

	Loss coefficient	f_0F_2, Mc/s	h_mF_2, km	$h(Q_{max})$ km
Day	2×10^{-12}	5.2	320	235
	6×10^{-13}	7.3	290	
Night	2×10^{-12}	4.1	315	180
	6×10^{-13}	6.0	290	

The range of critical frequency, or density, in the table is in good agreement with the measured densities reported in Chapter 4, and it is concluded that soft electron fluxes must play a major role in the maintenance of the polar F-region.

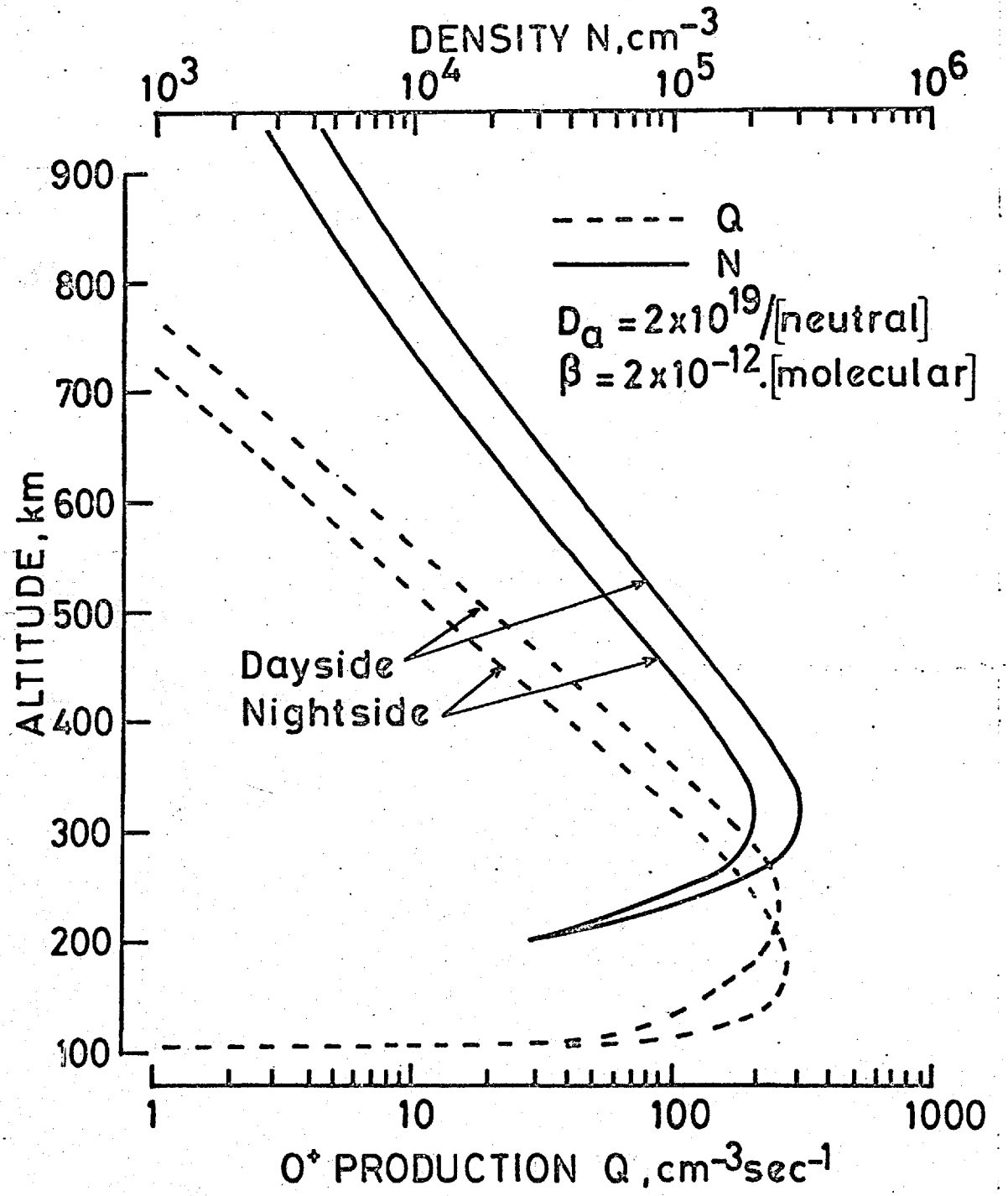


Fig. 5.2 The computed oxygen ion production rates caused by the soft electron fluxes at high latitudes, and the resulting electron density N in the ionosphere after allowing for loss and plasma diffusion using the parameters indicated. Dayside and nightside values refer to estimates in the noon and midnight sectors respectively.

6: Polar Densities and Universal Time Effects

6.1 Densities and Magnetic activity

It is reasonable to expect geomagnetic activity to have a bearing on exospheric electron densities. At mid-latitudes, Titheridge (1968) has found significant negative correlations between ionospheric electron content and magnetic activity. This was ascribed to the known increase in molecular particle concentrations at disturbed times (Reber and Nicolet, 1965), which should accelerate the loss of O^+. Alternatively it has been found in the laboratory that the rate of the loss-governing reaction

$$O^+ + N_2 \longrightarrow NO^+ + N$$

is strongly dependent on temperature and on vibrational excitation of N_2, (Bohme et al., 1967, Schmeltekopf et al, 1967). Both of these effects might be expected to occur during times of magnetic activity, leading to depressed electron densities.

In the winter polar ionosphere, there is no reason to believe that increased loss rates should not be present during storms, but there is the difference that here it is believed most of the ionisation is caused by precipitating particles. No information has yet been published on the magnetic dependence of the soft fluxes; though Burch (1968) considers them to be less affected by magnetic activity than fluxes of higher energy. Two approaches can be made; the effect of magnetic activity on the average background level of density, and secondly, its effect on the precipitation produced density peaks may be investigated.

To obtain a figure for the background density, up to six values of f_xF_2 were read from graphs of this quantity on polar transits at 10^o intervals of geocentric arc. These values were converted to F-peak electron density, assuming a gyrofrequency of 1.3 Mc/s (the variation of f_H

across the polar cap at F-peak heights is about 1.25 - 1.4 Mc/s), and then averaged to give a mean value of electron density over that pass. This was done for the last three months of 1962, and June 1963. Intercomparison of the data (shown graphically in Fig. 6.1) is not generally possible as the range of local times sampled differs from month to month (see Fig. 3.2). This is not the case with the December and June results, where in each case, the vehicle was travelling directly towards the sun, enabling a direct comparison between summer and winter densities to be made. This shows those in summer to be a factor of 2 - 3 times greater than winter values. The number beside each point in Fig. 6.1 gives the number of passes included in the average.

When considered against the current Kp index (i.e. that prevailing at the time of the observation), no clear general trend is apparent. Thus the June densities tend to fall with magnetic activity while there was a rising trend in November which covers dayside local times. Considered as a function of the mean Kp index over the 24 hours preceeding the observation, all months show a negative density correlation with Kp which might have been anticipated on the basis of mid-latitude findings.

The effect of magnetic activity on the dayside density enhancements was investigated by correlating the size of the enhancements seen at the F-layer peak and the current Kp index. From 93 observations, the density N, in 10^4 el/cc, found in the peaks was given by

$$N = 31.22 + (2.79 \pm .85)Kp$$

The correlation coefficient was .325. The probability of this result arising randomly in the sample when the population has zero Kp dependence is less than .2% here. The dayside peaks then correlate strongly and positively with magnetic activity, though the density enhancements at other local times did not show such a strong dependence.

An examination of passes over the summer pole shows no peaks and

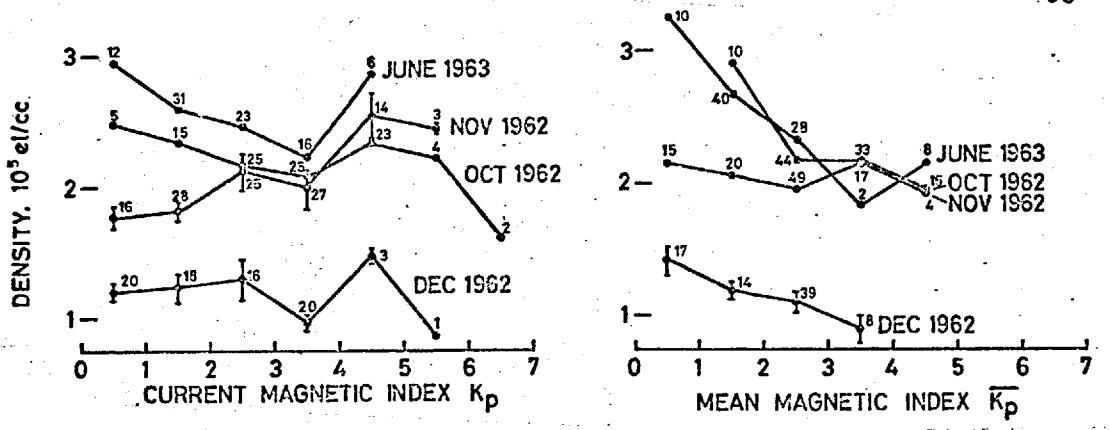


Fig. 6.1 Densities at the F peak averaged over a pass and shown as a function of K_p and $\overline{K}_p$ for different months. The numbers give the number of passes included in the average at each point.

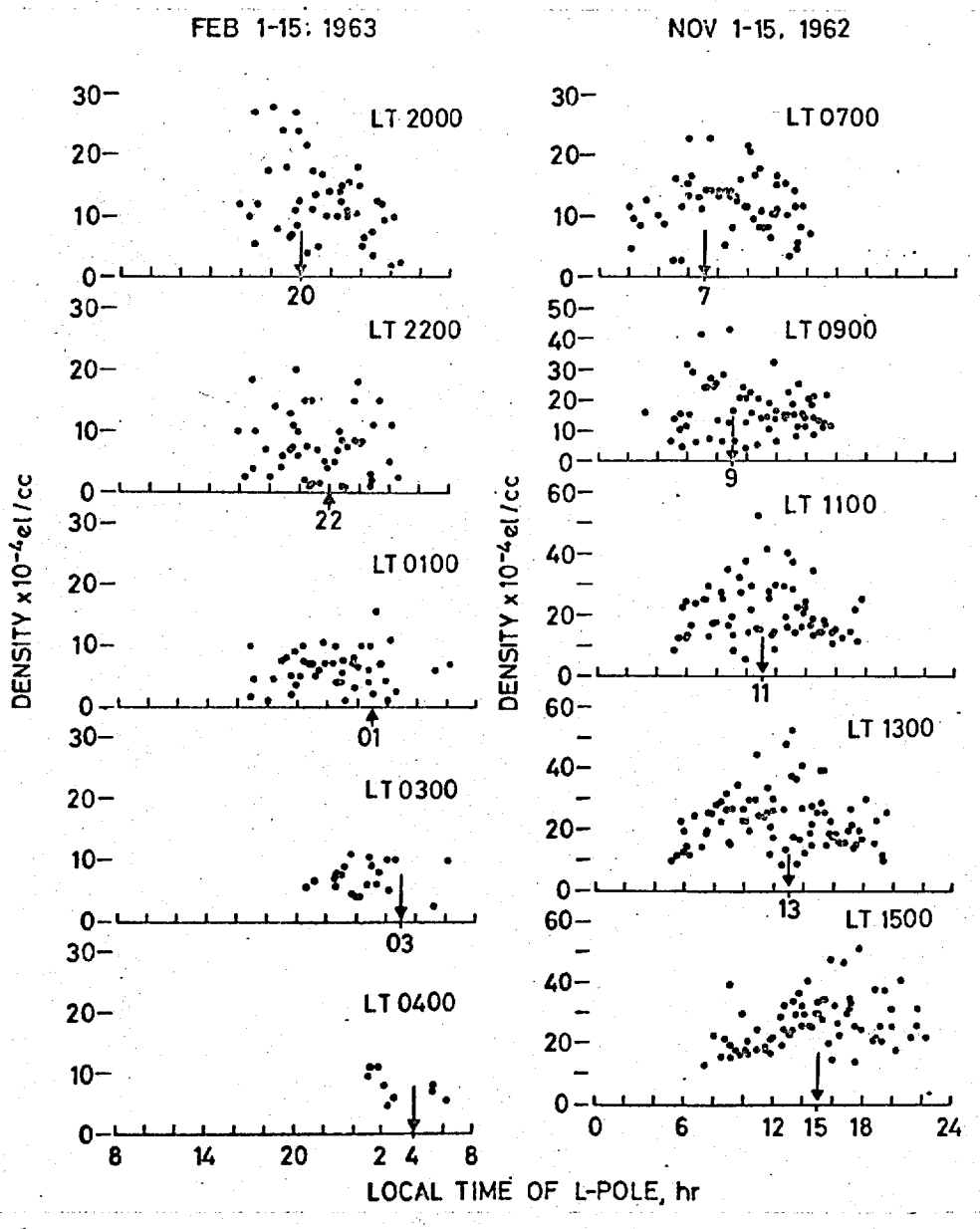


Fig. 6.2 F peak densities obtained during two months at fixed local times for different universal times. On the dayside, particularly near noon, the densities may become very high when the L pole is in the local time sector concerned as discussed in the text.

troughs of ionisation, probably as a result of the dominance of solar illumination. This may explain why the background density correlates negatively with Kp in June, and slightly positively during the winter months of November and December. The overall balance can be understood qualitatively in terms of two sources, the smaller of which (particle precipitation) depends on current magnetic activity, the second and stronger source coming during summer from ultra-violet radiation, combined with a loss rate which rises during periods of sustained magnetic activity. The results of the previous paragraph suggest too that any magnetic dependence of the soft fluxes should be greatest on the day-side.

6.2 Densities and Universal Time

An aspect of the polar ionosphere which has received considerable attention in previous years is the universal time control of the density of the ionospheric layers. The subject was treated in some detail by Duncan (1962) who concluded that the density of the whole Antarctic ionosphere was enhanced at a universal time of about 0600. The effect does not appear every day, but for example, in the case of Ellsworth, enhancements in f_0F_2 are seen at this time on about 50% of the days. A similar UT effect was noted over the Arctic ionosphere, with the difference that the enhancement then occured at 1800 UT and was rather less pronounced than in the south. Significantly, both Northern and Southern enhancements occur when the magnetic pole is towards the sun; possibly the greater separation of the geographic and geomagnetic poles causes the greater UT effect in the south.

Universal time control should be detectable in the records of density obtained by satellites. In an earlier analysis, Thomas et al. (1966) examined Alouette I data for the winter of 1962-63, and concluded that enhanced densities at 1000 km (the vehicle height) did in fact occur

at times centred about 1900 UT. The analysis did not, however, separate out local time effects, (which themselves produce density variations) as, because of the nature of the vehicle orbit and the location of the telemetry sites in the Western hemisphere, local and universal time samples are interdependent.

The Alouette I information has been re-examined using data from months when the satellite was travelling approximately perpendicular to the earth-sun line. This results in the solar zenith angle being approximately constant over each pass. Data from slightly smoothed plots of f_xF_2, obtained during November 1962 and 1963 at local times of 07, 09, 11, 13, and 15 hrs, were used to calculate the electron density at the F_2 peak when the satellite was inside the polar ionosphere at these local times, i.e. the vehicle was at a latitude above that of the plasmapause. F-peak electron densities at local times of 20, 22, 01, 03 and 04 hrs were similarly obtained from the February 1963 passes, when again the orbit plane was perpendicular to the earth-sun line. These results are shown in Fig. 6.2.

In this figure, the abscissa is taken to be the local time at the longitude of the L-pole, i.e. 80°W, and so is $5\frac{1}{3}$ hrs behind universal time; that is to say, local noon at the magnetic pole occurs between 1700 and 1800 hrs UT, the approximate time of the ground observed enhancements. The arrows in Fig. 6.2 denote when the local time at the magnetic pole coincides with the local time of the density samples.

The coincidence of the highest densities in Fig. 6.2 and the time at which the L-pole reaches the local time concerned is quite striking on the dayside, particularly near noon, i.e. 1100 and 1300 LT. This result has been confirmed by an equivalent analysis of data from November 1963, when the orbit configuration was similar. Thus densities at the peak of the F-region at a point in space may become very high when the magnetic pole approaches that point, so that a "wave" of higher density

plasma appears to follow the motion of the pole, or some point close to the pole.

There are several possible interpretations of this effect which should be considered. The universal time corresponding to the arrows in Fig. 6.2 represent the highest magnetic latitudes attained at that local time (since the L-pole is then closest to the point of observation). The evidence of this figure alone is consistent with simply a single enhancement of density over the pole itself, at least on the dayside of the earth. This eccentrically placed enhancement would then cause the progressive delay in the universal time of the maximum in the local time samples. Such an explanation is, however, inconsistent with the form of F-peak density records seen along many satellite tracks, from which a different spatial structure has been deduced. It is possible, assuming the presence of that structure, (i.e. the ring of enhanced density which is basically magnetically controlled) that the maxima of Fig. 6.2 could arise geometrically. Data points taken at a fixed local time in this work have approximately the same geographic latitude, so that their magnetic latitude fluctuates periodically throughout the UT day, as a result of the eccentricity of the geomagnetic axis. Density maxima could then arise as the observation point (in magnetic co-ordinates) moves cyclically across this pattern. This presupposes a more rigid adherence to magnetic time control than the data suggests when individual passes are examined; there is no systematic movement of the observation point across a density pattern such as would be required. In any case, if this mechanism was the cause of the UT maxima, it should be expected to be equally operative for the nightside, but this is not the case.

It therefore seems that this is a real enhancement effect, related to the magnetic pole being towards the sun, and probably the sunspot minimum equivalent of the UT control of the Arctic ionosphere recorded by Duncan. What the satellite study has shown is that although the

effect is greatest at approximately 1800 UT, the area of enhancement follows the magnetic pole across the dayside of the earth. The measurements of time-dependent enhanced densities support the suggestion that the magnetospheric configuration is more conducive to the entry of energetic particles when the magnetic pole is on the dayside; furthermore, the region of increased density is localised in space to a zone near the magnetic pole, suggesting that, for example, the dayside neutral point may be involved in the increased precipitation of particles. This conclusion may be compared with the ground-based observations of Oguti and Marubashi (1966), in which rather irregular enhancements of ionisation were seen in the F-region near geomagnetic noon for stations in the latitude range of these measurements.

6.3 Movements of the Precipitation Zone

Maelhum (1968) found that the latitude of the polar boundary of the soft fluxes showed large changes with universal time, both on the dayside and the nightside, so that the size of the polar cavity varied between 20° of arc at 1900 UT and 35° at about 0700 UT. This implies there is a ring of territory on the earth, $7 - 10^{\circ}$ in width, above which electrons precipitate at magnetic noon, but not at midnight. In a later paper, Maelhum (1969) proposed that stations within this band would see a universal time control of the ionosphere above them, due to the presence of ionising electron fluxes at 1900, but not at 0700 UT. No reports are known of UT variations in the magnitude of the fluxes, but the results of section 6.2 suggest that these might also be greatest near universal magnetic noon, i.e. about 1800UT in the north.

The data obtained from Alouette I on the poleward boundaries of the density enhancements has been examined as a function of UT, but does not support Maelhum's suggestion, though in many cases, the data is too scattered to enable a positive conclusion to be reached. When the data

is examined in monthly groups (to minimise any long-term effects of the dipole tilt angle) it seems that if any variation with UT is present, it is the same as that noted in connection with the trough motions; the boundary does not respond wholly to magnetic control, and it occurs at highest magnetic latitudes near the time the eccentric L-pole is in the local time sector of the boundaries in question. Some boundary data obtained at local times near 2000 hrs (eccentric dipole times around 1800 hrs) obtained in February 1963 illustrate this in Fig. 6.3. Though systematic trends are small, the highest invariant latitudes do seem to be reached near 0400 UT, close to the time the L-pole itself reaches 2000 LT (0200 - 0300 UT). This seems to preclude the polar density cavity reaching a maximum size (i.e. the boundary in Fig. 6.3 reaching a minimum latitude) at 0700 UT, as suggested by the particle measurements, and there remains, therefore a possible discrepancy between the two types of measurement.

Two points may be relevant here.

1) The expansion of the flux cavity has been deduced solely from measurements in the noon - midnight meridian. It does not necessarily follow that it will expand similarly in the dawn - dusk meridian if for example, it was simply distorted by the varying tilt angle of the earth's dipole.

2) Electron densities will show less magnetic control than particle precipitation, as any ionisation formed is subject to drifts for some hours until it recombines, which may account for the scatter of the electron concentration boundary data.

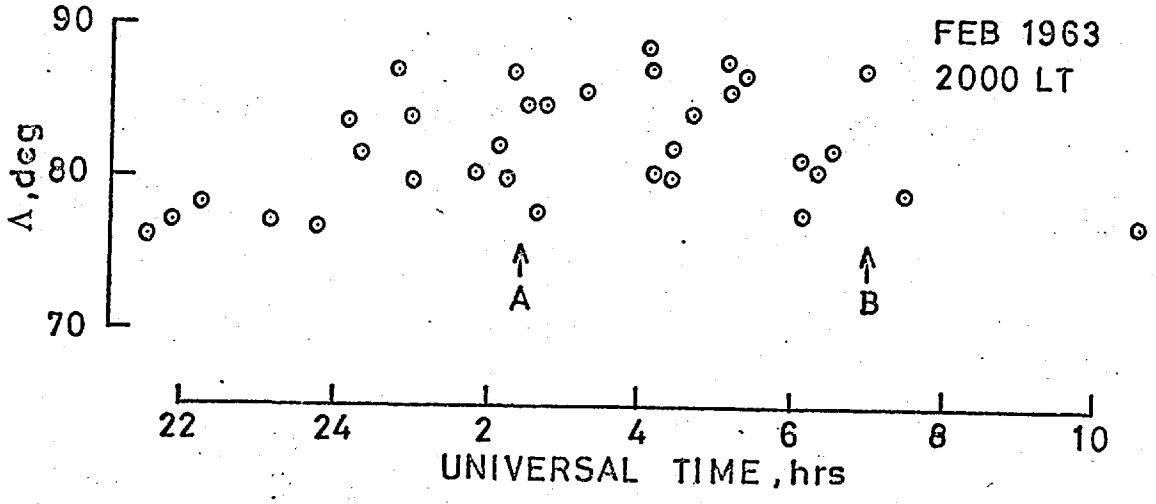


Fig. 6.3 The boundary in the polar cavity in the electron density distribution at a given local time, as a function of universal time. At the time marked B, the polar cavity in the precipitating fluxes reaches a maximum size, measured in the noon-midnight meridian. If the whole cavity expanded at this universal time, one might expect the density boundary also to reach its lowest latitude here. However, the boundary reaches its highest latitude (suggesting a smaller cavity) near the time A, when the L pole reaches the local time sector of the data. This suggests that the density enhancements, like the trough boundaries, show part magnetic, part geographic control, rather than the magnetic latitude-U.T. control of the precipitating electrons.

7: Polar Electron Density Profiles

7.1 The Breakdown of Diffusive Equilibrium

At low latitudes, the topside ionosphere is often considered to be in a state of diffusive equilibrium in regions where production and loss are insignificant. The basic reason for this is quite simple:- since the collision frequencies are low, the particles are constrained to move along field lines, and because the latter are closed, any particles rising from each hemisphere create a pressure gradient at the top of the field line which opposes and eventually halts further upward diffusion. At very high latitudes, however, the field lines may connect to interplanetary space, or go to a region of the magnetospheric tail where the plasma pressure is too low to prevent the upward flow of particles. At intermediate latitudes, e.g. near the ionospheric trough, the densities within closed field tubes are so low that it has been suggested that the collisionless treatment of Eviatar, Lenchek and Singer (1964) may apply. This treatment, though, which leads to a faster fall off in density than does diffusive equilibrium, is true only for zero collisions, and there is doubt as to its validity when applied to the steady state solution of a system with a small but finite collision frequency.

The observation at high latitudes of almost mono-energetic fluxes of electrons could mean, contrary to the usual assumptions, the existence of electric fields parallel to the magnetic field, and parallel currents. Schield, Freeman and Dessler (1969) suggest that such currents, driven by magnetospheric convection, should flow almost continuously into the auroral oval. The presence of these currents was predicted to have a large effect on the topside densities and it has been suggested that they may be linked with the formation of the trough (Block and Fälthammar, 1968).

The problem of the behaviour of the ionosphere on an essentially

open field line is mathematically similar to the expansion of the solar corona and has interesting physical consequences. The problem has been treated by Banks and Holzer (1968) on a hydrodynamic approach, though this has been the subject of some contention (Dessler and Cloutier, 1969; Banks and Holzer, 1969).

7.2 The Polar Wind

Following Banks and Holzer (1968) the equations of motion of the electrons and ions of the j^{th} species are

$$\frac{1}{\rho_e}\frac{\partial P_e}{\partial r} + \frac{eE}{m_e} = 0 \qquad (7.1)$$

$$u_j \frac{\partial u_j}{\partial r} + \frac{1}{\rho_j}\frac{\partial P_j}{\partial r} + \frac{g_o a^2}{r^2} - \frac{eE}{m_j} = -\frac{1}{\rho_j}\sum_k \frac{P_j}{D_{jk}}(u_j - u_k) - \frac{q_j}{n_j}u_j \qquad (7.2)$$

In these equations, which are coupled by the charge separation electric field E, P is the partial pressure, m the particle mass, n the concentration, and $\rho = nm$. Distances r are measured along the near-vertical magnetic field. Some approximations have been made in (7.1) as a result of the low electron mass, while the ion momentum equation is an extension of that assumed in Chapter 5, where now the inertial terms must be considered as at some altitudes, they will become greater than the drag due to ion friction with other species. The latter effect is incorporated in the first term on the right, where D_{jk} is the diffusion coefficient of the ions as they flow with speed u_j through the k^{th} species, which itself has a bulk velocity u_k. The final term in (7.2) allows for ion production q_j, which is assumed to occur with zero flow velocity.

A further equation in the steady state is provided by the conservation of charge of the individual species as they flow along a flux tube of area A, i.e.

$$\frac{\partial}{\partial r}(n_j u_j A) = A(q_j - l_j) \qquad (7.3)$$

where l_j is the species loss rate.

These three equations may be combined and the electric field eliminated to give the Mach equation, if the pressure and density are linked by the sound speed c, where

$$P = c^2\rho$$

and $c^2 = KT/m$ for a Maxwellian distribution.

In terms of a dimensionless distance co-ordinate S = r/a, where for convenience a is taken to be 1Re, the Mach equation, in terms of M_j $(= u_j/c_j)$ is

$$\frac{1}{M_j}\frac{\partial M_j}{\partial S}(M_j^2 - 1) = -\frac{g_o a}{c_j S^2} + \frac{1}{A}\frac{\partial A}{\partial S} - \frac{1}{Q}\frac{\partial Q}{\partial S} - \frac{1}{2T_i}\frac{\partial T_i}{\partial S}(M_j^2 + 1)$$

$$- \frac{1}{T_i}\frac{\partial T_e}{\partial S} - a\sum\frac{(c_j M_j - u_k)}{D_{jk}}$$

$$- \frac{T_e}{T_i n_e}\frac{\partial n_e}{\partial S} - \frac{q_j a M_j^2 A}{Q} \qquad (7.4)$$

where $$Q = a\int_{S_o}^{S}(q_j - l_j)A\,dS + nu_j A\Big|_{S_o} \qquad (7.5)$$

In (7.4), the effects of the other species enter partly through the friction term, but mainly via the electron density gradient, which by (7.1), incorporates the separation electric field. As this gradient is not initially known, and depends on all constituents, self consistent solutions to (7.4) can only be obtained by numerical techniques, though some features of the solutions can be obtained intuitively by analogy with Parker's (1967) treatment of the solar wind.

Considering only a single species, with equal ion and electron temperatures, $n_e = n_j$, and the electron pressure term may be absorbed via the continuity equation to yield a modified Mach number equation

$$\frac{1}{M}\frac{\partial M}{\partial S}(M^2 - 1) = -\frac{g_o a}{c^2 S^2} + \frac{1}{A}\frac{\partial A}{\partial S} - \frac{1}{Q}\frac{\partial Q}{\partial S} - \frac{caM}{2D_{in}} - \frac{q_i a A M^2}{Q} \qquad (7.6)$$

The diffusion coefficient is now between ions and neutrals, and c refers

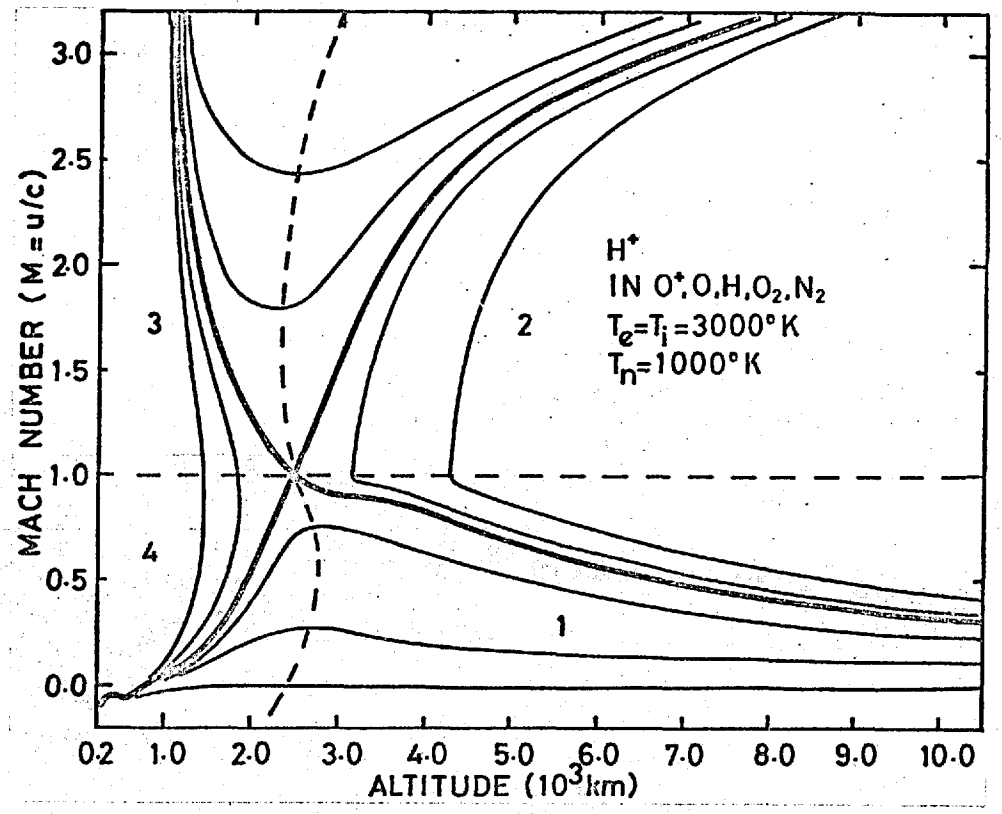


Fig. 7.1 Family of solutions to the Mach equation for protons in the atmosphere indicated (from Banks, 1969). Each curve corresponds to a given pressure at great heights. The dotted lines divide the solutions into regions characterised by slopes of the same sign. Only at the critical point, where the heavy lines (the ascending and descending critical solutions) cross, is the slope not defined. The ascending critical solution is the only one which which matches the actual boundary conditions.

to the sound speed of the plasma, $2KT/m_j$. The equation of static equilibrium ($u = 0$) does not follow from the Mach equation, as the latter is derived via the continuity equation, which assumes n and u are related. Fig. 7.1, from Banks (1969), shows a family of solutions of the Mach equation, actually for a multiple constituent ionosphere, but which are of the same form as the solutions to (7.6). Each curve corresponds to a definite pressure at infinity, and on physical grounds, those giving infinite flow speeds at low altitudes may be neglected. The origin of such a family may be seen from (7.6). For $M > 0$, all the terms on the right are negative, except for the flux divergence as initially in the ionosphere, $A \propto S^3$.

At low altitudes, and for likely temperatures, the gravitational term, augmented by the other negative terms, exceeds the tube divergence and the right of (7.6) is negative. As S increases, the last three terms eventually become zero as production and loss cease and friction decreases exponentially, while the gravitational term falls as S^{-2}, tube divergence as S^{-1}. There is therefore a critical altitude, S_c, where the R.H.S. goes through zero and becomes positive. In addition, for M greater than, or less than 1, the coefficient of $\frac{\partial M}{\partial S}$ is respectively positive or negative. Combining these observations, the sign of $\frac{\partial M}{\partial S}$ is positive or negative, depending on which "quadrant" (labelled 1 - 4 in Fig. 7.1) we are in. Thus for the fourth quadrant, $M < 1$, and as the R.H.S. of (7.6) is negative, $\frac{\partial M}{\partial S} > 0$. Along the horizontal line $M = 1$, the curves must have infinite slope, while their slope is zero along the line obtained by equating the R.H.S. of the Mach equation to zero. The slope is not defined at the critical point, which gives rise to the two heavy lines through this point, the ascending and descending critical solutions.

Curves below the descending critical solution correspond to outwards, subsonic expansion of the plasma, while there is a higher pressure at infinity which gives the solution $M \longrightarrow 0$, corresponding to the dif-

fusive equilibrium profile. However, the former solutions, with low and decreasing velocities at great altitudes, correspond to pressures in the tail an order of magnitude above those measured experimentally (Banks, 1969), and it is concluded that such steady state solutions are not possible. The only available solution giving a low pressure at infinity is the ascending critical curve, which has a supersonic velocity and zero pressure at infinity. In reality, the pressure at "infinity" is small but finite, and the expansion will proceed until the stagnation pressure of the flow (the momentum /cm^2/sec) falls to the tail pressure (Parker, 1967). The flow is then halted by a shock transition, but since this takes place beyond S_c, no signal can proceed upstream to change the conditions of the expansion.

In theory, any ion can reach a supersonic speed, as, unlike the escape of neutral constituents, energy is continuously supplied by the separation electric field, though the probability of this occurring is low for heavy ions. The critical point for O^+ and H^+ ionospheres may be found from (7.6) by equating the gravitational and field divergence terms, on the assumption that production, loss, and friction are small at S_c. For $A \propto S^3$, and $T = 1000^oK$, we have

$$S_c(H^+) = 1.25 \text{ Re}$$
$$S_c(O^+) = 20 \text{ Re}$$

Retrospectively, the neglect of friction at S_c was justified for oxygen, but not for hydrogen, though the probability of oxygen reaching such altitudes and speeds is low.

The locus of the point of zero slope of the Mach curves (shown as the near vertical dashed line), is obtained by putting the entire R.H.S. of (7.6) equal to zero. Immediately it is clear that the locus is a function of M, unlike the solar wind case, where this locus was a straight line at a fixed altitude. Qualitatively, the terms involving production

and friction add to the gravitational term, and therefore the altitude of the critical point, i.e. when tube divergence equals this sum, is increased. The magnitude of the friction term depends exponentially on the neutral temperature; raising this decreases the diffusion coefficient and rapidly pushes the critical point outwards.

Making the assumption that the point of zero slope is above the region of production and loss, we have approximately for its locus

$$M = K\left(\frac{3}{S} - \frac{g_o a}{c^2 S^2}\right) \exp \frac{S}{S_n} \qquad (7.7)$$

where K is a constant, and the diffusion coefficient has been assumed to increase exponentially upwards with the scale height of the neutral atmosphere, S_n, which is very small compared with S. Since along this line, in the presence of friction,

$$3/S > g_o a/c^2 S^2,$$

this locus increases upwards as a very strong exponential, rather than the vertical line of the solar wind case. This is evident in Fig.1 of Banks and Holzer (1968).

In the real ionosphere, while at low heights O^+ is the dominant ion, H^+ is formed near 500 km by the resonant charge exchange process

$$H + O^+ \longrightarrow H^+ + O,$$

and helium ions will also be present in significant quantities. The relevant Mach equations are now (7.4) and the simplification made earlier by eliminating the electron pressure term is no longer possible. The computed solutions for hydrogen ions in an oxygen ionosphere are those of Fig. 7.1 for the conditions given, where the most apparent effect of the coupling field is to produce the marked asymmetry about the M = 1 line compared with the single constituent solutions (e.g. Fig.1 in Banks and Holzer, 1968).

The effect of the coupling on S_c may be seen approximately if H^+

is a minority ion. In that case, the distribution of O^+, since it does not readily escape, may be not too different from that of diffusive equilibrium; i.e. if no temperature gradients exist,

$$-\frac{1}{n_e}\frac{\partial n_e}{\partial S} = \frac{a}{H}$$

where H is the scale height of the oxygen plasma. This term will add to the field tube divergence term 3/S. However, since it is known that the hydrogen critical point is reached at $S \sim 1.5$, and H may be 200 - 300 km, $a = 6370$ km, the electric field due to the oxygen, or the electron pressure gradient, dominates over the effect of field divergence. The result is that protons are accelerated upwards by this process, at least until the O^+/H^+ concentration ratio falls. In terms of hydrodynamic flow, the tube divergence is strongly augmented, and the critical point is lowered to an altitude where production, loss and friction are certainly not negligible. This complicates the locus of the line of zero slope equivalent to (7.7), which now becomes quadratic in M.

The effects of temperature gradients may be seen qualitatively:- if these are positive, the gravitational term is augmented, and the critical point raised, or the flow reduced. The reason for this is that an increasing temperature lowers the species pressure gradient, ∇nKT. Such an observation assumes that the other terms are unmodified. In fact, for example, the increased temperatures corresponding to a positive temperature gradient reduce the gravitational term, $(\propto \frac{1}{T})$ and oppose the first effect. The detailed effect of temperature variations is therefore only reliably determined numerically. Such computations have been made (Holzer, 1969), and lead to the general result that protons are swept from the ionosphere, leaving O^+ as the dominant ion to altitudes of several thousand kilometres.

7.3 Experimental Observations of Polar Topside Densities

The changes occurring in the ionosphere across the pole can be investigated in more detail after performing a real height-density analysis of ionograms in the region. This has been done for a number of ionogram sequences during which the satellite traversed some of the polar features described earlier.

Ionograms were reduced to real height profiles by the method of contiguous parabolas (Doupnik and Schmerling, 1965), after which interpolated densities and scale heights were computed at 50 km intervals from 1000 km downwards. High latitude ionograms are frequently of poor quality and caution is needed in interpreting results obtained from them. Commonly, the density at the height of the vehicle is very low and only approximately known, though it may sometimes be found by a plasma resonance technique mentioned in a later chapter. The effect of this uncertainty, and the type of compensation required for the altitude-dependent gyrofrequency is discussed in Appendix II , where it is shown that while the topmost portion of the computed profile is in error, the profile at lower altitudes is reliable. The presence of large gradients of ionisation results frequently in multiple traces, and little weight can be attached to profiles obtained in such regions. This has meant that profiles of the trough have come largely from the morning hours when the feature is widest and the ionograms are felt to be most reliable.

The interpretation of the scale height H, defined by

$$H = -N \frac{dh}{dN}$$

where N is the electron density, assumes that the ray has propagated vertically down into the ionosphere. For high dip angles, if diffusive equilibrium prevails, H is given by

$$\frac{1}{H} = \frac{m_i g}{K(T_i+T_e)} + \frac{1}{T_i+T_e} \frac{d(T_i+T_e)}{dh} \qquad (7.8)$$

where g = acceleration due to gravity at an altitude h

m_i = mean ionic mass at that altitude.

T_i, T_e are absolute temperatures of the ions and electrons

K = Boltzmann's constant.

The second term is small but not zero, as over the altitude considered, the ion temperature is rising from that of the neutral atmosphere to that of the electron gas. Smith and Kaiser (1967) estimate $d(T_i+T_e)/dh$ to be $2-3^{\circ}K/km$ at high latitudes, and so at heights near 700 km, where this gradient is greatest, and T_i+T_e typically 4000°, $K(T_i+T_e)/m_i g \sim 200$ km, the second term contributes about 11% to H. Thus H basically carries information on the ratio T_i+T_e/m_i. In view of the preceeding section, it is unlikely that the highest latitude ionosphere is in diffusive equilibrium, but in the absence of more knowledge on field aligned currents, the scale height at latitudes where the field lines must be closed has been interpreted qualitatively in terms of relative changes in T_i+T_e/m_i.

The results from one pass are shown in summary form in Fig. 7.2. During this sequence at about 0600 LT, the satellite traversed the mid-latitude ionosphere, the morning trough and entered a polar density enhancement. A fairly abrupt change in the form of the reflections was noted at the low latitude boundary of the trough. At higher latitudes and particularly in the polar peaks the traces were thicker and generally more irregular. Significant features appear to be:

1. The density variations at all heights follow those at the F-layer peak, and so the total electron content of the topside ionosphere computed between 450 and 950 km also followed the N_mF_2 variations. This shows that the peaks and troughs are not caused simply by a vertical redistribution of ionisation.
2. The scale height at great altitudes drops steadily from high values at low latitudes to rather low values in the polar region. At the same time, H at 500 km rises sharply from a mid-latitude value of 110 km to almost 200 km inside the

trough. In terms of scale heights, 500 km is now closer to the layer peak, in the vicinity of which the expression used to obtain H breaks down. Nevertheless, extrapolating H(h) curves downwards to 500 km shows that the scale height at this level probably has increased to about 140 - 150 km.

Since the dominant ion at 500 km is O^+ (Bowen et al., 1964), the change in H from mid-latitude to polar ionosphere represents a sudden temperature rise, with the result that the change from O^+ to lighter ions does not occur below 1000 km over the pole. The two profiles at the points marked A and B illustrate this. The former has a pronounced curvature at an altitude of 500 - 600 km, typical of low latitude profiles, and must be caused by a transition to ions lighter than O^+. The slope below 500 km, in the O^+ region, is rather less than that of profile B obtained inside the trough. In the latter example, the slope is approximately unchanged up to the satellite, indicating that the trough consists of a hot, predominantly oxygen plasma.

The remaining profile, C, is taken from the region of the polar peak of ionisation. Above 500 km, there is surprisingly little difference in the shapes of profiles B and C, though the electron content of the latter is a factor of ten greater than that in the trough. The scale heights above 600 km have increased slightly, probably indicating the presence of some lighter ions, but fewer than at mid-latitudes.

Some ionogram sequences extending to the highest latitudes on the nightside of the earth have been examined for evidence of the polar wind. According to Banks (1969), the escape flux of H^+ can be as high as $8 \times 10^8 cm^{-2} sec^{-1}$, which could empty a flux tube in a time of the order 1 - 2 hours. In the steady state, these protons must be replenished by O^+ ions diffusing upwards from near the F-peak and charge exchanging with neutral hydrogen. The flux of oxygen ions required is sufficiently close to the maximum rate set by $O - O^+$ collisions that the O^+ scale height is

depressed towards that of the neutral oxygen atmosphere through which it diffuses, rather than being that of diffusive equilibrium. In the altitude range accessible to Alouette I, this depression is the manifestation of the polar wind most likely to be seen, and such an effect has in fact been observed on passes at very high latitudes. A pass which entered the polar region in the evening and crossed the polar cap depletion on the nightside is analysed in Fig. 7.3. As before, the scale height at 800 km drops at the trough, leaving a predominantly oxygen plasma at higher latitudes. At 500 km, (7.8) for an oxygen plasma becomes

$$T_i + T_e = H\left[16.2 + \frac{d}{dh}(T_i+T_e)\right]$$

where heights are measured in kilometres.

Below 70° magnetic latitude, H_{500} is consistently 150 km, which if a maximum temperature gradient of 3°K/km is assumed, gives $T_i+T_e = 2880°K$. Few direct measurements of particle temperatures at high latitudes have been made. From the results of Brace and Reddy (1965) the electron temperature at 500 km could be about 2000° for these local times and solar epoch. From backscatter observations, (Evans, 1967), the ion temperature at 500 km is not greatly above the neutral gas temperature, which at this time was probably near or below 1000°. Thus, the plasma temperature of just below 3000° predicted by diffusive equilibrium is quite possible. However, at higher latitudes, while still within the polar peak, the scale height at 500 km falls as low as 102 km. Assuming diffusive equilibrium still applies, and $T_i + T_e$ is still 2880°, the temperature gradient must be 12.8°K/km, which is unrealistically high. Alternatively, the probable maximum gradient of 3°K/km in an oxygen plasma implies $T_i + T_e = 1980°K$. While the results of Brace and Reddy (1965) indicate a possible fall in electron temperature at highest latitudes, this would represent a drop of 100% on values deduced a few degrees south and does not seem probable. Thus diffusive equilibrium, which gave reasonable

temperature values at lower latitudes, appears to have failed above an invariant latitude of 80°. The scale height of neutral oxygen at 500 km is 62 km for a temperature of 1000°; the low plasma scale height of 102 km is thus depressed in this direction and could be caused by the upwards diffusion of O^{+} ions predicted. Such evidence for the polar wind is indirect, but the phenomenon has been observed on other passes and seems to be characteristic of latitudes above 80°, where one would not expect field aligned currents, another possible source of scale height depression.

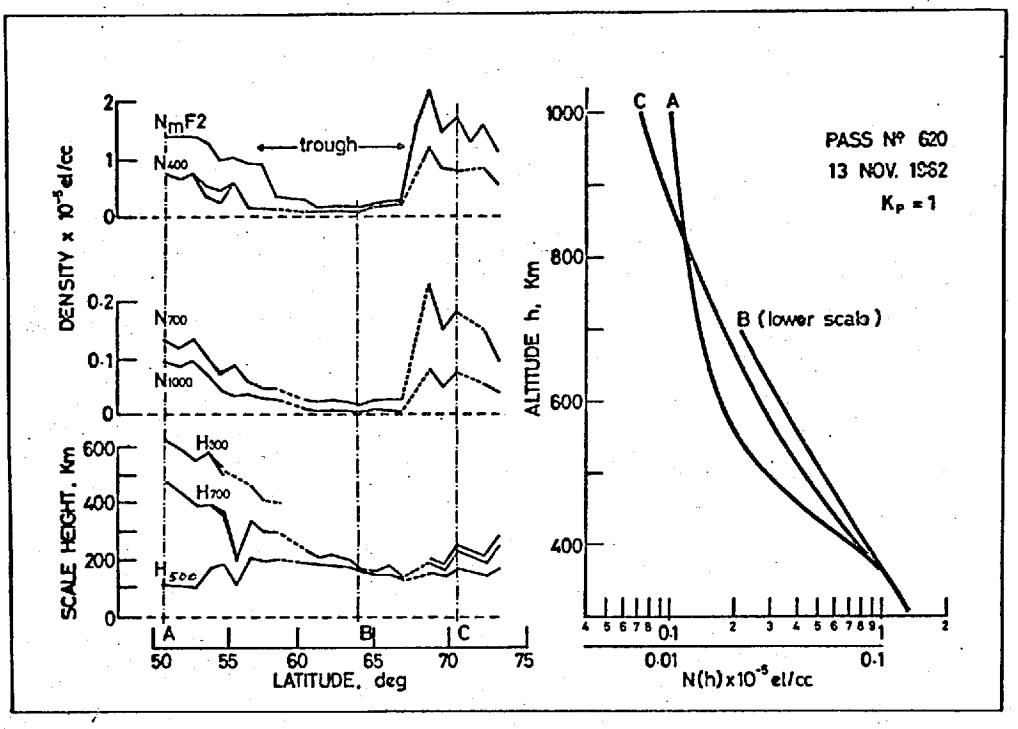


Fig. 7.2 The results of an N(h) analysis of a pass which crossed the morning trough, and entered a polar peak. Where two traces were seen on the ionograms, and neither was clearly oblique, data from both traces is included, giving rise to some double lines on the diagram at the left.

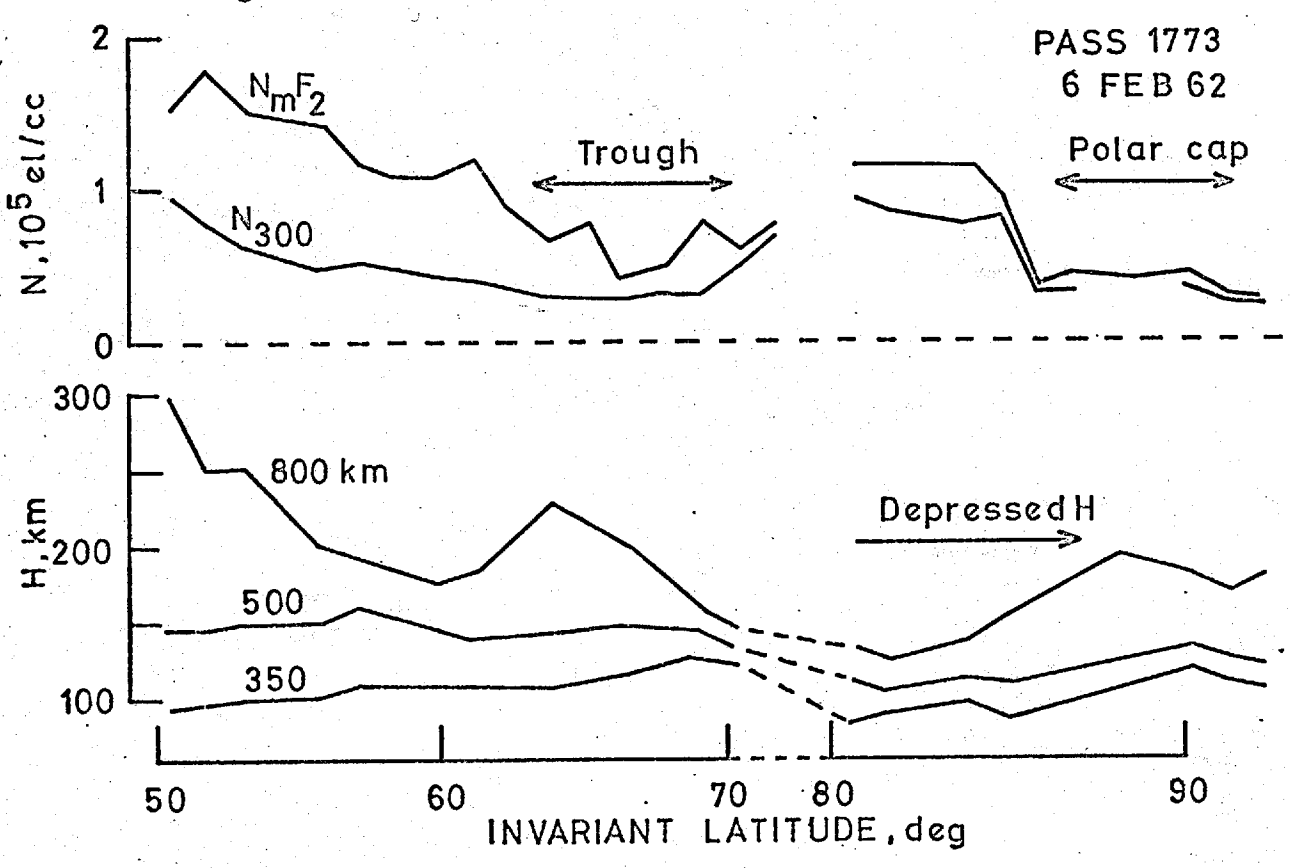


Fig. 7.3 The analysis of a sequence of ionograms where the satellite passed over the magnetic pole on the nightside of the earth. Above magnetic latitudes of about 80°, scale heights are depressed well below those expected if diffusive equilibrium prevailed.

8: Conclusion

The sketch of Fig. 8.1, which is not to scale, outlines what is currently believed to be the overall shape of the earth's magnetoplasma. The strongest, and most predictable, ionosphere - magnetosphere coupling applies within the closed plasmasphere, though the somewhat more erratic effects at higher latitudes map to potentially more interesting regions of the magnetosphere.

The higher temperatures inferred in the polar ionosphere above the plasmapause are consistent with current ideas of magnetospheric circulation, in which the whole region is populated with hot plasma from the tail, which enters the closed field lines from the nightside. The increased temperatures may be produced by conduction downwards from this convecting plasma, or by the joule heating from the current systems related to the circulation, which flow in the ionosphere, as well as the more impulsive heat sources such as electron precipitation in the auroral oval.

The source of the nightside "soft" precipitation, which appears at latitudes coincident with the more impulsive and harder auroral - type precipitation, is probably the plasma sheet and its horn - like extensions. The daytime source, however, is not yet determined. Burch (1968) considered the fluxes may have been associated with the dayside neutral point. The present observations of plasma densities reported in Chapter 6 also suggest the direct entry of solar wind particles, partially thermalised in the bow shock. On reconnection models of the magnetosphere (Dungey, 1961) such an entry along field lines connected to the boundary of the magnetosphere is to be expected.

While a coarse picture of the magnetosphere is now available, many theoretical explanations remain to be made. For example, though an

intimate connection between the ionospheric trough and the plasmapause seems beyond doubt, the present explanations say nothing of the extremely high density gradients reported, at both high and low altitudes. Some ionospheric scale height measurements in the afternoon hours, when the horizontal gradients were large, showed surprisingly little difference in the N(h) profiles at latitudes in and below the trough. The discrepancies found between the trough and plasmapause still lack an adequate explanation if the coupling between ionosphere and magnetosphere is direct, via field lines, and the present information on the plasmapause, trough and magnetic field is not in error.

The halo of electron density found over the pole related to a very quiet solar period and winter conditions, which probably enabled precipitation effects to be located more easily. A question still to be answered concerns whether or not the ring structure is present at all solar epochs. Currently, it seems that the depletion of density at high latitudes related to the absence of ionising particles there, rather than to the removal of plasma by a mechanism such as the polar wind. It is still of interest to learn to what extent the wind can remove ions, and whether or not this is a continuous process. To date, apart from the present finding of depressed scale heights, the only experimental evidence known of the supersonic outflow of protons is an observation of Hoffman (1968) which has been interpreted as a flow of hydrogen, relative to oxygen ions. While undoubtedly the most conclusive evidence of a supersonic wind must come from more refined direct velocity measurements, deductions based on N(h) profiles, particularly from high-orbit satellites, can still be valuable.

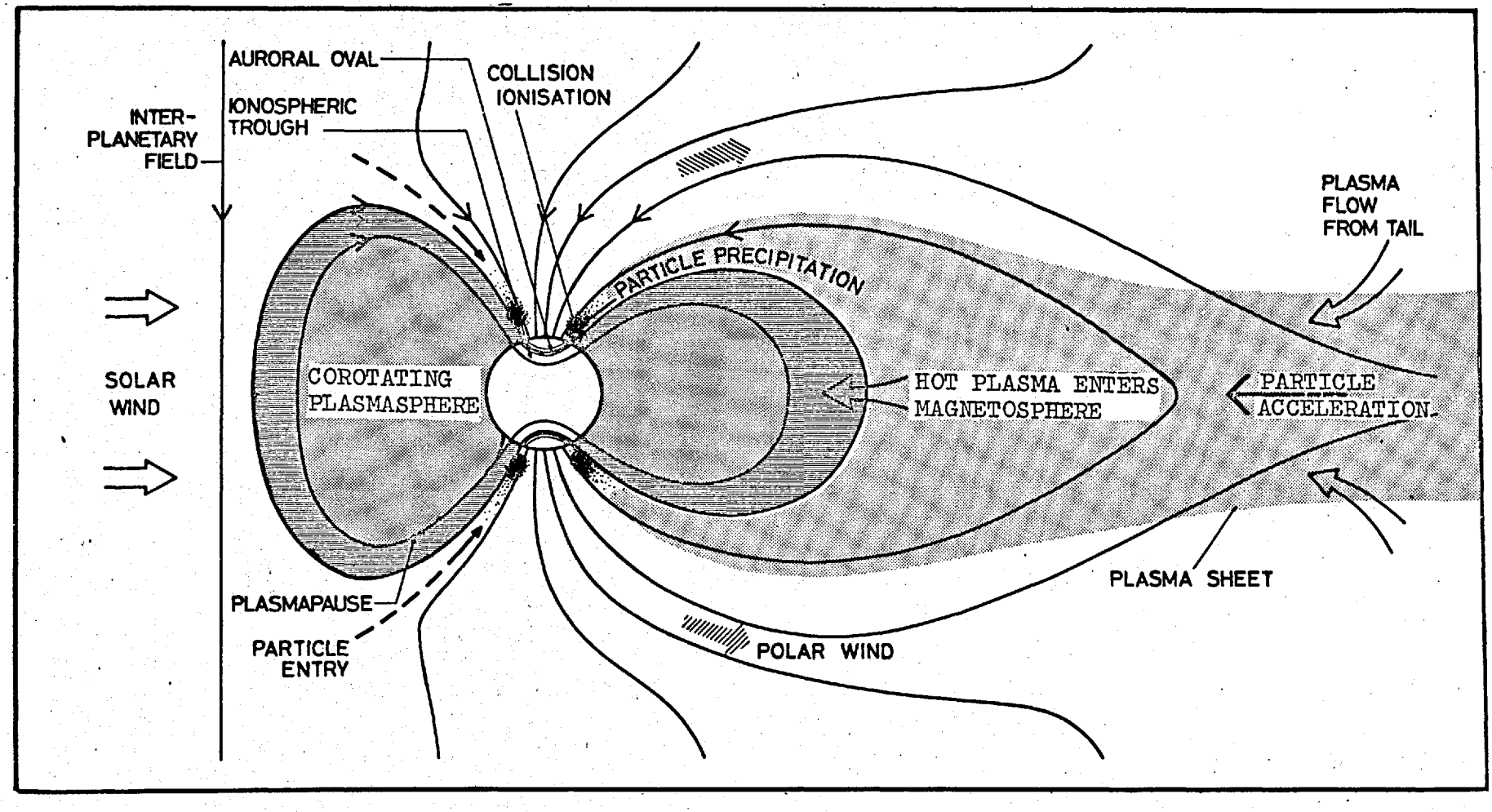


Fig. 8.1 Overall picture of the ionosphere-magnetosphere region about the earth in the noon-midnight meridian. The horizontal shading is a region of closed field lines, linked to the trough in the ionosphere, but which can however take part at some time in magnetospheric circulation, and hence is populated with hot plasma from the tail. At higher latitudes, particles entering the ionosphere, possibly directly on the dayside, produce collision ionisation. Field lines at highest latitudes connect to the tail away from the plasma sheet, where plasma pressures are too low to prevent the polar wind outflow.

PART II

9: Resonance Observations in Space

9.1 Introduction

Although resonance effects in laboratory plasmas have been known to occur for many years, their observation in plasmas in space is fairly recent. The excitation of resonances in the ionosphere was first reported by Knecht et al. (1961), and by Knecht and Russell (1962), during rocket flights designed to test the feasibility of variable-frequency, pulsed-radar experiments from satellites. Subsequently, they have been identified and recorded regularly in experiments involving all the top-side sounders launched to date. The resonances correspond to signals which last for a relatively long time (several milliseconds) being received at a number of characteristic frequencies, following the excitation of the plasma by a radio frequency pulse of very short duration (~100 microseconds). The plasma is said to 'ring' at these characteristic frequencies. The most important of these were identified as the local plasma frequency f_N, f_H and its harmonics, and the upper hybrid frequency

$$f_T = (f_N^2 + f_H^2)^{\frac{1}{2}}$$

It will be seen that these resonances can be attributed to electrostatic oscillations of the plasma, the associated plasma waves having group velocities comparable with the satellite speed. Most attention will subsequently be directed to the resonances at f_T and nf_H, i.e. those involving the magnetic field, as these are more interesting in terms of possible applications.

From the pulse powers given in Table 1.2, it may be deduced that voltages far in excess of the thermal energy of the ionospheric plasma (.1 ev) are imposed on the medium, and while the antenna-ionosphere coupling is not understood, one should expect non-linear effects. These

have been seen recently (Nelms, 1969), but are not discussed here. Gyro-resonances are characterised by a short time persistence compared with the f_N and f_T resonances. In the ionogram of Fig. 1.1, the former persist for about 200 km of virtual depth, corresponding to about 2000 RF periods at the frequencies involved. (100 km of depth is equivalent to a time delay of 667 μs.) In this time, the satellite has travelled some 10 - 20 m along its orbit.

The records from Explorer XX give continuously the virtual depth of reflection at six fixed frequencies. This format shows the resonances to have a fine structure, which is not seen on the standard Alouette display. Both a slow roll modulation of the resonance persistence, due to the changing antenna orientation, and a beat-type interference on the resonance signal itself are commonly seen. Such patterns at the gyro-harmonics are not understood, but may be related to the launching of two waves as outlined in the next chapter. Similar effects are seen at the f_N resonance. McAfee (1969) has proposed an explanation of this resonance by a plasma pressure correction to the ordinary propagation mode at frequencies very close to f_N. This yields a quasi-electrostatic mode, which exhibits rather complicated ray paths within a few hundred metres of the vehicle. From these paths, when the exciting signal is a pulse with component frequencies, a time dependent beat develops at the receiver as the components return with different delays.

9.2 Resonance Identification

The magneto-ionic conditions of all the spike-like responses, both resonance and electro-magnetic in origin, seen on ionograms are summarised in Table 9.1. From the relationships in this table, it is clear that resonance identification is facilitated by the fact that they must occur in a particular sequence; for example, since $f_T^2 = f_N^2 + f_H^2$, both f_N and f_H resonances must occur at frequencies below the upper hybrid resonance.

Magnetoionic condition	Remarks	*Frequency*	
$Y = 1/n, \quad n = 1, 2, \ldots$	Cyclotron harmonics Oscillation $\perp$B	nf_{Hs}	—
$X = 1 + Y$	Z trace zero range echoes	f_{zs}	$f_{zs}^2 = f_{Ns}^2 - f_{Zs} f_{Hs}$
$X = 1$	Ordinary trace zero range echoes	f_{os}	$f_{os}^2 = f_{Ns}^2$
$X = 1$	Plasma resonance Oscillation $\parallel$B	f_{Ns}	
$X = \dfrac{1 - Y^2}{1 - Y^2 \cos^2(\pi/2 - \theta_s)}$	Z trace infinite range echoes	$f_{z\infty}$	—
$X = 1 - Y^2$	Magnetic plasma resonance Oscillation $\perp$B	f_{Ts}	$f_{Ts}^2 = f_{Ns}^2 + f_{Hs}^2$
$X = 1 - Y$	Extraordinary trace zero range	f_{xs}	$f_{xs}^2 = f_{Ns}^2 + f_{xs} f_{Hs}$

Table 9.1 Frequencies and magnetoionic conditions at which spike-like responses may be seen on topside sounder records. The subscript s refers to a quantity measured at the satellite, while $X = f_N^2/f^2$, $Y = f_H/f$.

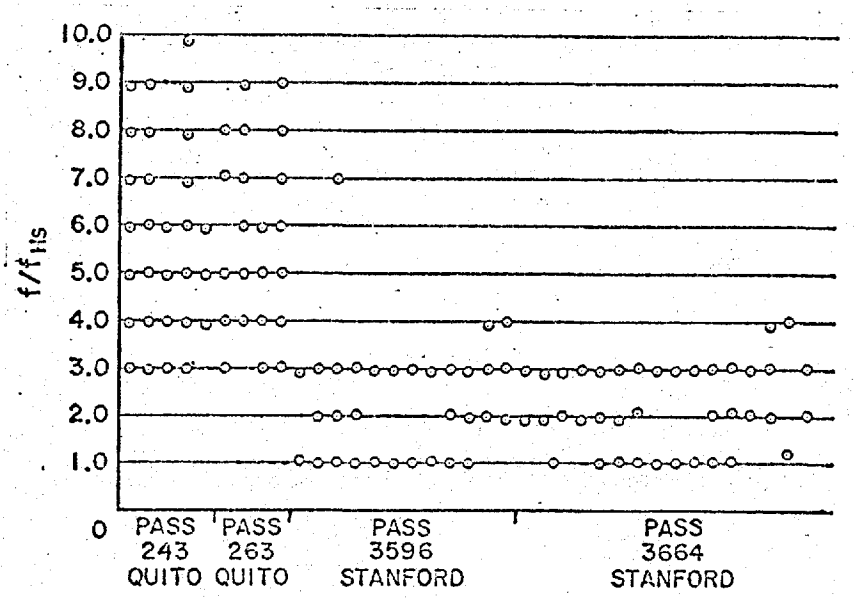


Fig. 9.1 Ratios of the measured gyroresonance frequencies to the calculated gyrofrequency at the satellite for four passes. The ratios are closely integral, indicating that any deviations of the gyroresonances from integral multiples of f_H are small.

In addition, the gyrofrequency is known accurately from field expansions, and the plasma frequency may be found, independently of the resonances, from the ordinary or extraordinary ray zero range traces, as indicated in Table 9.1. Calvert and Goe (1963) identified resonances at nf_{Hs}, f_{Ns} and f_{Ts} using sequences of Alouette I ionograms in which the variation of electron density and geomagnetic field along the orbit was used to distinguish between the different resonances and also to indicate spurious instrumental responses. In another investigation (Thomas and Andrews, 1968) involving all the spike-like responses occurring on the ionograms of four passes, it was confirmed that the resonances seen by Alouette I occurred at the above frequencies, together with some at $2f_T$. The latter are thought to be due to a non-linearity in the receiver. Fig. 9.1 shows the frequency ratio of signals identified as gyroresonances to the computed electron gyrofrequency, for the four passes. It is clear the ratios are closely integral.

Attempts have been made to estimate quantitatively any deviations from such a harmonic relationship by examining portions of seven passes (650 and 663, Ottawa; 243, 257, 236, Quito; 1194, 1234, Prince Albert) which showed clear gyroresonances up to high harmonics.

With high harmonics present it becomes simple to determine the order n of each harmonic. Allowing for the greater accuracy inherent in measurements on the high harmonics, a weighted mean gyrofrequency,

$$\bar{f}_{Hs} = \frac{\sum f_{nHs}}{\sum n}$$

was determined from all gyroresonances seen on a particular ionogram, after which the mean deviation of the gyroresonances from the exact integral multiple of $\bar{f}_{Hs}$ was found. Such deviations were small; in pass 650, for example, the mean deviation from the weighted gyrofrequency was 0.0113 Mc/s, while the 58 gyroresonances seen on pass 1234 had a mean deviation from the weighted gyrofrequency of 0.0105 Mc/s. These devia-

tions of about 1% are well within the experimental limits imposed by the machine-digitising of the ionogram frequencies to three significant figures, by film non-linearities, and by satellite position and hence magnetic field variations between harmonics measured, since the vehicle speed is 7 km/sec and the time between the first and last gyroresonances is typically 5 seconds. At the same time, the plasma density varies by a factor of four over the seven passes, from a high of 2.8×10^4 el/cc on pass 650 to $\sim 0.6 \times 10^4$ el/cc on pass 1234. Thus within the accuracy of the experiment, the gyroresonances do occur at integral multiples of the gyrofrequency, independently of the ambient plasma density. Somewhat better frequency resolution can be realised through the use of the data in its videotape form; using tape formats, or A-scans, Benson (1967) has reported systematic, though small deviations of the resonances from integral multiples of the gyrofrequency. With Alouette I, however, the basic limitation of frequency determination is imposed by the radar-type sounding transmitter. This limit is about ± 6.5 Kc/s since the 1 Mc/s^2 linear sweep rate and 67 pps repetition frequency yield frequency increments of 13 Kc/s pulse centre to pulse centre. Resonances at intermediate frequencies would, of course, be excited because of the almost continuous frequency spectrum of the transmitted pulse; the frequency components are spaced approximately every 67 c/s, with a bandwidth of the order of $\pm$ 10 Kc/s about the centre frequency. In his work, Benson measured the centre of the resonance by an interpolation technique involving the time for which ringing was seen on the A-scans following the transmitted pulse. By this method, the error was thought to be reduced to around $\pm$ 4 Kc/s, but it seems that the important question of whether the gyroresonances bear an exact harmonic relationship to each other is difficult to decide unambiguously from the Alouette data.

9.3 Other Effects

In addition to the signals received at the characteristic frequencies enumerated in Table 9.1, a number of additional effects are seen on topside ionograms, particularly from Alouette II and the newly launched ISIS-I. These include a remote resonance (Hagg, 1966; Muldrew, 1966; Muldrew and Hagg, 1966) which links the extraordinary ray and the gyrofrequency at a point away from the vehicle; an infrequently occurring resonance, diffuse in appearance (Nelms and Lockwood, 1966); and a spur on an electron resonance, which is connected to the proton gyrofrequency (King and Preece, 1967). Resonances were a by-product of the Alouette I programme, and complicated effects such as these are probably best investigated with later-generation sounders, such as ISIS-I, designed with resonance investigation in mind.

10: Electrostatic Waves in an Infinite Plasma

10.1 Introduction

The existence of resonances at frequencies equal to f_N and f_T suggests that electrostatic oscillations of the electrons in the plasma, in directions parallel and perpendicular to the static magnetic field might be involved as suggested by Calvert and Goe (1963). In this process, the electrons may be envisaged oscillating against a restoring force caused by the charge separation of the ions and electrons. This type of cold plasma mechanism, however, is unable to predict effects at frequencies equal to multiples of the gyro-frequency. These effects depend on thermal motions. Though in the theory, infinitely small oscillations are considered, thermal motion causes the particles to gyrate with finite cyclotron radii. Under certain conditions, a bunching of the gyrating electrons is caused by the alternating electric field, which, in turn, is sustained by the bunched gyrations (Lockwood, 1963, Johnson and Nuttall, 1964). In a real plasma, the many different particle velocities lead to wave-particle interactions, some of them resonant, which can only be satisfactorily taken into account via a distribution function. The technique was first introduced by Landau (1946), who showed that the simple electrostatic oscillation at the plasma frequency would, in the absence of a magnetic field, be changed into slowly propagating damped waves. The analysis was developed (e.g. Gross, 1951, Bernstein, 1958) as outlined in section 10.3 to include the effects of a static magnetic field.

10.2 The Plasma Permittivity

In an analysis of plasma behaviour, two approaches are possible. The plasma may be treated as a region of space with permittivity ε_o, together with an assembly of free charges and currents, or it may be

Table 10.1

Quantities used in Part II and their meaning unless specified otherwise.

$\underline{E}$	Electric field
$\underline{B}$	Magnetic field
$\underline{D}$	Electric displacement
$\underline{r}$	position vector
$\underline{v}$	particle velocity
m	particle mass
t	time
e	electronic charge (positive)
K	Boltzmann's constant
T	Absolute temperature
N	Electron density
v_T	thermal speed of a particle, $\sqrt{\frac{KT}{m}}$
v_g	group velocity
v_p	phase velocity
c	speed of light in vacuo
ω_c	electron gyrofrequency, $\frac{eB}{m}$
f_H	$\omega_c/2\pi$
f, f_o	wave frequency
ω, ω_o	$2\pi f_o$
$\underline{k}$	wave vector
λ	wavelength, $2\pi/k$
f_T	upper hybrid frequency
ω_T	$2\pi f_T$

treated as a dielectric medium with a tensor permittivity $\underline{\underline{\varepsilon}}$. Where sources are involved, external charges (e.g. on an antenna in the plasma) and the currents due to them must be considered. If ρ_{int} and $\underline{j}_{int}$ are the normal plasma charge and current, ρ_{ext} the external (source) charge, $\underline{j}_{ext}$ the plasma current due to the sources, Maxwell's equations become

$$\nabla \wedge \underline{H} = \underline{j}_{ext} + \underline{j}_{int} + \varepsilon_o \dot{\underline{E}} = \underline{j}_{ext} + \underline{\underline{\varepsilon}}\dot{\underline{E}} \qquad (10.1)$$

$$\nabla \wedge \underline{E} = -\dot{\underline{B}} \qquad (10.2)$$

$$\nabla . \underline{B} = 0 \qquad (10.3)$$

$$\nabla . \varepsilon_o \underline{E} = \rho_{int} + \rho_{ext} \quad \text{or} \quad \nabla . \underline{\underline{\varepsilon}}\underline{E} = \rho_{ext} \qquad (10.4)$$

Transform methods enable these equations and the Boltzmann equation to be handled algebraically. A quantity $A(\underline{r},t)$ may be Laplace transformed in time and further Fourier transformed in space according to the convention

$$\bar{A}(\underline{k},\omega) = \int_{-\infty}^{+\infty} d\underline{r} \int_{0}^{\infty} dt\, A(\underline{r},t) e^{-i(\omega t - \underline{k}.\underline{r})} \qquad (10.5)$$

The reverse transform is

$$A(\underline{r},t) = \left(\frac{1}{2\pi}\right)^4 \int_{-\infty}^{+\infty} d\underline{k} \int_{C} d\omega \bar{A}(\underline{k},\omega) e^{i(\omega t - \underline{k}.\underline{r})} \qquad (10.6)$$

Equation (10.5) implies that ω has a negative imaginary part so that the integrand is bounded, which requires the inverse transform (10.6) to be taken along a contour below the real ω-axis. These transforms are equivalent to the normal mode analysis (after initial conditions are neglected), in which all quantities are assumed to vary as

$$\exp i(\omega t - \underline{k}.\underline{r})$$

Maxwell's equations are then transformed in the usual way by writing

$$\nabla = -i\underline{k}$$

$$\frac{\partial}{\partial t} = i\omega$$

and may be combined to give the wave equation, with sources, applicable for times after initial transients have disappeared, i.e.

$$\underline{k}\wedge\underline{k}\wedge\underline{E} + \omega^2\mu_o\underline{\underline{\varepsilon}}.\underline{E} = i\omega\mu_o\underline{j}_{ext}. \tag{10.7}$$

Here, the transformed permittivity ε is defined by the equation

$$\underline{D}(k,\omega) = \underline{\underline{\varepsilon}}(k,\omega).\underline{E}(k,\omega)$$

and where now all variables represent the doubly transformed quantities. From the continuity equation for external charges and currents

$$\omega\rho_{ext} = \underline{k}.\underline{j}_{ext}$$

We seek electrostatic solutions, or waves whose electric field is related to a potential i.e.

$$\underline{E} = -\nabla\phi = i\underline{k}\,\phi \tag{10.8}$$

This implies $\nabla\wedge\underline{E} = 0$, (i.e. $\underline{k}\|\underline{E}$), and by (10.2), $\underline{B}$ is zero also; that is to say, when the wave vector $\underline{k}$ is parallel to the wave electric field, the wave is purely electrostatic (E.S.), and there is no associated magnetic field. In this case, the wave equation reduces to

$$\omega\underline{\underline{\varepsilon}}.\underline{E} = i\underline{j}_{ext} \tag{10.9a}$$

which might have been deduced via Poissons electrostatic equation.

From (10.9a) and the continuity equation, since $\underline{k}\|\underline{E}$, we have

$$\underline{k}.\underline{\underline{\varepsilon}}.\underline{k}\,E/k = \frac{i\underline{k}.\underline{j}_{ext}}{\omega} = i\rho_{ext} \tag{10.9b}$$

The dispersion equation for electrostatic waves is obtained from this expression by examining theconditions for non-zero values of E to

exist in the absence of ρ_{ext}, the driving term; i.e. $\underline{k}.\underline{\underline{\varepsilon}}.\underline{k} = 0$. Without loss of generality, consider a Cartesian system, with E_z parallel to the applied magnetic field $\underline{B}_o$, and the remaining axes such that E_y (and hence k_y) is zero. This leads to the E.S. dispersion relation

$$k_x^2 \varepsilon_{xx} + 2k_x k_z \varepsilon_{xz} + k_z^2 \varepsilon_{zz} = 0$$

where the expected equality of ε_{xz} and ε_{zx} (Stix, 1962) has been used. For propagation perpendicular to $\underline{B}_o$, $k_z = 0$, and the dispersion relation becomes simply, writing $\varepsilon_\perp = \varepsilon_{xx}$

$$k_x^2 \varepsilon_\perp = 0 \qquad (10.10)$$

The evaluation of the dispersion equation in this case then gives an expression for $\varepsilon_\perp$, which is required in the analysis of later driven problems. In these problems, which involve perpendicular propagation, (10.9b) gives the associated perpendicular (to $\underline{B}_o$) electric field

$$\underline{E} = \frac{i\underline{k}\rho_{ext}}{k^2 \varepsilon_\perp} \qquad (10.11)$$

These perpendicular modes are highly significant as they do not suffer Landau damping (Bernstein, 1958). Clearly, the quantity $\varepsilon_\perp$ is highly significant, as it determines the normal modes via the dispersion equation, and the electric fields (and hence admittances) in driven problems.

The electrostatic assumption, i.e. $\underline{E} \| \underline{k}$ or very nearly so, restricts somewhat the possible range of k. On separating the electric field into components parallel and perpendicular $\underline{k}$, the wave equation (10.7) may be written (Stix, 1962)

$$(\varepsilon_o n^2 - \underline{\underline{\varepsilon}}.)\underline{E}_\perp = \underline{\underline{\varepsilon}}.\underline{E}_\parallel$$

in which n is the refractive index $\frac{ck}{\omega}$ of the medium. Since we require

$E_\perp \to 0$, we require n^2 large, i.e.

$$\frac{ck}{\omega} >> 1,$$

or the phase velocity $\omega/k << c$, the velocity of light. This implies that k must not be too short, and the waves are slow.

10.3 Electron Oscillations in a Warm Plasma

The phenomenon of cyclotron waves, or Bernstein wave propagation is characteristic of warm plasmas, in which wave-particle interactions are taken into consideration by the use of the function $f(\underline{r},\underline{v},t)$ which describes the particle distribution in the plasma. The fields, currents and the distribution function are linked through Boltzmann's equation, which states that the changes in f along a trajectory in phase space are caused only by collisions. In many applications, such as space plasmas, collisions are unimportant enough that one may apply Liouville's equation, which requires that particles are conserved along a trajectory in phase space. Thus for the electron gas alone (since at the frequencies of interest, the ions will be effectively at rest),

$$\frac{\partial f}{\partial t} + \underline{v} \cdot \frac{\partial f}{\partial \underline{r}} - \frac{e}{m}(\underline{E} + \underline{v} \wedge \underline{B}) \cdot \frac{\partial f}{\partial \underline{v}} = 0 \qquad (10.13)$$

A linearised, normal mode analysis is used to solve this equation; we assume any quantity may be expressed as the sum of its unperturbed value, subscripted zero, and a perturbation, which varies as $\exp i(\omega t - \underline{k}.\underline{r})$. Thus we have

$$f = f_0 + f_1$$

$$\underline{B} = \underline{B}_0 + \underline{B}_1$$

but $$\underline{E} = \underline{E}_1$$

since we assume there is no applied electric field.

Inserting these terms in (10.13), and retaining only first order quantities yields the linearised equation

$$if_1(\omega - \underline{k}\cdot\underline{v}) - \frac{e}{m}(\underline{E}_1\cdot\frac{\partial f_o}{\partial \underline{v}} + \underline{v}\wedge\underline{B}_o\cdot\frac{\partial f_1}{\partial \underline{v}}) = 0 \quad (10.14)$$

The term $\underline{v}\wedge\underline{B}_1\cdot\frac{\partial f_o}{\partial \underline{v}}$ is omitted in this expression; in the case of pure E.S. propagation, it is zero since $\underline{B}_1 = 0$. In general, $\frac{\underline{v}\wedge\underline{B}_1}{E_1}$ is of order $\frac{v_p v_T}{c^2}$, where v_p is the phase velocity, and v_T the thermal speed of the particles, so that the term is small for quasi-electrostatic propagation, characterised by low phase speeds.

Following the treatment of Bernstein (1958), to solve (10.14) we introduce a rectangular co-ordinate system in velocity space, with unit vectors $\hat{i}$, $\hat{j}$, $\hat{k}$, in which $\hat{k}$ is parallel to $\underline{B}_o$, and the wave vector $\underline{k}$ is in the $\hat{i}-\hat{k}$ plane making an angle θ with the $\hat{k}$ axis (Fig. 10.1). Thus

$$\underline{k} = \hat{i}\,k\sin\theta + \hat{k}k\cos\theta$$

In terms of the notation in Fig. 10.1, the particle velocity $\underline{v}(u,w,\phi)$ may be resolved into components $\underline{u}$ in direction $\hat{k}$, and $\underline{w}$, the perpendicular velocity, in the $\hat{i}-\hat{j}$ plane with an azimuthal angle ϕ. Thus,

$$\underline{v} = \underline{w} + \underline{u} = \hat{i}w\cos\phi + \hat{j}w\sin\phi + \hat{k}u$$

In terms of these cylindrical co-ordinates,

$$\frac{\partial f_1}{\partial \underline{v}} = \nabla_{\underline{v}} f_1 = \hat{w}\frac{\partial f}{\partial w} + \hat{u}\frac{\partial f}{\partial u} + \hat{\phi}\frac{1}{w}\frac{\partial f}{\partial \phi},$$

where $\hat{w}$ represents a unit vector in the direction $\underline{w}$ etc., and hence

$$\underline{v}\wedge\underline{B}_o\cdot\frac{\partial f_1}{\partial \underline{v}} = -B_o\frac{\partial f_1}{\partial \phi}.$$

Equation (10.14) becomes

$$\frac{\partial f_1}{\partial \phi} + \frac{i(\omega - \underline{k}.\underline{v})}{\omega_c} f_1 = \frac{e}{m\omega_c}\underline{E}_1\cdot\frac{\partial f_1}{\partial \underline{v}} \quad (10.15)$$

This equation may be solved explicitly, subject to the requirement that

f_1 is periodic in Φ, with period 2π, by the use of an integrating factor G, where

$$G = \exp - \int_{\phi'}^{\phi} \frac{i(\omega - \underline{k}.\underline{v})}{\omega_c} \, d\phi \quad .$$

The required solution of (10.15) is then

$$\underline{f}_1 = \frac{1}{\omega_c} \int_{-\infty}^{\phi} d\phi' \; G \frac{e}{m} \underline{E}_1 . \frac{f_o(\underline{v}')}{\partial \underline{v}'} \qquad (10.16)$$

where $\underline{v}'$ is a vector defined by

$$\underline{v}' = \hat{i} w \cos \phi' + \hat{j} w \sin \phi' + \hat{k} u .$$

Equation (10.16) explicitly links perturbations in the distribution function and the corresponding electric field variations. The electric field may also be found from the distribution function and Maxwell's equations. Here, the full Maxwell equations may be used, yielding all possible waves, or the induced field $\underline{B}_1$ may be omitted as in electrostatics giving longitudinal waves with $\underline{k} \| \underline{E}$. Adopting the latter course, the current equation gives

$$\nabla \wedge \underline{H} = 0 = \underline{\underline{\varepsilon}} . \dot{\underline{E}}_1 = \underline{j}_{int} + \varepsilon_o \dot{\underline{E}}_1$$

$$\text{i.e.} \qquad \underline{\underline{\varepsilon}} . \underline{E}_1 = \varepsilon_o \underline{E}_1 + \frac{\underline{j}_{int}}{i\omega}$$

Also, $\underline{j}_{int} = -e \int d^3v f_1 \underline{v}$ where d^3v implies an integration over velocity space. Using the expression for f_1 derived in (10.16), and putting $\underline{E}_1 = \frac{\underline{k} E_1}{k}$, we derive the dispersion relation (cf 10.10).

$$\underline{k}.\underline{\underline{\varepsilon}}.\underline{k} = \varepsilon_o k^2 - \frac{e^2}{i\omega m \omega_c} \int d^3v \int_{-\infty}^{\phi} d\phi' \underline{k}.\underline{v} G \underline{k}.\frac{\partial f_o}{\partial \underline{v}'} = 0$$

(10.17)

An equivalent expression could have been derived using the equations of charge rather than of current. For a Maxwellian plasma

$$f_o = N \left(\frac{m}{2\pi KT}\right)^{\frac{3}{2}} \exp - \frac{mv^2}{2KT}$$

and the dispersion equation may be integrated progressively (e.g. Bernstein, 1958) to yield finally,

$$1 + k^2a^2 = \frac{s}{\omega_c} \int_o^\infty dy \exp \left\{ -\frac{sy}{\omega_c} - \lambda (1 - \cos y) - \tfrac{1}{2}\mu y^2 \right\} \quad (10.18)$$

where

a = Debye length = $\left(\frac{\varepsilon_o KT}{Ne^2}\right)^{\frac{1}{2}}$

s = $i\omega$ = Laplace transformed frequency

λ = $k^2r^2 \sin^2\theta$

μ = $k^2r^2 \cos^2\theta$

r = gyroradius of a thermal electron = $\frac{1}{\omega_c}\sqrt{\frac{KT}{m}}$

θ = angle between $\underline{k}$ and the field $\underline{B}_o$

y = $\phi' - \phi$

This integral is defined for all s if $\mu > 0$, or if s has a small real component. The electron oscillations parallel to the applied magnetic field are given by (10.18) with $\lambda = 0$, while the cyclotron modes emerge when the propagation is at right angles to $\underline{B}_o$, i.e. $\mu = 0$. For this propagation mode, Bernstein (1958) showed that the damping caused by wave-particle interactions is zero, that is, ω is wholly real. As the direction of propagation is varied from the perpendicular, Landau damping increases extremely rapidly, and is rather wave-length dependent. From expressions for the Landau damping of waves in the presence of a magnetic field (Yngvesson and Perkins, 1968) the magnitude of the damping for propagation angles between 0° and 90° to the magnetic field may be much greater than in the no-field case. Near 90°, the damping depends strongly on whether ω is near a multiple of the gyrofrequency.

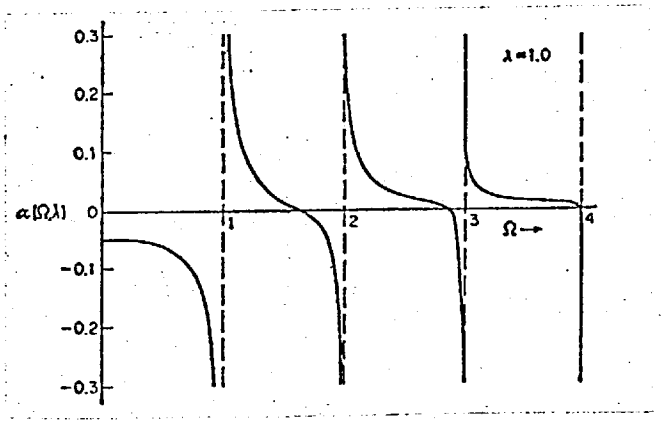


Fig. 10.2 A plot of the Bessel function series $\alpha(\Omega,\lambda)$ in equation 10.19 for the case $\lambda = 1.0$ (From Bernstein, 1958).

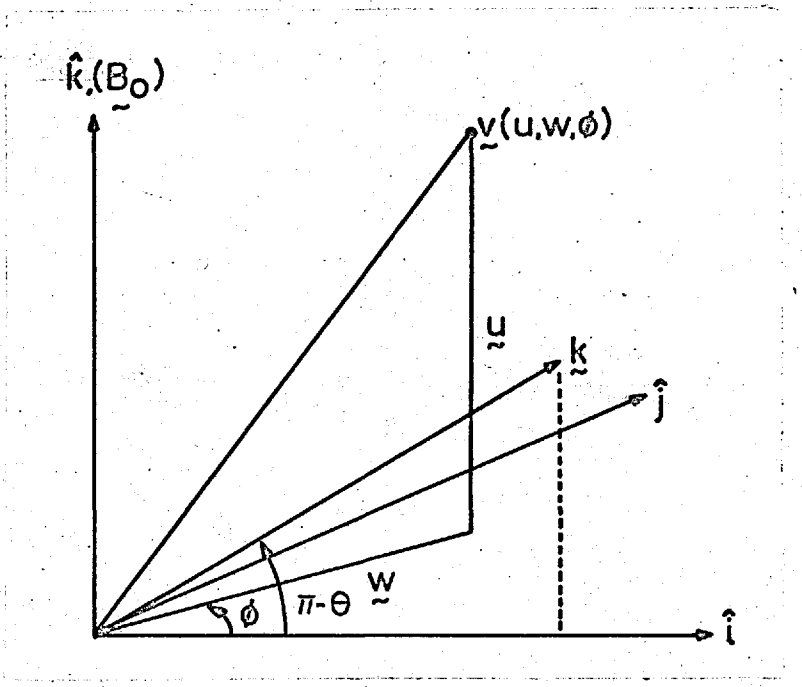


Fig. 10.1. The co-ordinate system and nomenclature used to transform Liouville's equation to cylindrical co-ordinates.

10.4 Perpendicular Propagation

For the case of waves propagating at right angles to the applied magnetic field, Bernstein (1958) has shown that s is wholly imaginary. Several representations of the dispersion relation are possible.

(i) Series Method:- Using the relation

$$e^{\lambda}\cos y = \sum_{n=-\infty}^{+\infty} I_n(\lambda)e^{-iny}$$

where I_n is Bessel function of the first kind, of imaginary argument, (10.18) with $\mu = 0$ may be integrated to yield

$$k^2a^2 = e^{-\lambda}I_o(\lambda) + 2\sum_{1}^{\infty} e^{-\lambda}I_n(\lambda)\frac{\Omega^2}{\Omega^2-n^2} - 1 \qquad (10.19)$$

where Ω has been written for ω/ω_c.

As noted earlier, the perpendicular warm plasma permittivity $\varepsilon_\perp$ may be derived from this dispersion relation. Comparing (10.10), (10.17) and (10.19) it may be deduced that

$$\varepsilon_\perp/\varepsilon_o = 1 + \frac{1}{k^2a^2}\left[1 - e^{-\lambda}I_o(\lambda) - 2\sum_{1}^{\infty} I_n(\lambda)\frac{\Omega^2}{\Omega^2-n^2}\right] \qquad (10.20)$$

The series dispersion equation (10.19) is useful in predicting the kind of solutions (i.e. ω, k pairs) to be expected. The function on the right has been discussed by Bernstein (1958), who produced the graph of it shown in Fig. 10.2. Clearly, poles will be produced each time Ω approaches an integer, regardless of the smallness of the smoothly decaying multiplier $e^{-\lambda}I_n(\lambda)$. Thus the solutions of the dispersion equation (10.19) will be given by the intersection of the horizontal line of ordinate k^2a^2 with the Bessel series. For a value of k^2a^2 then, particularly if this is large, it is clear that there will be an infinite number of solutions of Ω, all close to, but slightly greater than integers. This fact may be used in numerical computations.

(ii) Integral Representation:- Alternatively the solution of equation (10.18) with $\mu = 0$ may be computed by an integral technique. If it is

assumed that s has a small real part, i.e.

$$s = i\omega + \delta \tag{10.21}$$

equation (10.18) may be written (Gross, 1951),

$$1 + k^2a^2 = \frac{\frac{s}{\omega_c}\int_0^{2\pi} \exp\left\{-\frac{sy}{\omega_c} - \lambda(1-\cos y)\right\}}{1 - \exp\left(\frac{-2\pi s}{\omega_c}\right)} \tag{10.22}$$

The assumption in (10.21) is necessary to ensure the convergence of an infinite series to the form of the denominator in equation (10.22). Collecting real and imaginary parts of this equation yields two integral representations of the perpendicular dispersion relation (and by implication $\varepsilon_\perp$). In the limit of vanishingly small δ, we obtain

$$2(1 + k^2a^2)\sin^2\pi\Omega = \Omega\int_0^{2\pi} \sin\Omega y \exp -\lambda(1 - \cos y)dy \text{ (Real)} \tag{10.23}$$

$$\text{and} \quad (1 + k^2a^2)\sin 2\pi\Omega = \Omega\int_0^{2\pi} \cos\Omega y \exp -\lambda(1 - \cos y)dy \text{ (Imaginary)} \tag{10.24}$$

10.5 Numerical Solutions

The dispersion equation has been solved numerically for the undamped case of propagation perpendicular to the magnetic field. Solutions were computed by a Newton-Raphson technique, using both integral and series representations of the dispersion equation, parametric first in ω_p^2/ω_c^2, then in ω_p^2/ω^2, via the plasma density term k^2a^2 in the equation. Two examples are presented in Fig. 10.3, in which the normalised variables ω/ω_c (or f/f_H) and kr are used, rather than ω and k. Since the dispersion equation involves only $(kr)^2$, k may be negative, though only the positive branch is shown.

The relevance of either the first or second presentation depends on the experimental situation; in the experiment to be described, ω_p^2/ω^2 is constant, since ω/ω_c is changed by varying the gyrofrequency. On the other hand, in an experiment such as Alouette, it is the operating fre-

quency which is varied, whilst ω_p^2/ω_c^2 is fixed.

Below the upper hybrid frequency ω_T, there is a continuous spectrum of waves; that is, for any real value of ω there is a corresponding real wave number k. Above ω_T, gaps are present in the spectrum of waves, and propagation is possible only in a band on the high frequency side of the gyrofrequency harmonics. Where ω_p^2/ω_c^2 is constant, the curves flatten progressively as the harmonic number n increases, causing the upper limit of the propagation window to lie closer to an integral multiple of the gyrofrequency. This is not so for constant ω_p^2/ω^2. Here the difference between the "hump" frequency and the harmonic below stays almost constant. Numerical values of the solutions are included in an appendix.

The limitations on the range of kr computed are set by the electrostatic assumptions. In terms of the variables kr and Ω, (10.12) leads to

$$\Omega/kr < c/v_T,$$

where v_T is the electron thermal speed. Since $c/v_T \sim 1000$, the computed solutions become invalid above the light line $\Omega = 1000$ kr; that is, the curves do not continue to approach the ω-axis with zero slope in the wedge-shaped zone where E-M effects must be considered. At the other end of the scale, there is nothing in the theory to preclude infinitely short wavelengths. On physical grounds, however, one would not expect wavelengths less than the Debye length, for the waves would not see collective particle effects, and the wave fields would be influenced by individual particle trajectories. Hence we set

$$\frac{2\pi}{k} > a \qquad \text{i.e.} \qquad kr < 2\pi \frac{\omega_p}{\omega_c}$$

and in the worst computed case, where $\omega_p/\omega_c = 1$, kr is restricted to values below about 5.

10.6 Physical Origin of the Sounder Resonances

It is now possible to understand physically how the resonances might

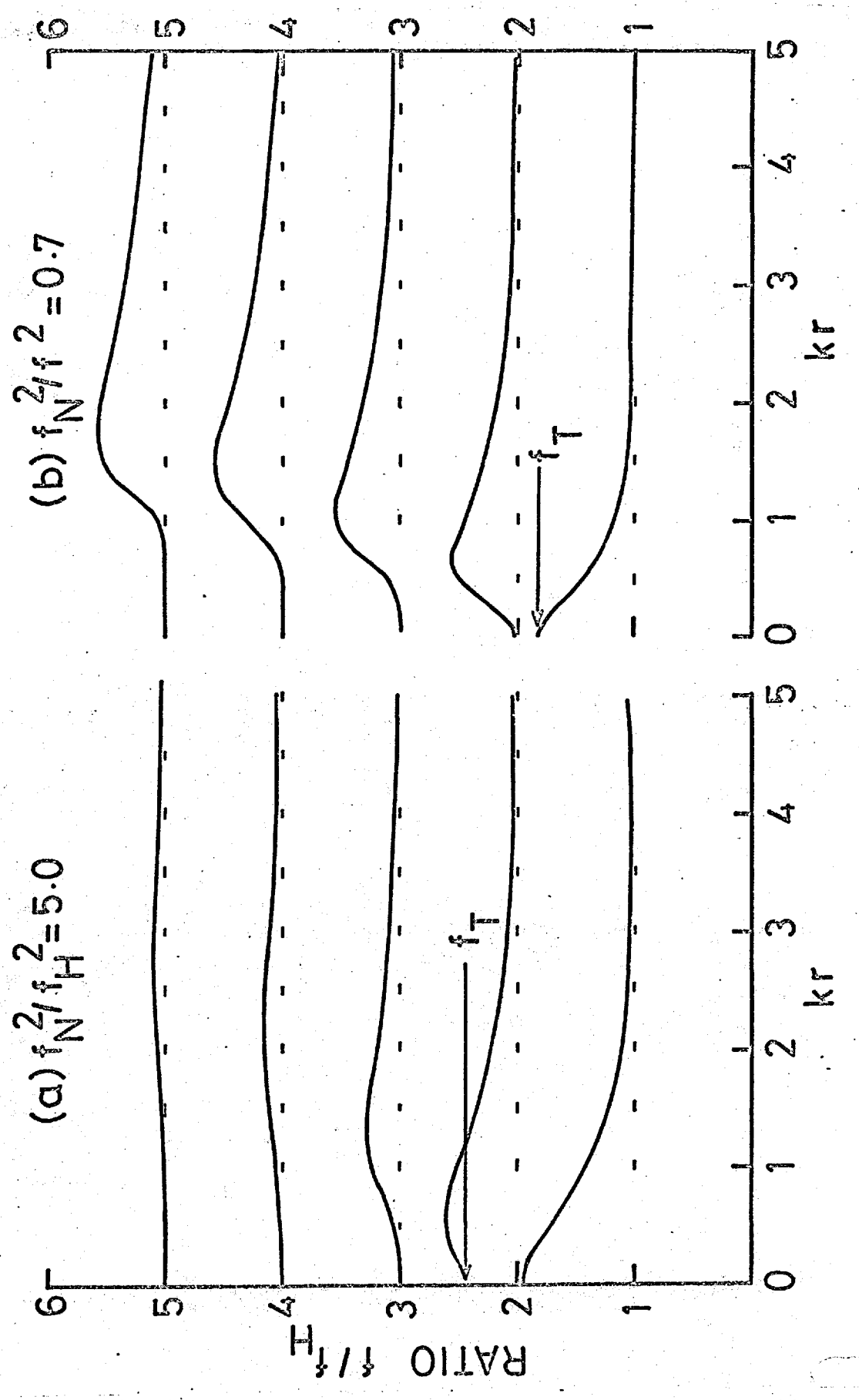


Fig. 10.3 Dispersion curves for cyclotron waves propagating at right angles to B_o, (a) for f_N^2/f_H^2 constant, and (b) for constant f_N^2/f^2. The curves in (a) flatten at high harmonics; those in (b) do not. In each case, propagation above f_T is possible only in bands adjacent to the gyroharmonics.

arise by reference to the dispersion curves. Since the resonance signals on ionograms are caused by the reception of energy for sometimes of the order of milliseconds, it is thought that this must be due to the satellite's velocity matching the group velocity of an excited electrostatic wave packet, and hence extracting energy from it for a considerable period of time. Fejer and Calvert (1964) have shown that the rate at which a wave packet spreads into the surrounding medium depends on the ratio of phase to group velocity. In a wave packet with differing propagation vectors $\underline{k}$, the smallest size of the packet will be determined approximately by the width of the spatial spectrum of Fourier components. If the wave number is k at the center of the spectrum, the spatial width will be about $2\pi/k$. In an isotropic medium, since the direction of the group velocity is that of $\underline{k}$, the packet will spread in all directions. An index of the time T required for substantial spreading to occur may be taken as the time required for the wave packet to just displace itself - i.e. the spatial size divided by the group velocity v_g. That is,

$$T = \frac{2\pi}{kv_g}$$

In terms of wave periods $2\pi/\omega$, this will occur after τ periods, where

$$\tau = \frac{v_p}{v_g} .$$

This is true in an isotropic medium, such as a plasma without a magnetic field, in which case Fejer and Calvert showed that the decay of oscillations for conditions found in the exosphere would be caused almost entirely by the spreading of the wave packet, the decay due to Landau damping being small at the wavelengths concerned. The result is modified if a magnetic field is present, as the group velocity in general is not in the direction of $\underline{k}$. However, for the special cases of propagation parallel and perpendicular to the magnetic field, Fejer and Calvert showed that the group velocity is in the direction of $\underline{k}$. Thus in these cases,

the time for which oscillations remain localised is given by the ratio of phase to group velocity as in the no field case. Since the group velocity is low, the persistence at these limiting angles is high. The arguments advanced concerning the relative unimportance of Landau damping of course are strengthened for $\underline{k} \perp \underline{B}_o$.

In view of the large damping of the electrostatic waves at other than perpendicular propagation, it would seem then that to observe resonances for an extended period requires that the satellite velocity normal to the field should match the group velocity of the undamped waves travelling in that direction; further, to ensure the energy does not become rapidly dispersed, the group velocity should be much less than the phase velocity.

The group velocity of the electrostatic waves ($= d\omega/d\underline{k}$, or the gradient of ω in $\underline{k}$ space) can be derived by differentiating the dispersion curves of Fig. 10.3a. In terms of the normalised variables of that figure, the slopes give the required group velocity normalised to the average thermal velocity of an electron. An example illustrating the group velocities for gyroharmonics above the second and the plasma parameter $\omega_p^2/\omega_c^2 = 1$ is given in Fig. 10.4. Here, speeds are normalised to the thermal velocity, but the true speeds for a plasma temperature of 1000^oK corresponding to the topside ionosphere are also indicated. From the dispersion curves, it is apparent that for a given frequency ω within the transmission band, there are two electrostatic waves with differing wave numbers. Corresponding to these waves, the slope of the dispersion curves or the group velocity, has two values, one positive and one negative, indicating that the group and phase velocities are oppositely directed. In the diagram of group velocities, (Fig. 10.4), speeds arising from negative slopes are plotted to the left and vice versa, to illustrate the continuity of the group velocity as the wave number changes. In the figure, $\underline{k}$ decreases as one moves clockwise around the various loops

from the "six o'clock" position. It is here also, i.e. large and small $\underline{k}$, that the electrostatic assumptions made become invalid. The general flattening of the dispersion curves described earlier here manifests itself as a progressive decrease in the maximum group speed reached as the harmonic number of the transmission band increases.

From this diagram of group velocities, there are apparently several frequencies, all above integral multiples of the gyrofrequency, at which the component of satellite velocity normal to the magnetic field matches the group velocity, and it may be significant that Benson (1967) noted several resonance spikes which appeared as doublets.

From laboratory experiments and the argument presented earlier, it is unlikely that the matched frequencies corresponding to $k \longrightarrow \infty$ would be seen. This leaves, however, two sets of resonant frequencies; one quite near to integral multiples of the gyrofrequency, and the others well displaced corresponding to the "hump" on the dispersion curves. In many cases, particularly with high order harmonics, the deviation of the first set from nf_H would be too small to be measured from the Alouette I data. This is not the case with the frequency deviations of the second set, which may be large. The maximum possible deviation from an integral multiple of the gyrofrequency, corresponding to zero group velocity, expressed as a percentage for various values of plasma parameter and harmonic number is shown in Fig. 10.5, and corresponds to the approximate analytic expression, based on a similar treatment of the Bernstein modes, given by Dougherty and Monaghan (1965). These resonances were never detected on the Alouette I records, but have recently been reported in the data from Alouette II (Warren and Hagg, 1968). The existence of these resonances is strong evidence for the validity of the theory.

Rather approximate expressions for the strength and duration of the resonances have been given in the literature, and have been reviewed elsewhere (Thomas and Andrews, 1968).

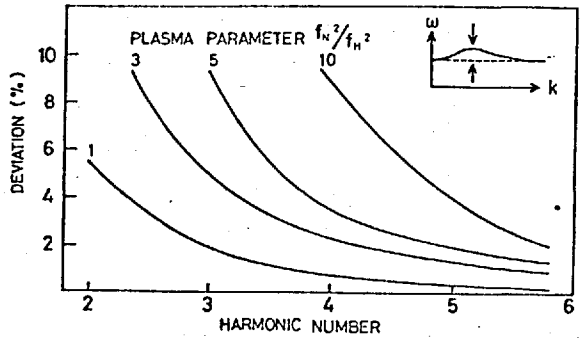


Fig. 10.5 Maximum possible percentage frequency deviation from an integral multiple of the gyrofrequency (occurring at the part of the dispersion curve shown in the inset), predicted for gyroresonances by Bernstein theory. Deviations for values of plasma parameter spanning conditions in the ionosphere are shown. These maximum deviations were not seen on Alouette I records, but have since been reported.

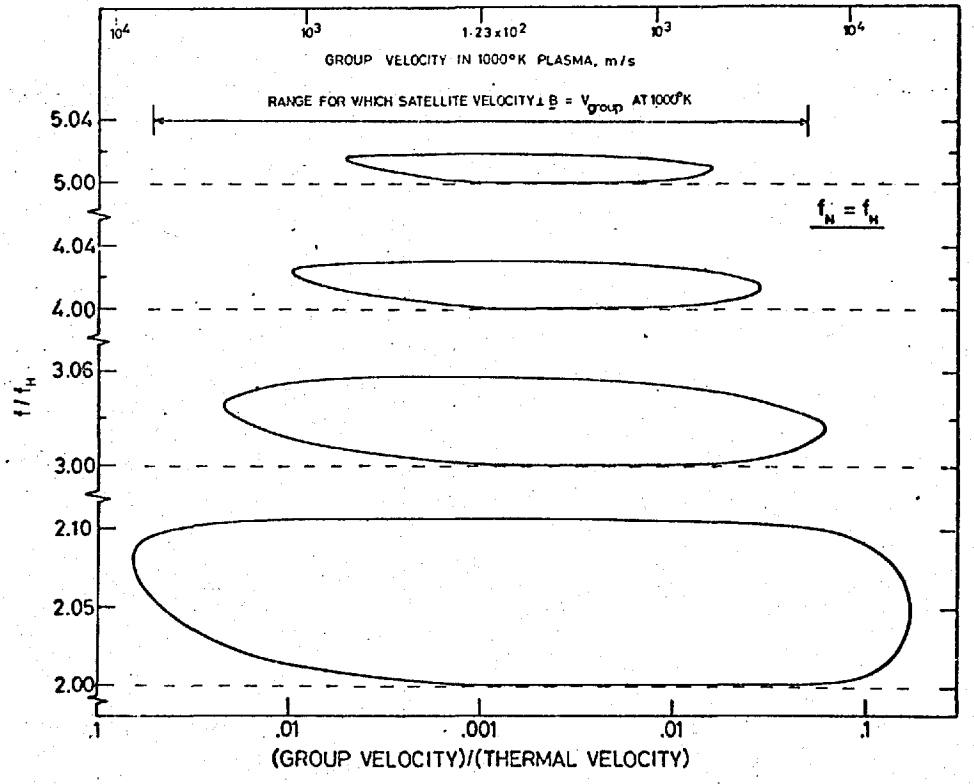


Fig. 10.4 The group velocities of Bernstein waves of frequencies above f_T in a Maxwellian plasma for which $f_H = f_N$. At a given frequency, $d\omega/dk$ has two values, one positive and one negative. To show the continuity of the curves, velocities arising from negative slopes are drawn to the left, positive to the right, and all are normalised to the electron thermal speed, v_T. The range over which the Alouette I velocity normal to the field may match the group speed, for $T_e = 1000^{\circ}K$, is indicated.

11: Laboratory Experiments: Background

11.1 Introduction

The interpretation of the Alouette resonance signals has been based on a theory of warm plasmas which was shown to predict waves near the gyroharmonics, via the dispersion relation $\varepsilon_1 = 0$. As a check on this, the existence of these waves can be better verified by experiments in the relatively controlled environment of the laboratory.

There is a considerable literature of experimental observations of effects at frequencies related to the gyrofrequency, and as comprehensive reviews have been given by Crawford (1965, 1968), only an outline is given here.

Observations of noise emissions at right angles to $\underline{B}_o$, at multiples of f_H, were reported by Wharton (1960), and by Landauer(1961), in experiments involving streaming electrons. Landauer(1962, 1964) subsequently detected emissions up to the 45th harmonic, in all cases of an intensity far greater than expected from thermal radiation. Because of the presence of the streaming electrons in the experiments, it was supposed that much of the cyclotron radiation came from beam-plasma interactions. This was confirmed (Bekefi and Hooper, 1964) in an experiment in which different amounts of the streaming energy could be injected transverse to $\underline{B}_o$, so varying the number of particles able to couple to transverse waves. Working with hot cathode discharges, and fewer streaming electrons than the first experiments, Tanaka et al. (1963) showed that maximum noise emission could occur displaced from nf_H. Both absorption and transmission measurements show structure, which was interpreted by Buchsbaum and Hasegawa (1966) as the trapping of discrete cyclotron wave modes in the interior of the inhomogeneous plasma. This is possible in a column discharge, because continuous wave propagation can exist only below the

upper hybrid frequency (Fig. 10.3). In a plasma column with a radial density profile, ω_T decreases outwards until a point is reached at which a wave of a particular frequency cannot propagate.

A major advance on the early observations was made by Crawford et al. (1964), and by Harp (1965), when discrete modes of propagation were excited by probes placed inside the plasma column, in regions of fairly uniform density. This means that the treatment of chapter 10, which applies strictly only for uniform plasmas, may be used. Since the present investigation began, some experiments in similar discharges have been reported by Crawford et al. (1967), and most recently by Clinckemaille (1968). From (10.11), the electric field near a source, such as an antenna in the plasma, is closely linked with $\varepsilon_\perp$. This implies that the admittance between two probes also depends on $\varepsilon_\perp$, so that the dispersion equation may be deduced from measurements of this quantity.

The experimental work reported here consists of part of a programme designed ultimately to test the feasibility of a cyclotron wave diagnostic technique in space. This thesis concerns the development of a suitable discharge tube, and some experiments from which the E.S. dispersion relation was measured, and some diagnostic measurements made.

11.2 Theoretical Aspects of the experiments

The linear theory commonly used is incapable of describing the plasma behaviour in the sheath region very near to the antennas. It is here that charge fluctuations on the probes are coupled to the plasma via perturbations to the trajectories of particles which pass through the region (Pavkovitch and Kino, 1963). Due to the uncertainty of these boundary conditions, it is expected that the theory will hold good only for distances greater than a few Debye lengths from the antennas.

To make the problem physically meaningful , a collision term is incorporated in the Boltzmann equation by writing, with the present sign

conventions

$$\left.\frac{\partial f}{\partial t}\right|_{\text{collisions}} = -\nu f_1$$

where ν is the electron-neutral collision frequency (appropriate in the case of lightly ionised plasma). If this term is transposed, the Boltzmann equation becomes formally equivalent to the collisionless Liouville equation (10.13), if ω is replaced by $\omega - i\nu$.

To investigate the electric field in the plasma, consider an infinite plane grid at $x=0$, in the $y-z$ plane, parallel to $\underline{B}_o$, through which electrons pass without being collected (i.e. it is a source of charge, but does not otherwise interact with the plasma), and on which is placed a driving charge oscillating at a frequency ω_o;

$$\text{i.e.} \qquad \rho_{ext} = e^{i\omega_o t}\delta(x)$$

with its double transform

$$\rho_{ext}(k,\omega) = \frac{1}{i(\omega-\omega_o)}$$

From (10.11) and (10.6), the temporal electric field perpendicular to the grid is

$$\underline{E}(k,t) = \underline{k}\,\frac{1}{2\pi k^2}\int_C \frac{e^{i\omega t}d\omega}{\varepsilon_\perp(\omega-i\nu,k)\,(\omega-\omega_o)}$$

Since for real k, the roots ω of $\varepsilon_\perp(\omega,k)=0$ are real, the zeros of $\varepsilon_\perp(\omega-i\nu,k)$ now lie at $\omega+i\nu$. Thus the electric field arising from a real wave number is

$$\underline{E}(k,t) = i\underline{k}\,\frac{e^{i\omega_o t}}{k^2\varepsilon_\perp(\omega_o-i\nu,k)} + T \qquad (11.1)$$

where T is a series of terms arising from the zeros of $\varepsilon_\perp$, all of which involve a time dependence $e^{-\nu t}$. For large t then, for any degree of

damping, the system responds only to the driving frequency and one may validly assume all time dependences of the form $\exp i\omega_o t$. The spatial electric field is then given by

$$E(x,t) = \frac{e^{i\omega_o t}}{(2\pi)} \int_{-\infty}^{+\infty} \frac{ike^{-ikx}dk}{k^2 \varepsilon_\perp(\omega_o - i\nu, k)} \qquad (11.2)$$

In the absence of collisions, it has been shown (Bernstein, 1958) that the poles of the integrand for real ω_o fall at real values of k; i.e. along the integration path (though there are complex poles also). With the small component $-i\nu$ now associated with ω_o, the value of k required to reduce $\varepsilon_\perp$ to zero becomes complex by an amount found by Taylor expanding $\varepsilon_\perp(\omega_o - i\nu, k)$ about ω_o, k_o, where $\varepsilon_\perp(\omega_o, k_o) = 0$. It is found that the root (ω_o, k_o) moves to $(\omega_o - i\nu, k_o - \frac{i\nu}{v_g})$, and the poles no longer fall on the integration path.

For $x>0$, (11.2) is effected by closing the integration contour in the lower-half k plane. The contour and the shifted poles near the real k axis are illustrated in Fig. 11.1. The significance of this discussion is that it shows that for positive directions, only the poles A and B which arise from positive group velocity portions of the dispersion curve, i.e. outward propagating energy, contribute to the field. Though one cyclotron mode may have a negative phase velocity, the energy is always carried away from the radiator as physically it must.

Buckley (1968) has expanded (11.2) for vanishingly small ν as a sum of residuals corresponding to the poles of the integrand. The result is of the form

$$E(x,t) = -e^{i\omega_o t}\left[\frac{1}{2\varepsilon_\perp(\omega_o)}\bigg|_{k=o} + \frac{e^{+ik_1 x}}{-k_1 \frac{\partial \varepsilon_\perp}{\partial k}\big|_{-k_1}} + \frac{e^{-ik_2 x}}{k_2 \frac{\partial \varepsilon_\perp}{\partial k}\big|_{k_2}} + 2\mathrm{Re}\sum_{n=3}^{\infty} \frac{e^{-ik_n x}}{k_n \frac{\partial \varepsilon_\perp}{\partial k}\big|_{k_n}}\right] \qquad (11.3)$$

The final summation expresses the spatially damped contribution from any complex zeros of $\varepsilon_\perp$, which arise, for example, when ω_o lies outside a propagating cyclotron band. Roots $\pm k$ of $\varepsilon_\perp$ then appear in complex conjugate pairs. This summation rapidly decays as x increases. Terms in k_1 and k_2 represent undamped, propagating Bernstein modes. In the stop-band zones, both are omitted, whilst only k_1 is included at frequencies below ω_T. The denominator of the first term, which arises from the pole at $k = 0$, may be found from (10.20) to be

$$\varepsilon_\perp\Big|_{k=o} = \varepsilon_o\left(1 - \frac{\omega_p^2/\omega_c^2}{\omega_o^2/\omega_c^2 - 1}\right) \qquad (11.4)$$

and is just ε_c, the cold plasma perpendicular permittivity. Thus term 1 represents the capacitively transmitted field, with an infinite wave length in the E.S. approximation. The kind of electric field excited as a function of x, resulting from the interference of the components may be seen from (11.3). For simplicity, consider $\omega_o < \omega_T$, so that $k_2 = 0$, and x is assumed large enough that damped contributions are negligible. Then E is of the form

$$E(x,t) = E_o e^{i\omega_o t}\ (a + \cos k_1 x + i \sin k_1 x)$$

Expressing this in an amplitude - phase form, the phase is given by

$$\phi(x) = \tan^{-1}\left\{+\frac{\sin k_1 x}{a+\cos k_1 x}\right\}$$

and the amplitude A by

$$A^2(x) = (1 + a^2 + 2a \cos k_1 x)E_o^2 \qquad (11.5)$$

Experimentally, we detect the power in the wave, proportional to A^2. As a detecting probe moves away from the radiator, we expect to find amplitude maxima separated by a distance δx, where

$$\delta x = \frac{2\pi}{k_1} = \lambda$$

i.e. the maxima are separated by one cyclotron wavelength, rather than $\lambda/2$, as is the usual standing wave case. Finding this wavelength for a given ω_o by moving a detecting probe enables the dispersion relation to be found. The extension of this approach to a frequency at which two waves may propagate shows the amplitude to be again x-dependent, but now contains a beat frequency, $\cos(k_1 - k_2)x$, as well as the components $\cos k_1 x$ and $\cos k_2 x$.

The impedance between two grids may be found from the series expansion of (11.3), which has the advantage of exhibiting the contributing components. The current supplied to the plasma is found from the time derivative of ρ_{ext}, and the driving voltage from integrating an expression similar to (11.3) between grids. The result for $\omega_o < \omega_T$ given by Buckley (1968) in terms of the vacuum capacitance C_o/unit area is

$$\omega_o C_o R = \frac{2}{d}\left\{\frac{1 - \cos k_1 d}{k_1^2 \cdot \frac{\partial \varepsilon}{\partial k}\Big|_{k_1}}\right\} \qquad (11.6)$$

$$\omega_o C_o X = -\frac{\varepsilon_o}{\varepsilon_c} - \frac{2}{d}\left[\frac{\sin k_1 d}{k_1^2 \frac{\partial \varepsilon}{\partial k}\Big|_{k_1}} + \begin{pmatrix}\text{terms from complex}\\ \text{zeros of } \varepsilon\end{pmatrix}\right]$$

where the impedance $Z = R + iX$ per unit area, and the grid spacing is d.

Qualitative results may be seen from (11.6)

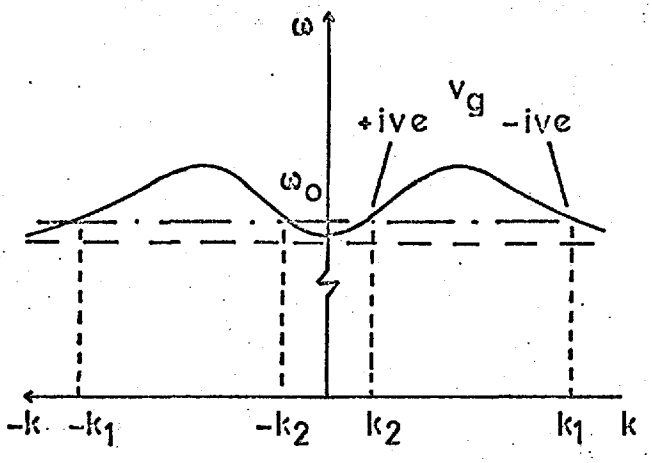
1) The real part of the admittance is provided solely by the propagating Bernstein wave.

2) As d increases, $R \longrightarrow 0$, and $iX \longrightarrow \frac{1}{i\omega C}$, where C is the cold plasma capacitance.

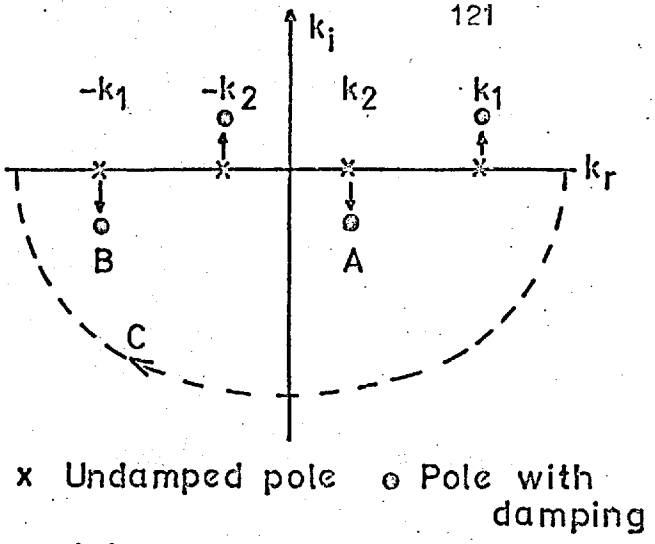
From the second result we expect the admittance between the grids will be proportional to $|\varepsilon_c|$, with warm plasma effects superimposed near

the propagation bands of the waves. The signal in a transmission experiment will then be related to $|\varepsilon_c|$. This quantity, from (11.4), is sketched against ω_c/ω_o (as measured in experiments) in Fig. 11.2.

The theoretical form of the admittance between two infinite, cyclindrical parallel wires was computed by Mantei (1967), and is qualitatively very similar to the infinite grid case. Mantei's results are redrawn in Fig. 11.3 to show the relation of the admittance to the propagation bands. Admittance maxima above the gyroharmonics (above ω_T) and below ω_T are caused by a minimum voltage across the plasma, due to the presence of an even number of cyclotron half wavelengths between antennas. Between admittance peaks then, ω_c/ω_o has changed to allow one more (or less) cyclotron wavelength to be accomodated.



(a) Dispersion curve branch



(b) Complex k plane

Fig 11.1 Evaluation of the integral in (11.2). $\varepsilon_\perp(\omega_o,k)$ is zero at $\pm k_1$, $\pm k_2$, on the dispersion curve, i.e. these points become integration poles (crosses) in (b). When collisions are included, the poles move to the positions indicated, and only those at A and B, corresponding to positive group velocities, contribute in the integration.

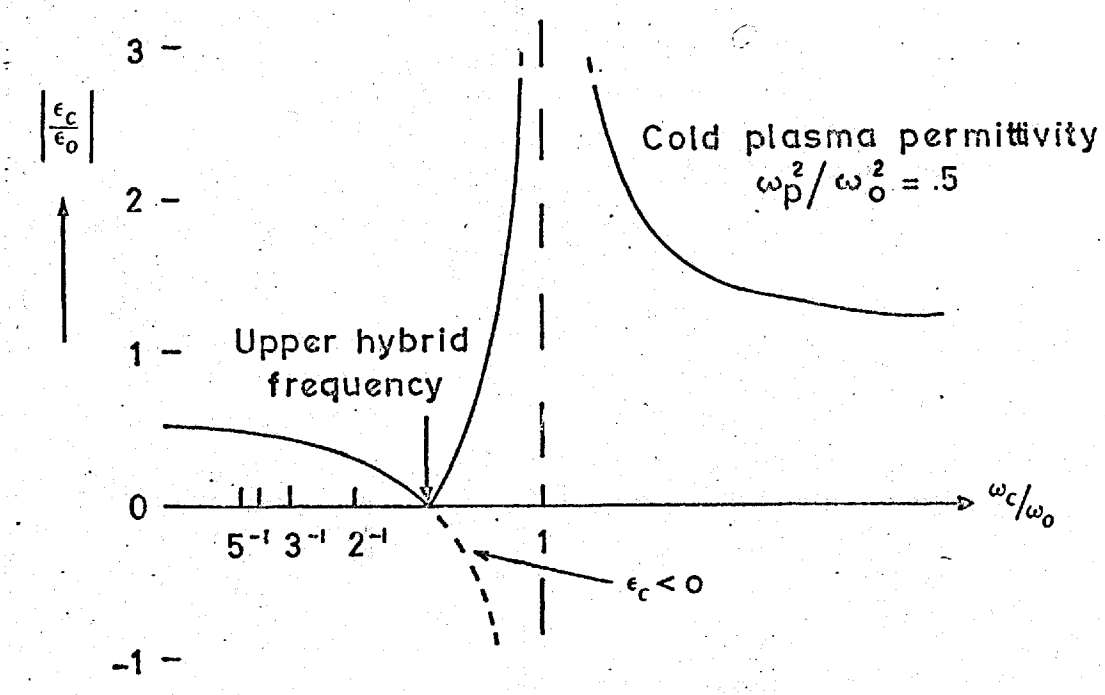


Fig. 11.2 The modulus of the cold plasma permittivity as ω_c/ω_o is increased. The curve also gives the overall shape of the perpendicular admittance expected between two antennas in a magnetoplasma.

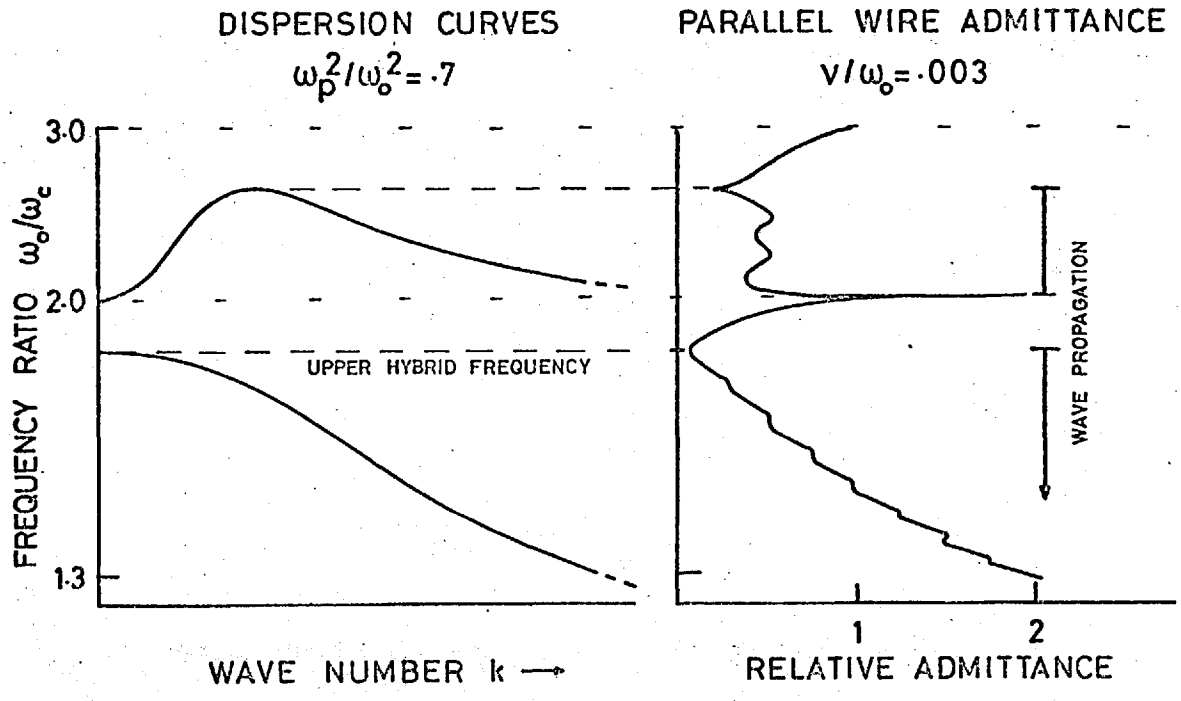


Fig. 11.3 (Right) The computed admittance per unit length between two parallel conducting cylinders immersed, parallel to $\underset{\sim}{B}_o$, in a plasma with a low electron-neutral collision frequency, for a typical experimental geometry (from Mantei, 1967). The sketch on the left shows the relationship between the admittance, particularly the upper hybrid null and the oscillations in the regions of propagating cyclotron waves, and the dispersion curve.

12: Laboratory Experiments: Observations

12.1 Equipment

Experiments have been carried out in the discharge tube shown in Fig. 12.1, which consists of a cathode "gun" separated from the discharge chamber by a mesh anode. The chamber is 65 cm long, 10 cm in diameter; the plasma size corresponds to the cathode diameter, which for these experiments was 5 cm. A thermionic cathode is necessary at the operating pressure (10^{-3} - 10^{-4} torr, Argon), and both tungsten wire and barium oxide coated nickel discs have been used, the latter producing a more uniform plasma, but requiring some 200 watts of heating. While the neutral pressure is low enough to require hot cathodes to sustain the discharge, the significant collision frequency (between electrons and neutrals, since the degree of ionisation is low) is estimated to be about 1 Mc/s, which agrees approximately with an experimental estimate under similar conditions (Freeston, 1968). The ratio of collision to operating frequency is therefore of order .001, or an order of magnitude above that found in the ionosphere at 1000 km (Thomas and Andrews, 1968).

The antenna probes may be changed, and both are movable by a thread of 1 mm pitch. One probe may be extracted at a speed of about 2 mm/sec by means of an electric motor. The magnetic field was calibrated by a Hall probe gaussmeter. Near the probes, it is constant to 1% over $\pm$ 4 cm along the tube axis, and substantially independent of radial position. By means of the coil power supply, the electron gyrofrequency may be held fixed or swept mechanically from zero to 700 Mc/s.

Since plasma densities depend primarily on the tube current, the discharge is operated by a current-regulated supply, which applies a potential of up to 50 volts between cathode and anode for currents up to .5 Amp. Some 50 volt electrons pass through the earthed anode mesh, which

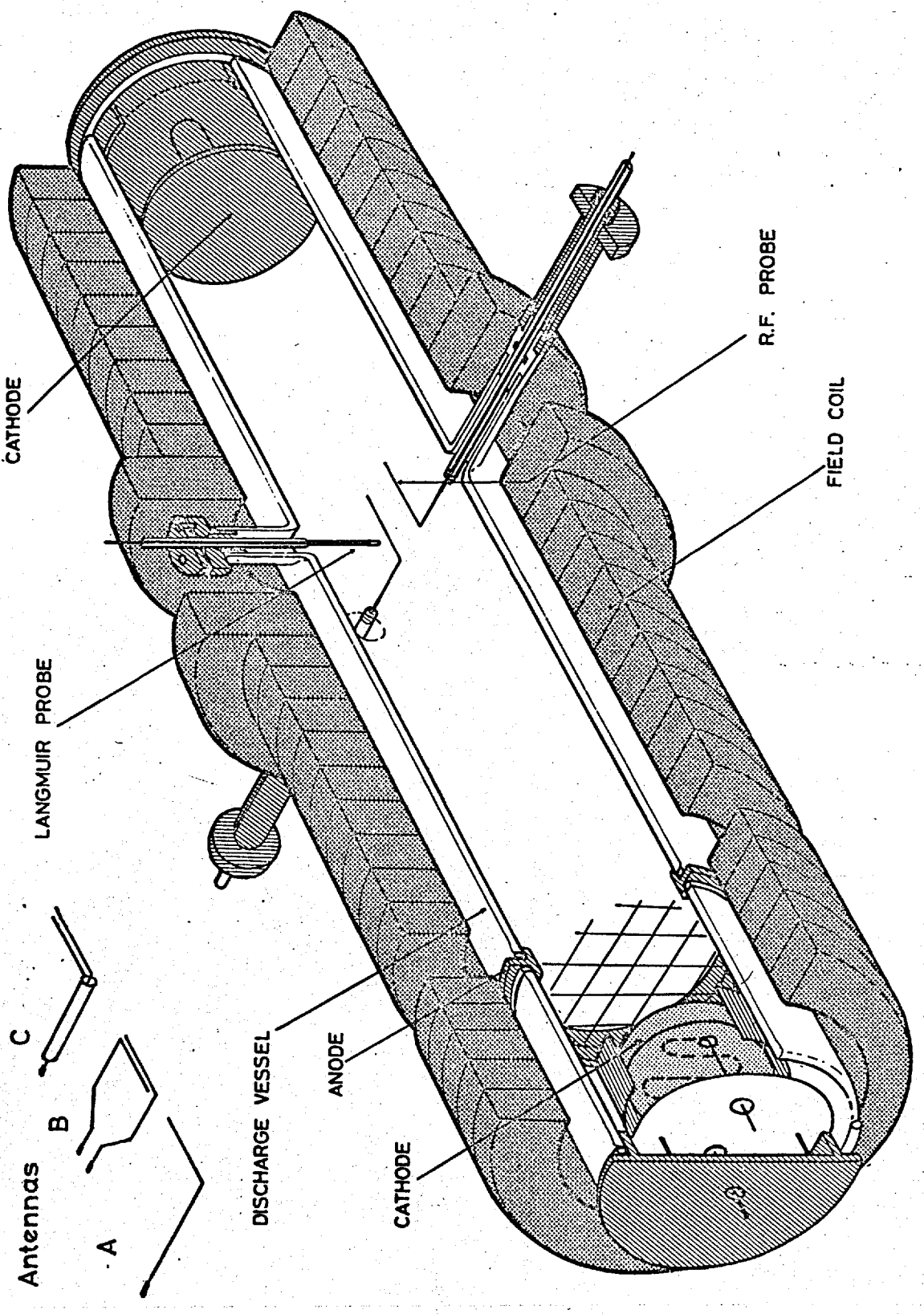


Fig. 12.1 Cut-away drawing of the discharge tube, fitted with an indirectly heated oxide cathode. Antenna types, shown in the inset, are interchangeable. The operating gas is fed in through a port below the probes, and the system is continuously pumped through holes in the plate at the far end of the tube.

has been found to isolate the discharge chamber from any fluctuations near the cathode, and produce a stable plasma by collisions in the chamber. The range of electron densities available, found by the null in transmission at f_T (see Fig. 11.2) and by approximate Langmuir probe measurements, is from 10^9 - 10^{10} el/cc, or plasma frequencies of 300 - 1000Mc/s. As the neutral density at 10^{-4} torr is $\sim 5 \times 10^{12}$/cc, the percentage ionisation is indeed low.

Langmuir probe measurements indicate electron temperatures of 10 ev at the lowest pressures, falling to 3 ev as the neutral pressure is raised, but it is thought that these estimates are incorrect. An electron-neutral collision frequency of 1 Mc/s means a 50 volt electron can travel almost the tube length before making a collision, and so one should expect a large suprathermal component in the tail of the electron velocity distribution. As it is this portion of the distribution which is sampled when estimating temperatures, it seems probable that the probe measurements will be contaminated by streaming electrons. The marked fall in T_e with increasing neutral pressure (and hence decreasing mean free path) supports this interpretation.

An amplitude-modulated signal of about .1 volt amplitude, and between 450 and 1000 Mc/s is transmitted through the plasma, and received by a heterodyne detector. After filtering, the modulating signal is rectified, and displayed on a chart recorder. As the output of the signal generator is not constant, it is more convenient in swept measurements to vary the magnetic field, whilst leaving the wave frequency fixed. In this way also, the problem of tracking the transmitted frequency with the receiver does not arise.

12.2 Admittance Measurements

Several different types of antenna have been used, as illustrated in Fig. 12.1. The double wire type employ a spacing of about 1 mm, in

an attempt to impose a longitudinal field on the system. Best results were obtained with antennas of type B, though this may have been connected with the ferromagnetic nickel wire from which they were constructed. This is likely to have modified the magnetic field very close to the wires, and may well have improved the coupling to the plasma.

Fig. 12.2a shows the signal current received when transmitting between parallel-wire antennas. Since the transmitter voltage is fixed, the signal is related to the admittance between the antennas. Comparison of the admittance with the overall shape of ε_c (Fig. 11.2) shows basically the same form, falling to a minimum at f_T. The warm plasma effects are superimposed on this shape, localised to regions below f_T and near cyclotron harmonics. As near as can be measured, the admittance peaks, visible to 20 f_H, do fall at the gyrofrequency harmonics, as computed by Mantei (1967). All the predicted behaviour is exhibited near f_T, and more detail in this region is shown in Fig. 12.2b, while the response near f_H is shown in Fig. 12.2c, using different signal frequencies to alter the coverage of the ratio f/f_H. While the oxide cathode gives a more uniform plasma, it is not as stable as that from the hot filament over a wide range of magnetic field.

The admittance in Fig. 12.2b follows the general shape of ε_c, together with the oscillatory structure due to regions of cyclotron waves below f_T and above the gyroharmonics. Qualitatively, the agreement with Mantei's (1967) admittance computations, (Fig. 11.3), is good, but differences do occur in the size of the propagation regions, which in theory should extend out to the "nose" of the propagation window. in Fig. 12.2b, from the position of the upper hybrid null, $f_N^2 = .69\ f^2$, and the region of visible cyclotron wave interference extends above the second and third gyroharmonics to 2.38 f_H and 3.33 f_H respectively. For this plasma density, however, waves should be present to 2.51 f_H and 3.52 f_H, or rather more than is observed. The discrepancy is probably

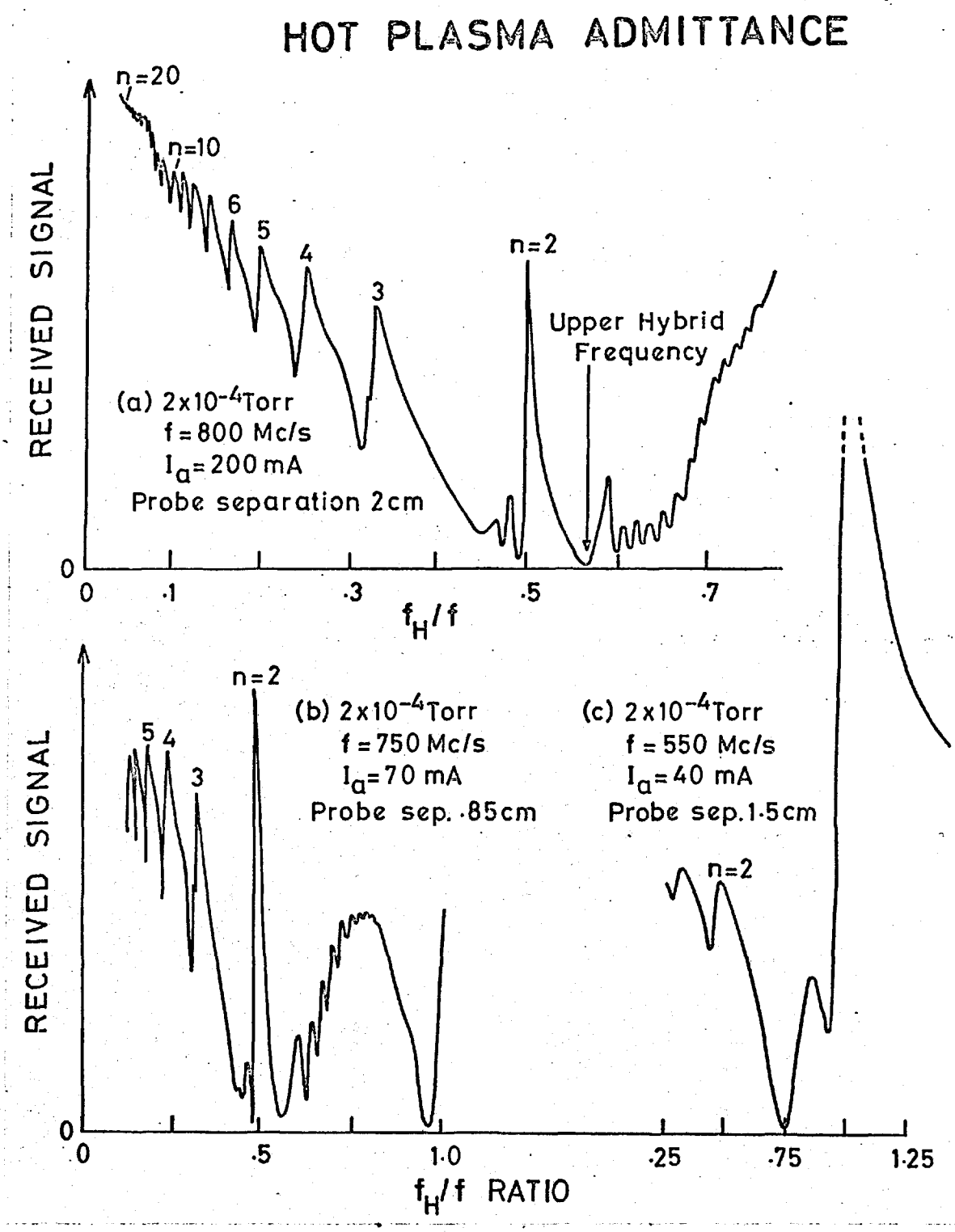


Fig. 12.2 The signal received (which is proportional to the admittance for a constant driving voltage) when transmitting between two antennas in the plasma. Curve (a) was obtained using a hot-wire cathode, which gave a stable plasma over a wide range of magnetic field, but one which was less uniform than that obtainable from the oxide cathode in (b) and (c).

due to collisional damping. It has been shown that the imaginary part of the wave vector k is $-i\nu/v_g$, where ν is the collision frequency, and so the low group velocity modes in the "nose" region of the dispersion curve will be attenuated first.

12.3 A Cold-plasma Sheath Resonance

The overall shape of the admittance curve below f_T is not completely understood. From Fig. 12.2b, the warm plasma oscillations are superimposed on a background which reaches a peak between ω_T and ω_c. From Fig. 11.2, ϵ_c is negative here, i.e. the plasma is inductive on cold theory. Since the antennas will be surrounded by a capacitive sheath, it is possible that a series resonance may account for the peak, as illustrated in Fig. 12.3. Due to the sheath impedence, a peak in admittance is now reached at f_R, rather than f_H. If the sheath capacitance is large (i.e. has a small impedence) the shift $(f_R - f_H)$ will be small.

The simplest antenna - plasma model of the experiment is drawn in Fig. 12.3b, in which the antennas of length l are surrounded by electron-free cylinders of radius R. The sheath capacitance C_s and the free space capacitance between the two sheaths C_o, are given by

$$C_s = \frac{2\pi\epsilon_o l}{\log R/R_o}$$

$$C_o = \frac{\pi\epsilon_o l}{\cosh^{-1} d/R}$$

These capacitances are plotted as a function of R in Fig. 12.3c, for an antenna radius R_o of .1 mm, as was used in the experiment of Fig. 12.2b. The Debye length here is about .2 mm, and since the RF sheath is probably several times this, (Holt and Lerfald, 1967) R may be ~1 mm. R and R_o are thus very different and C_s is small, which is the condition that $(f_R - f_H)$ is not small. In this experiment only one antenna had a .1 mm radius, the other being considerably larger, with a much greater sheath

capacitance. This means that the reactance of the sheath surrounding the thin antenna will dominate in the combined series sheath impedence. Assuming R = 1 mm, $C_s \doteq 2C_o$, and a series resonance between sheaths and plasma should occur when

$$C_s + \frac{\varepsilon_c}{\varepsilon_o} C_o = 0$$

i.e.

$$\frac{\varepsilon_c}{\varepsilon_o} = -2$$

For the data of Fig. 12.2b, $f_N^2/f^2 = .69$, and so the series resonance condition is reached at $f_H/f = .88$, which compares reasonably with the experimental peak at $f_H/f = .83$ when the antenna approximations are considered.

There are other tests one can apply to see if this is a resonance peak; for example a positive bias on the antenna should collapse the sheath. Experimentally, this had the reverse result to that anticipated on simple theories, a similar result to that found by Freeston (1968) during experiments with no magnetic field. A resonance, however, should occur at the same value of ε_c, regardless of frequency, for a given probe separation and plasma density. For a particular geometry, the following results were obtained at the admittance peak.

Frequency (Mc/s)	750	600	550
$\frac{\varepsilon_c}{\varepsilon_o}$	-.81	-.82	-.92

The near constant value of ε_c supports a resonance interpretation of the observed results. There are other frequencies, near the gyro-harmonics, at which the warm plasma reactance becomes inductive, and resonance effects near these frequencies should also be present, though they are probably swamped by the other effects at these frequencies.

12.4 Measurements with Moving Probes

Equation 11.5 predicts that the electric field within a Bernstein

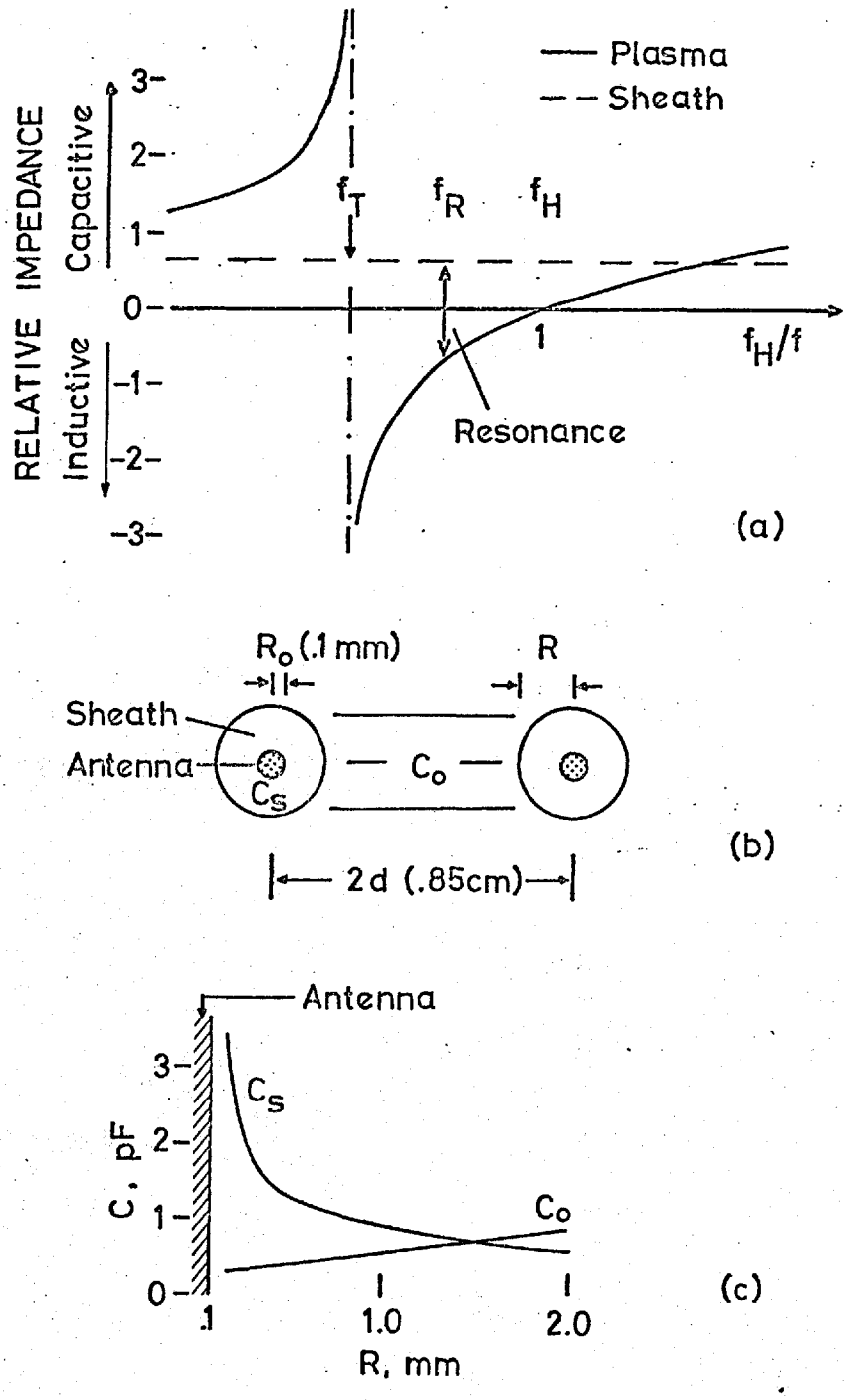


Fig. 12.3 The origin of a cold plasma-sheath resonance. (a) The impedances of the plasma and the electron-free sheath as f_H is varied. In a series combination, the two impedances resonate at f_R. (b) A simple model of parallel wire antennas immersed in the plasma. C_o is the vacuum capacitance between cylinders equal in size to the sheath. The variations of sheath capacitance C_s, and C_o as the sheath radius R is changed is shown in (c). Only for R very small is the sheath impedance negligible.

pass-band should have a spatially dependent amplitude, which should cause the admittance between probes to exhibit a related spatial behaviour. This is readily checked with the moving probe. The output from several such sweeps is shown in Fig. 12.4 and clearly shows the expected wave structure superimposed on a decaying background. Waves in the region of continuous propagation (below f_T) are relatively easy to excite, and have considerable amplitudes. Since for a given transmitting frequency, the wave number k is dependent on the electron density, the progressive change of the wavelength with probe separation which is frequently seen, reflects the radial density profile of the plasma column.

The wave amplitude below f_T decreases progressively as the ratio f/f_H is reduced to the gyro-harmonic below. In the first band, propagation has not been observed below typically $f/f_H = 1.2$. Three factors may account for this:

1. From equation 11.3, the amplitude of the electric fields goes as $\frac{1}{k}$, i.e. they decrease as the frequency is lowered and the wavenumber rises.

2. As k increases, the group velocity v_g tends to zero, so that the imaginary part of k (in the presence of collisions), $-i\nu/v_g$, produces increasing damping.

3. One would not expect to see a wavelength smaller than the "collector" size, that is, the diameter of the antenna and its sheath.

In this discharge, the Debye length is quite large (~.2 mm). If the sheath is much larger than this, the latter point suggests that the smallest antennas used here (.1 mm radius) were unnecessarily small, as the sheath is the major contributor to the collector size. Mantei (1967) however, reports more clearly defined admittance peaks with antennas of small radius; possibly the efficiency of the wave-antenna coupling depends on the ratio R_o/R in Fig. 12.3.

The records of Fig. 12.4 corresponding to frequencies above the

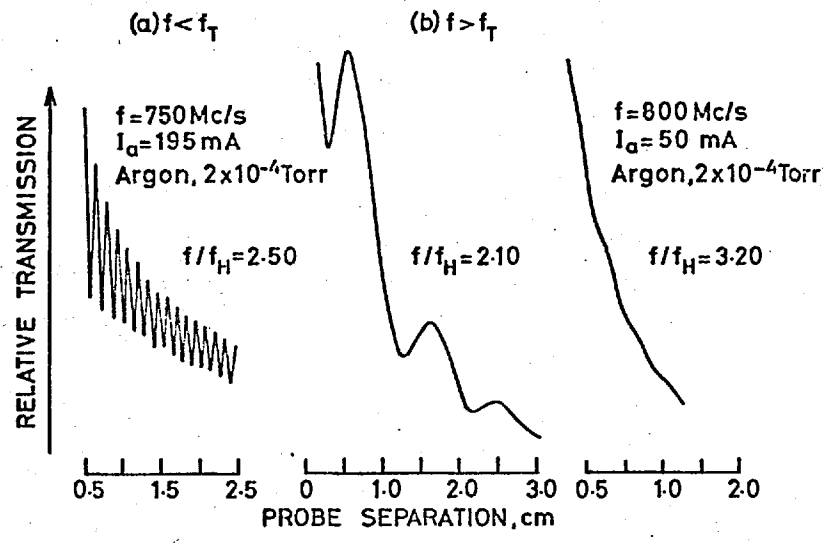


Fig. 12.4 Signal received as the antenna separation is increased. The oscillatory response is due to the interference of a propagating cyclotron wave with the capacitively coupled signal.

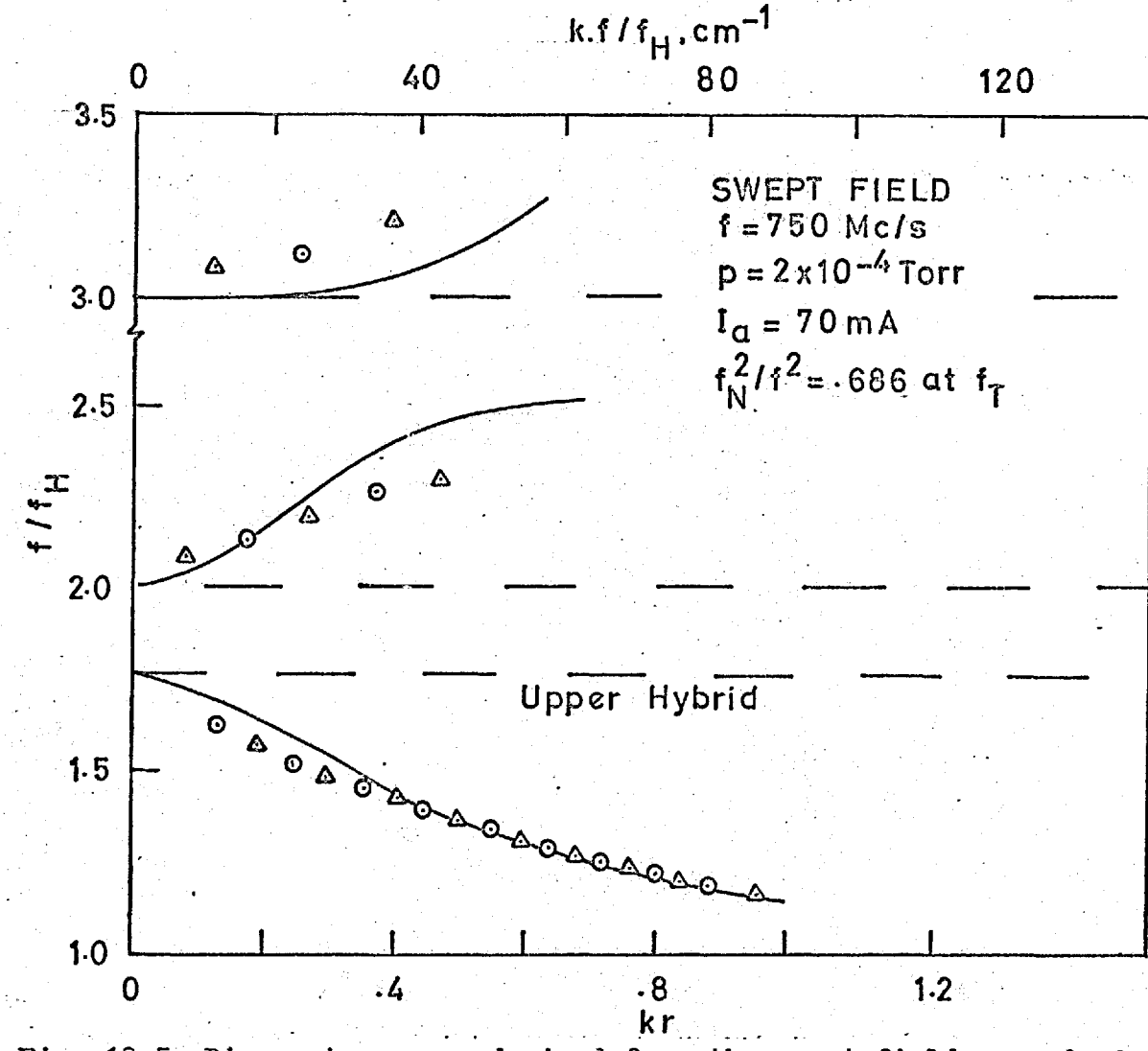


Fig. 12.5 Dispersion curve derived from the swept field record of Fig. 12.2(b), in which circles and triangles represent points of maximum and minimum admittance respectively. The full line is the theoretical curve for the value of plasma density deduced at the upper hybrid null. Discrepancies between theory and experiment are attributed to density variations as the magnetic field increases.

second and third gyroharmonics clearly demonstrate the existence of propagation bands near multiples of f_H and above f_T, and further illustrate the greater damping at the higher harmonics. This is to be expected due to the lower group velocities with increasing harmonic number (Fig. 10.4). Physically, on arguments of phase bunching of the electrons, a wave at f_H requires particles to be collision-free for a time of the order of the cyclotron period; to produce a comparable effect at the same wave frequency, when this is now the n^{th} harmonic of f_H, requires f_H to be lowered n times, and for the particles to remain phase-bunched for n wave-periods, or one new cyclotron period, clearly a more stringent requirement. In the example of Fig. 12.4b, waves were seen only from 2.07 to 2.21 f_H, and 3.12 to 3.22 f_H, corresponding to the fastest waves in the band. Theoretically propagation should have been seen from $2 - 2.3\ f_H$ and $3 - 3.3\ f_H$ for this density.

No experimental evidence has been seen of the second cyclotron mode above f_T. It is thought this is related to its shorter wavelength, its theoretically decreased amplitude, and its increased collision damping which arises from its low group velocity compared with the short-k mode at the same frequency.

12.5 The Dispersion Relation

The ultimate quantitative check on the Bernstein wave predictions is to derive the dispersion relation experimentally. This may be achieved here in two ways, of which the fastest is sweeping ω_c/ω. It is known that the progression from an admittance maximum to a minimum is a result of the addition or subtraction of one cyclotron half-wavelength between transmitting and receiving probes. The ambiguity in the integral number of wavelengths between the antennas is resolved by the knowledge that this is zero adjacent to a harmonic of f_H or at f_T, since the wavelength is infinite ($k = 0$) here. Knowing the antenna spacing then enables

the wavelength to be found as a function of ω_c/ω as one moves away from such points. A complication in the laboratory (when ω_c is swept) arises because the plasma density depends slightly on the magnetic field, and the method is inaccurate above f_T, where few interference maxima are seen (e.g. Fig. 12.2). Another problem is the effective separation of the antennas. Normally the physical separation d is taken, but unless this is large compared with the sheath thickness s, a systematic error is introduced.

The dispersion curves of Fig. 12.5 have been derived from the data of Fig. 12.2b, which enables values of k to be found as a function of ω/ω_c. The continuous lines give the computed curves for $\omega_p^2/\omega^2 = .686$, deduced from the upper hybrid transmission null. As such solutions are in terms of kr, where

$$kr = k\frac{v_T}{\omega_c} = \frac{\omega}{\omega_c}k.\frac{v_T}{\omega},$$

ω/ω_c was first plotted against $k.\frac{\omega}{\omega_c}$, which was then scaled to fit the theoretical data below the upper hybrid frequency. The scale factor v_T/ω contains the electron temperature, here 1.57 ev or 18,200°K, rather less than that implied by Langmuir probes for reasons discussed. The discrepancies between the theory and experiment are systematic, and can be explained by the fact that the density is not constant, but increases slightly with magnetic field. Above $3f_H$, the experimental points are rather unreliable.

It has been assumed that at the admittance maxima

$$n\lambda = d \quad \text{or} \quad k = \frac{2\pi n}{d}$$

When an effective sheath s around each antenna is assumed, d is reduced and

$$k = \frac{2\pi n}{d(1-\frac{2s}{d})}$$

If s is constant, k is in error by a constant fraction, and the earlier value of electron temperature should be reduced by the factor $(1-\frac{2s}{d})^2$. Whether or not this effect is significant has been tested by measuring wavelengths directly in the experiment from which the dispersion curves were constructed, using the moving probe facility, which gives a true value of λ unaffected by sheaths to an accuracy of 1 - 2%. For a given value of ω/ω_c we have

$$\lambda_t = \frac{d-2s}{n} \qquad \lambda_a = \frac{d}{n}$$

i.e. $\frac{\lambda_a - \lambda_t}{\lambda_t} = \frac{2s}{d-s}$, independent of n, where λ_t and λ_a refer to the true and apparent values of λ found from moving probe and swept field measurements respectively. The following results were obtained :-

ω/ω_c	λ_t, mm	s, mm	s/λ_D
1.52	2.97	.73	4.5
1.38	1.72	.55	3.5

The Debye length λ_D was found from the temperature given earlier, but is not strongly dependent on T_e. While the sheath estimates are subject to quite large errors, they are compatible with other estimates of RF sheaths (e.g. Holt and Lerfald, 1967), and the sheaths inferred when considering the effects of antenna capacitances in section 11.3.

The shortest wavelength observed experimentally was about .8 mm, which is comparable with the sheath, rather than the antenna size of .1 mm radius. This limitation makes it unlikely that two waves could be detected above f_T, even apart from considerations of amplitude. Consider the propagation above $2f_H$ in Fig. 12.5. Propagation is not seen beyond 2.3 f_H, when $\lambda = 3.7$ mm for the long wavelength mode. At this point, the second (short) wavelength is theoretically .85 mm, the minimum detectable, so that in the band where the long mode is seen, the second wavelength is

always shorter than .85 mm, and unlikely to be seen in this apparatus. A tube with an inherently smaller Debye length is required to reduce the the collecting size of the antenna.

The problems of sheaths and field-dependent densities can be overcome by using the movable probe at different operating frequencies to obtain λ directly. The result of such an experiment is shown in Fig. 12.6, for conditions where propagation was continuous between one and two f_H. To facilitate comparison with theoretical curves, (computed in terms of kr), without assuming a value of electron temperature, the ratio $k/k_{(f=1.5f_H)}$ is plotted, rather than k. It appears that with the possible exception of long wavelengths, the experiment agrees reasonably well with theory.

The probable existence of a non-thermal tail in the electron velocity distribution has been mentioned. For propagation strictly perpendicular to the magnetic field, the parallel velocity component does not affect the dispersion equation, since $k_{\parallel} = 0$ (Crawford, 1964). However, as a result of collisions and field non-uniformities, a proportion of the streaming electrons will acquire a velocity transverse to the field, which does affect the dispersion function. To allow for this, it was assumed the density consists of a fraction α electrons with a Maxwellian distribution, and the remainder with a ring velocity distribution

$$f_o(v_\perp, v_\parallel) = \frac{1}{2\pi v_{o\perp}} \delta(v_\perp - v_{o\perp})\, \delta v_\parallel ,$$

i.e. particles of velocity $v_{o\perp}$ circulating with zero parallel velocity. The dispersion equation for such a mixed distribution, derived from Tataronis (1967) is

$$\sin \pi\Omega + \frac{\omega_p^2}{\omega_c^2} \int_0^\pi \sin \Omega y \sin y \cdot \left\{ \alpha \exp -\lambda(1+\cos y) + (1-\alpha) J_o\left(\frac{2v_{o\perp}}{v_T} \lambda \cos \frac{y}{2} \right) \right\} dy = 0$$

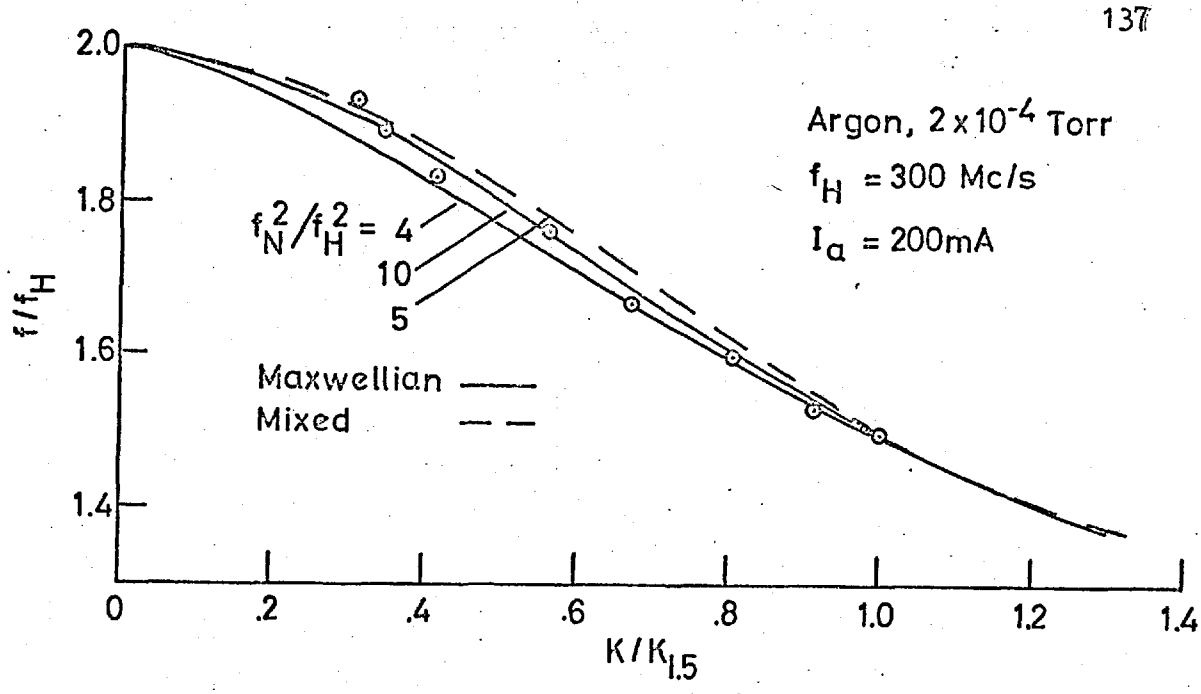


Fig. 12.6 Dispersion curve branch derived using the moving probe. The experimental points are well bracketed by the two theoretical Maxwellian dispersion curves, while that for a mixed velocity distribution is discussed in the text.

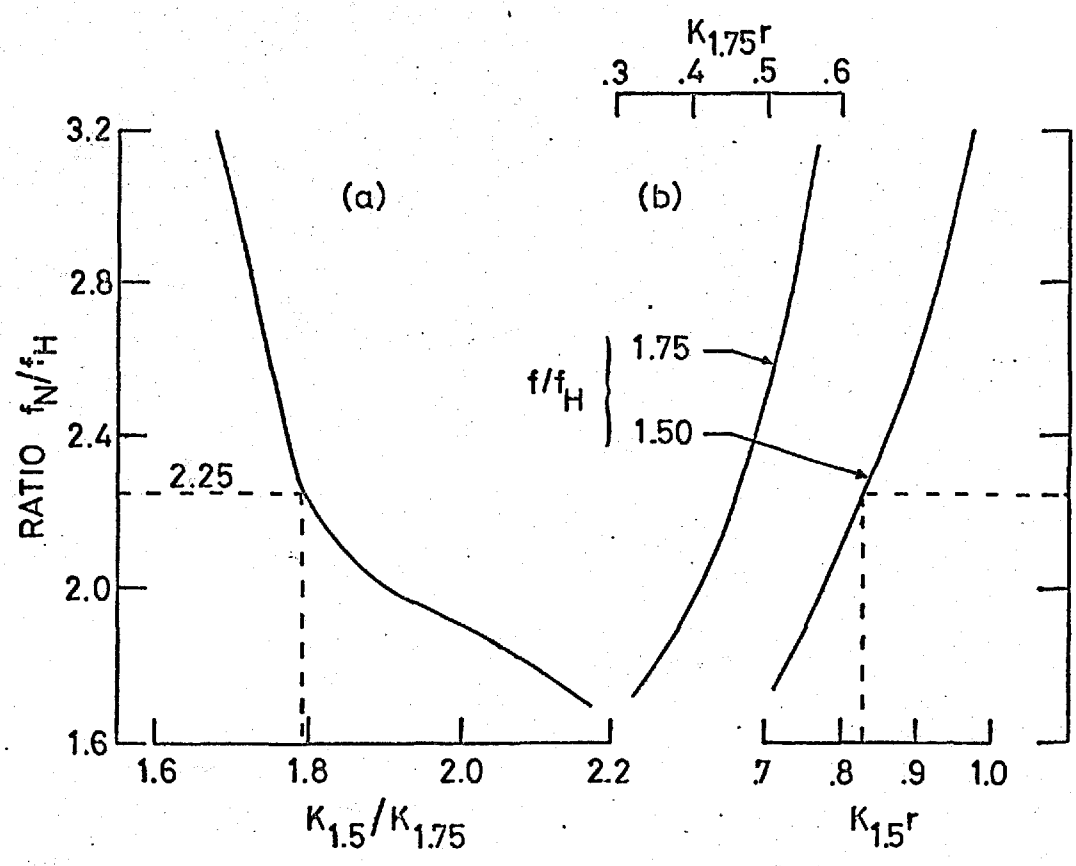


Fig. 12.7 Theoretical curves involving measurements at two frequencies from which plasma parameters may be extracted. The dashed lines refer to the example in the text.

J_o is a Bessel function of the first kind, and all other quantities are as defined earlier. The solution of this equation is included in Fig. 12.6 as the dashed line for $\omega_p^2/\omega_c^2 = 5$ (a value derived below), $\alpha = .9$, implying a high proportion of the electrons are streaming, and $v_{o\perp}/v_T = 3$. The latter corresponds to a non-thermal "temperature" 9 times the Maxwellian.

Apparently even this proportion of non-thermal particles does not radically change the dispersion curves. The largest deviation from the thermal plasma occurs near $f/f_H = 1.7$, when the experimental points are bracketed well by the Maxwellian curves. It therefore appears that the discrepancies above $f/f_H = 1.9$ are not caused by a high energy plasma component, and are probably associated with the difficulties in measuring long wavelengths accurately.

12.6 Plasma Measurements

A technique is suggested by Fig. 12.6 for measuring temperatures, and with less accuracy, plasma densities. If f_H is constant, the gyroradius r, containing the electron temperature is also constant, but both r and f_N may be extracted from measurements at two frequencies, subscripted 1 and 2. Since kr is a known function of f/f_H and f_N/f_H, we have

$$k_1 r = F(f_1/f_H, f_N/f_H)$$

$$k_2 r = F(f_2/f_H, f_N/f_H),$$

and the ratio k_1/k_2 is then a known function of density for given values of f_1/f_H and f_2/f_H. The dependences of $k_1 r$, $k_2 r$ and k_1/k_2 on f_N/f_H have been computed for $f_1 = 1.50\ f_H$ and $f_2 = 1.75\ f_H$, corresponding to the data in Fig. 12.6, and are shown in Fig. 12.7. From the former, $k_{1.5}/k_{1.75} = 1.79$, so that $f_N = 2.25\ f_H$, or 675 Mc/s. Also, when $f_N = 2.25\ f_H$, $k_1 r = .83$, and since $k_1 = 30.4\ cm^{-1}$ it may be deduced that

$$T_e = 17{,}200^\circ K$$

This solution has been illustrated graphically, but it could be programmed to allow greater flexibility in the choice of frequencies. A completely analogous technique is possible in which the group velocity, rather than kr, is considered as a function of density and frequency. It is clear from Figs. 12.6 and 12.7 that the plasma frequency is only a weak function of the ratio k_1/k_2, but this is an advantage where temperature measurements are concerned. Ideally, one would measure the plasma frequency, using a swept frequency and tracking receiver, to locate the upper hybrid null, unaffected by sheaths. The electron temperature follows from a single measurement of k or v_g, since kr or v_g/v_T may be computed at that density and wave frequency.

Note Added: Recent measurements (T. A. Hall, unpublished results), using the moving probe and improved recording equipment have shown excellent agreement with the theoretical Maxwellian dispersion curves, confirming the conclusions of section 12.5.

13: Applications of Electrostatic Waves

13.1 Direct Resonance Measurements

The final section of this work is concerned with the application of electrostatic signals to measurements in space. The discussion falls into two categories, the first largely concerning simple measurements which have been made from ionogram resonances, and second a discussion of the type of experiment which might be conducted using discretely excited cyclotron waves.

Clearly, the simplest measurement which can be made is of the scalar magnetic field, if it is assumed that the gyroresonances do not, in practice, show deviations from integral multiples of f_H (Thomas, 1964; Thomas and Colin, unpublished work). In Fig. 13.1 the earth's field has been found for two passes from the gyroharmonics, weighting the higher harmonics because of their greater inherent accuracy. For the nth harmonic

$$f_r = 2.799\ B.n \quad (Mc/s,\ Gauss)$$

then

$$\delta B = \delta f_r / n$$

It is estimated that with the ionogram film format, the accuracy of frequency determination with Alouette I is usually from ± 20 Kc/s to ± 35 Kc/s. The corresponding uncertainty in the magnetic field as measured from the nth harmonic is as follows

n	δB, γ ($\gamma = 10^{-5}$ gauss)	
	$\delta f_r = \pm$ 20 Kc/s	$\delta f_r = \pm$ 35 Kc/s
1	± 700	± 1260
5	± 140	± 250
9	± 78	± 140

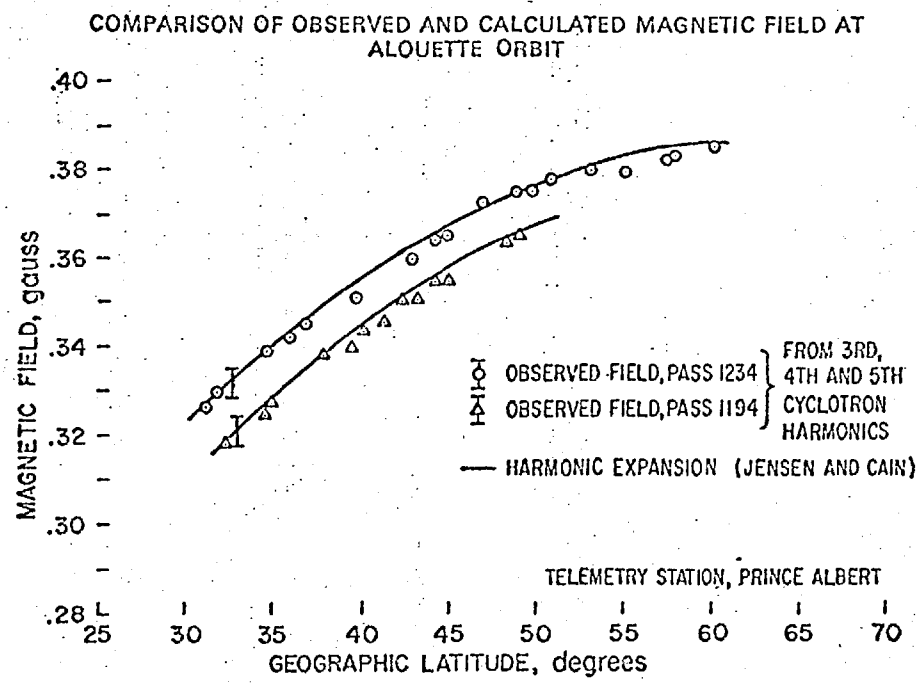


Fig. 13.1 Comparison of the Earth's magnetic field as deduced from gyroresonances with that computed from the harmonic expansion GSFC 12/66 for two passes of Alouette I over North America at an altitude of approximately 1010km.

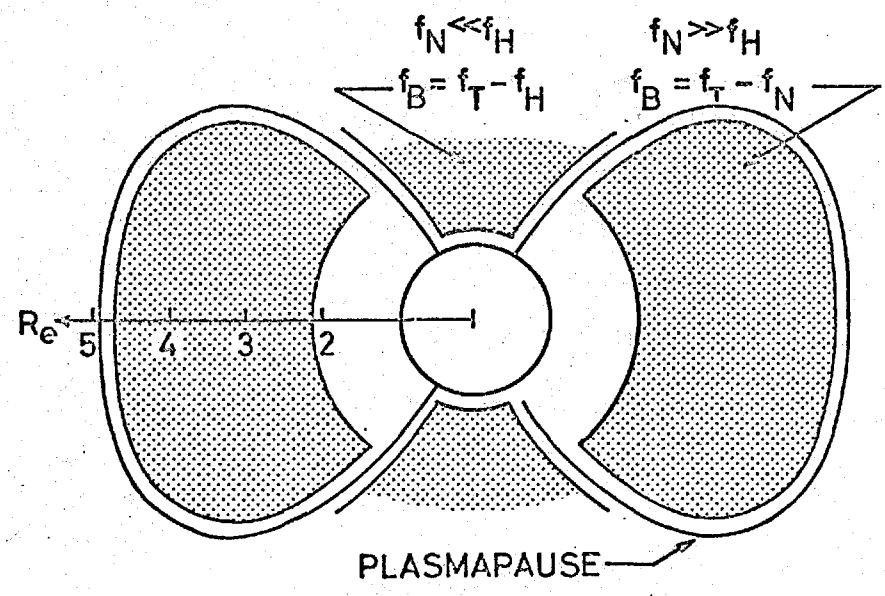


Fig. 13.2 Schematic diagram showing the approximate regions in space where beats might be expected because of the order of magnitude difference between the electron gyrofrequency and the plasma frequency. Beats over the polar regions of the earth have been detected; the possibility of beats in the plasmasphere is inferred from probable particle densities in the area.

The percentage error in measuring the field at the Alouette orbit from the ninth harmonic is about .3%. Also shown in Fig. 13.1 is the main field of the earth computed from the spherical harmonic expansion GSFC 12/66 of Jensen and Cain. This field is that due to magnetic sources within the earth which can, from potential theory, be shown to account for more than 99% of the geomagnetic field. Clearly this technique of field measurement is to be regarded as a sometimes useful bonus rather than an experiment in its own right, as better magnetometers are available.

More useful is the measurement of plasma density from the f_N resonance. With the ionogram format of Alouette II, frequency measurements may be made to an accuracy of $\pm$ 0.005 Mc/s below 2 Mc/s, where the sweep rate is low. If a more typical value of $\pm$ 10 Kc/s is taken to be the accuracy with which the f_N resonance can be determined, the corresponding errors in the electron density are

$\pm$ 7%	at	280 el/cc	(f_N = .15 Mc/s)
$\pm$ 2%	at	3,100 el/cc	(f_N = .50 Mc/s)
$\pm$ 1%	at	49,600 el/cc	(f_N = 2.0 Mc/s)

The accuracy obtainable falls at higher frequencies because of the faster sweep rate above 2 Mc/s.

13.2 Excitation of Beats between Plasma Resonances

When two resonances are excited simultaneously and both lie within the bandwidth of the detecting equipment, the resulting signal will show beat interference. Using Alouette II data, Hagg (1967) identified a regular modulation on the f_T resonance as a beat between f_T and f_H. From the beat frequency, he was able to deduce electron densities down to 8 el/cc. These measurements were made at altitudes of about 2000 km in zones above the poles where the plasma frequency was much less than the gyrofrequency, so that the beat frequency

$$\sqrt{f_N^2 + f_H^2} - f_H$$

may be approximated by

$$f_b \simeq \frac{1}{2}\frac{f_N^2}{f_H} \quad \text{or} \simeq \frac{KN}{f_H}$$

where N is the electron density and K a constant. Since the field in these regions is known to good accuracy, the accuracy of the density measurement is set by the accuracy with which the beats may be measured, which, at the low frequencies concerned, could be quite high in an experiment designed for this purpose. This beat is also common on Alouette I polar ionograms, and has been used extensively in N(h) analysis.

At greater heights within the plasmasphere, the situation is reversed and the plasma frequency greatly exceeds the gyrofrequency (Angerami and Thomas, 1964). In this situation, the upper hybrid resonance is now close to the plasma frequency, and a low frequency beat of less than 10 Kc/s may be expected between these two resonances at altitudes above 2Re. Fig. 13.2 shows the zones of the magnetosphere where the two kinds of beat may be excited. For magnetospheric measurements, the polar type of beat is more useful as it detects ambient plasma densities difficult to measure by other techniques. The second class of beat yields the plasma frequency and a coarse measurement of magnetic field.

13.3 Experiments with Electrostatic Waves

The work of Chapter 12 suggests that it may be possible to conduct electrostatic wave experiments in space. The experiment essentially would derive part of the dispersion curve, which would then be compared with computed curves for various plasmas. The parameters extracted would be both the electron density and temperature, which modify the dispersion curves. The great advantage of such experiments is that one is measuring a bulk plasma effect on the propagation of a wave, and the results should be independent of sheaths and the vehicle potential.

Some characteristic lengths and frequencies in the ionosphere and magnetosphere are illustrated in Fig. 13.3. At all altitudes of interest, the space plasmas approximate far more than laboratory plasmas to the infinite, uniform, collisionless plasmas of theoreticians.

The physical size of the antennas needed to excite plasma waves in space is not excessive even at altitudes of several earth radii, if the requirement is taken to be a radiator of a size comparable with the electrostatic wavelength. For experiments involving the gyroresonances, values of kr of the order of 2 are necessary. In terms of the wavelength λ, we have then

$$\lambda \sim \pi r$$

In the topside ionosphere, r is about 2.4 cm for a 1500°K plasma; at 5 Re (approximately a geo-stationary orbit) r is 7.8 metres for a plasma temperature of 10,000°K. Thus the required wavelength is still only ~20 metres. In the latter case, a greater problem arises due to the fact that the Debye length at this extreme altitude is estimated to be several metres. If an antenna radiating in such a tenuous plasma still has an R.F. sheath several Debye lengths about it, it would require the propagation path to be long, unless the sheath could be collapsed by biasing. It could well be, however, that the sheath size at great altitudes will restrict possible experiments to the plasma ringing type of the previous section, in which the ambient plasma is shocked by a strong pulse.

Propagation information may be compared with theoretical dispersion curves via either group velocities or direct $\omega - k$ measurements. The topside sounder experiment immediately suggests a pulse delay experiment, where the time of flight of an electrostatic pulse is measured over a known distance. This has been successfully accomplished in the laboratory (Crawford, Harp and Mantei, 1967). Such an experiment has the advantage that the fast, capacitively coupled signal, the $k = 0$ mode, is automatically separated from the slow cyclotron wave, and looks attractive in the lower

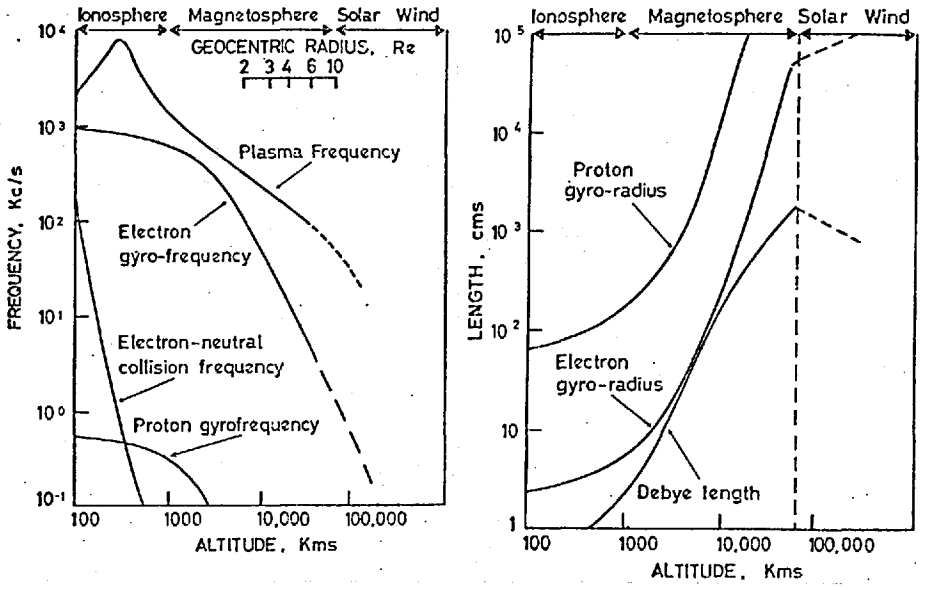


Fig. 13.3 Relative magnitudes of important frequencies at altitudes between 100km and the solar wind. Electron resonance phenomena, of frequencies above the gyrofrequency and near the plasma frequency, are orders of magnitude above the electron-neutral collision frequency and characteristic ion frequencies. Right: Characteristic lengths over the same altitude range.

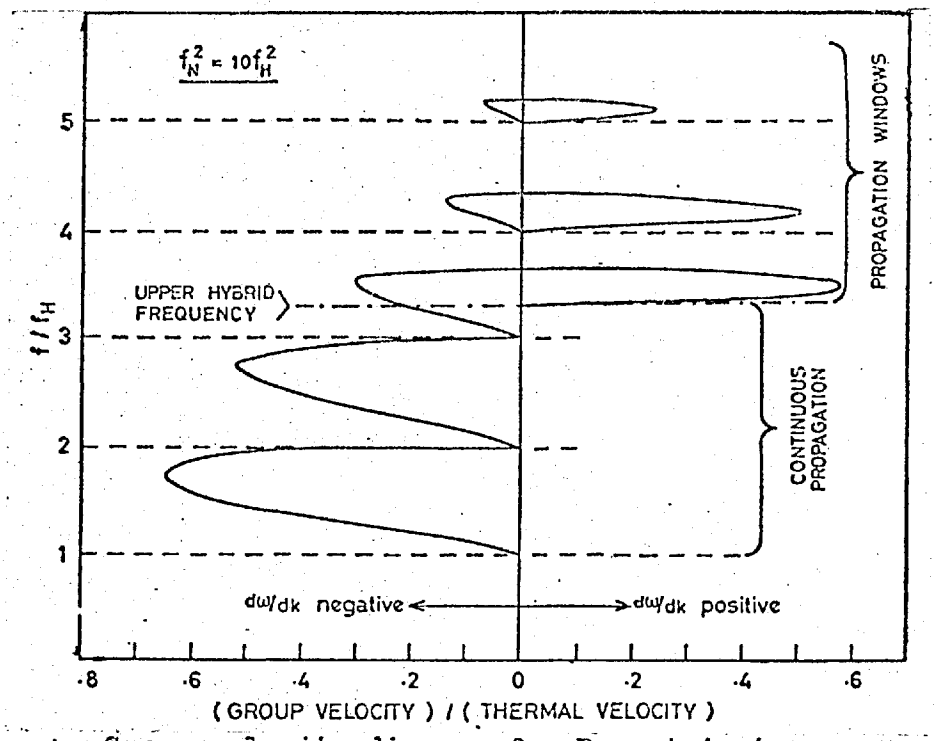


Fig. 13.4 Group velocity diagram for Bernstein-type propagation inside the plasmasphere where $f_N^2 = 10 f_H^2$. Continuous propagation is possible up to the third harmonic, in this case, before discrete propagation windows appear. For a geostationary orbit, $f_N \simeq 10 f_H$, and on Bernstein theory, continuous propagation would be obtained up to about the tenth harmonic of the gyrofrequency.

magnetosphere. Here $f_H << f_N$, and there are many branches on the dispersion curves below f_T, where the propagation is continuous as frequency increases, and the group velocity does not go through zero for non-zero $\underline{k}$. Thus the closed "loops" of group velocity found above f_T become broader half loops below f_T. Some computed examples are illustrated in Fig. 13.4 for the case $f_N^2 = 10 f_H^2$, corresponding approximately to a magnetospheric altitude of 3 Re. In this case, continuous propagation is obtained below about the third gyroharmonic. The advantage in operating in the region of continuous propagation is that values of $dv_g/d\omega$ are lower than those above f_T, and thus delays can be measured with a minimum of pulse dispersion, which results from the differing velocities of the pulse frequency components.

However, pulse experiments need more consideration. It is desirable that the length of the pulse of energy received should be small in comparison with the total delay of the pulse. The pulse length (i.e. number of cycles), cannot be indefinitely reduced as this widens its Fourier spectrum, and the dispersive effects of the medium may then cause unacceptable broadening. In ionosondes, the pulse length is typically 100 μs at a frequency of 1 Mc/s, or a pulse length of 100 R.F. cycles, which will be taken here as a reasonable length in an electrostatic sounder.

Ideally, one would require a pulse time of flight ten times the undispersed pulse width to make accurate time delay measurements. Let D be the path length, f the operating frequency and v_g the group speed of the wave. Thus we need

$$D > \frac{10^3 v_g}{f} \qquad (13.1)$$

For ionospheric conditions, (e.g. Fig. 10.4) operating at $2f_H$, or 2Mc/s, the most extreme case comes from the maximum group speeds, which are about 10^4m/s. In this case, D must be 5 metres or more, which is practicable. In the magnetosphere however, the gyrofrequency has fallen and typical

group speeds risen to the extent that D becomes prohibitively large for operation at low gyroharmonics. As an illustration of the requirements at 3Re (Fig. 13.4), when the frequency is between one and two times the gyrofrequency (10 Kc/s), the maximum v_g is about .6 v_T, i.e. about 10^5m/s. Then to achieve the desired pulse-length to travel-time ratio, a value of D in excess of 10^4m is required , which is clearly impracticable. A more realistic approach would be to set D to what might be possible in practice, say 20 m, (which is a minimum as the path must be at least several gyro radii) and to seek a possible region where the ratio v_g/f is suitable. In practice this clearly means using the high order harmonics of the gyrofrequency, which has the effect of both reducing v_g and increasing f in (13.1). The operating region is now away from zones where the group velocity changes slowly with frequency as described above. The data contained in Fig. 13.4 suggest that the largest group velocities encountered would still be perhaps .1 v_T or about 10^4 m/s, in which case a frequency of 500 Kc/s, which is 50 f_H, is needed. It is doubtful whether such experiments are feasible, though more favourable figures would be obtained if the requirement that the time of flight be ten times the pulse width were relaxed. Possibly a more useful approach in the magnetosphere would be via the analogue of the swept field technique used in the laboratory to obtain dispersion curves from admittance measurements. As mentioned previously, there are several branches of the magnetospheric dispersion curve where propagation is continuous. For a region of space where the gyroradius is 2 metres, the range of kr of interest - say .2 to 3 - corresponds to wavelengths from 60 to 4 metres. If it is possible to arrange a propagation path comparable to the first wavelength, many admittance maxima like those of Chapter 12 should be seen when now the transmitter frequency is swept. A smaller spacing would result in fewer admittance oscillations. Fig. 13.5 shows a laboratory simulation of the type of record obtained when $f_N \gg f_H$, giving many continuous propagation

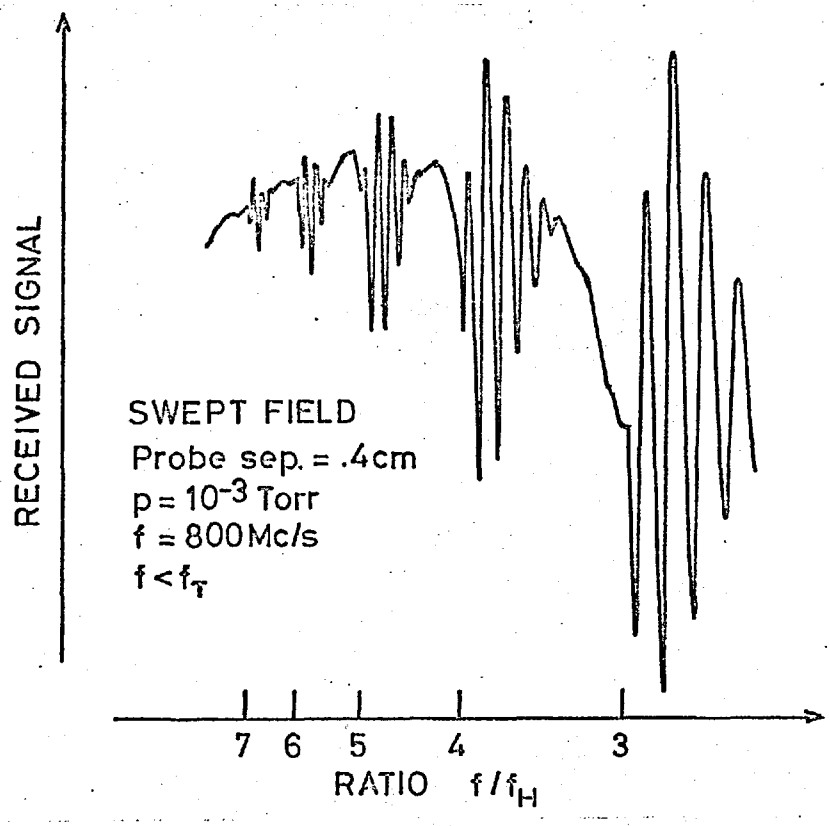


Fig. 13.5 The signal transmitted between two parallel probes in a laboratory plasma for which $f_N \gg f_H$, showing interference in the regions of continuous propagation below the gyroharmonics. A similar situation exists in many regions of space, and could be the basis of an admittance experiment to derive plasma parameters.

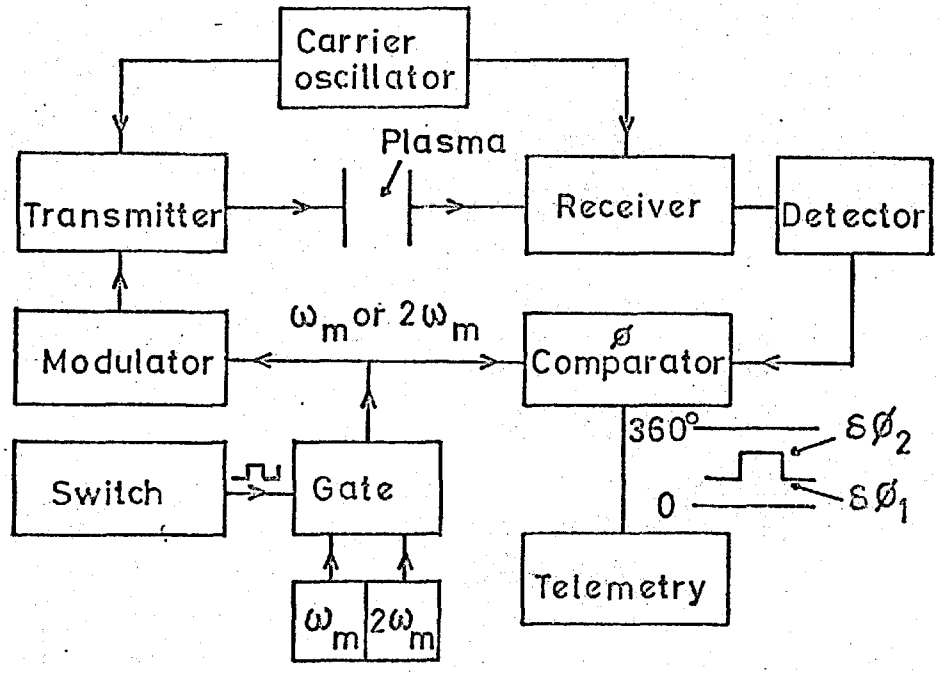


Fig. 13.6 Outline of an experiment to measure Bernstein mode group velocities in the lower magnetosphere by a phase technique. From measurements at two frequencies, electron temperatures and densities could be found.

bands below f_T. This technique is the basis of a proposed space experiment (T. A. Hall, Imperial College Note, 1969). While it should operate at both ionospheric and magnetospheric altitudes by judicious antenna spacings, it suffers from the disadvantage that a complete and continuous frequency sweep is required.

It is not feasible to obtain the electrostatic wavelength directly from phase measurements, as there will be a phase ambiguity of $2n\pi$ radians after a propagation path of many wavelengths. There appears to be an alternative method of finding the group velocity using a CW. technique. The advantage lies in the fact that although the carrier is modulated, the system bandwidth can be made much smaller than that used in pulse experiments. Assuming that the magnetic field is known, knowledge of the group velocity at two frequencies is sufficient to establish both the electron density and temperature.

The E.S. waves launched by an antenna consist of two types

1. One or two propagating cyclotron waves
2. A non-propagating, capacitive ($k = 0$) signal.

We transmit an amplitude modulated signal, proportional to $(1 + A \cos \omega_m t)\sin \omega t$, i.e. the three components

$$\sin \omega t \; + \; \frac{A}{2} \sin(\omega + \omega_m)t \; + \; \frac{A}{2} \sin(\omega - \omega_m)t$$

It is assumed that the group velocity is constant over a band of the order of the modulating signal, i.e.

$$v_g = \frac{d\omega}{dk} = \frac{\omega_m}{\delta k} = \text{constant.}$$

The three components transmitted in the cyclotron mode will arrive at the receiver, distant x from the transmitter, as

$$\sin(\omega t + kx), \quad \frac{A}{2} \sin\left\{(\omega t + kx) \pm (\omega_m t + \delta kx)\right\}$$

i.e.

$$\left\{1 + A \cos(\omega_m t + \delta kx)\right\} \sin(\omega t + kx)$$

in the region of one propagating mode. Compared with modulating signal, the detected output is phase shifted an amount $\delta\phi$ where

$$\delta\phi = \delta k x$$

and

$$v_g = \frac{\omega_m x}{\delta\phi}$$

A low modulating frequency ensures that the modulation phase change over an R.F. path of many wavelengths is small, and that the phase comparison may be made simply.

Unfortunately, the capacitively coupled mode is also received, with zero phase shift. We then have two components, with and without phase shifts, whose amplitudes a and b are in an unknown ratio depending on the path length and the plasma parameters. The capacitive signal cannot be nulled out as in many plasma density probes, since we wish to remove not only the free space capacitance effect, but also that contributed by the "cold plasma".

After detection and filtering, we have the modulating voltages

$$a \cos \omega_m t + b \cos(\omega_m t + \delta k x)$$

i.e.

$$\mathrm{Re}\left\{ e^{i\omega_m t}(a + b \cos \delta k x + ib \sin \delta k x) \right\}$$

Expressing this in amplitude - phase form, compared with the modulating signal, the phase is now

$$\delta\phi = \tan^{-1} \frac{\sin \delta k x}{a/b + \cos \delta k x}$$

This phase depends on the relative amplitudes of the components. If the experiment is repeated using a modulating frequency $2\omega_m$, δk also doubles as we have assumed v_g is constant. The ratio a/b should not change, nor should it be affected by a change in modulation percentage. Thus

$$\delta\phi_1 = \tan^{-1} \frac{\sin \delta k x}{a/b + \cos \delta k x}$$

$$\delta\phi_2 = \tan^{-1} \frac{\sin 2\delta k x}{a/b + \cos 2\delta k x}$$

from which δkx may be extracted. A possible experiment is outlined in Fig. 13.6. When the capacitive signal is absent, $a = 0$ and $\delta\phi_2 = 2\delta\phi_1$, and this fact could be used in an automatic experiment to eliminate the unwanted signal by a feedback technique. While only one phase would need to be telemetered, the increase in electronic complexity is considerable.

13.4 Future Work

Problems still to be investigated in this work relate to the feasibility of cyclotron-mode experiments in space. Foremost among these is the effect of a propagation path which departs from purely perpendicular to the magnetic field. It is not known presently at what angle perpendicular effects cease, but this could be investigated with the current laboratory equipment. It appears that the sheaths about the antennas could be collapsed without altering the dispersion properties but further measurements on this remain to be made. The removal of the sheaths is probably a necessity at magnetospheric altitudes, but only a small source of error in the ionosphere. Finally, it is intended to investigate in the laboratory the possibility of measuring group velocities by the phase technique proposed in the previous section.

Appendix I

Numerical Solutions of the Bernstein Dispersion Equation

The following tabulations cover values of the plasma density factor f_N^2/f_H^2 between 1 and 10. This includes the ionospheric, and much of the magnetospheric plasma. The computations have assumed the electrons have a Maxwellian velocity distribution. Column headings are as follows:-

KR .	Wavenumber x electron gyroradius
OMEGA	Ratio f/f_H corresponding to the value KR
V GROUP	Group velocity of the mode, normalised to the thermal speed v_T

The latter velocities are given with the sign of the dispersion curve slope at the point of computation; this is simply an aid linking the group velocity and the relevant portion of the dispersion curve, for, as described in Chapter 11, the group velocity is always positive, carrying energy away from the radiator.

Values of V GROUP are to be multiplied by the electron thermal speed to obtain the actual speed. For an electron gas of temperature T^oK,

$$v_T = 3.9 \times 10^3 \sqrt{T} \text{ m/s}$$

For $T = 1000^oK$, $v_T = 1.23 \times 10^5$m/s, while the speed for a temperature of $10{,}000^oK$ is 3.9×10^5m/s. Thus, as a result of its weak temperature dependence, v_T, or the scale factor in the group velocity tabulations, is always about 2×10^5m/s for space plasmas.

BERNSTEIN MODES - NUMERICAL SOLUTIONS

Density factor = 1.0

KR	OMEGA	V GROUP
5.0	1.003	-0.1765E-02
4.5	1.004	-0.2643E-02
4.0	1.006	-0.4134E-02
3.5	1.008	-0.6823E-02
3.0	1.013	-0.1204E-01
2.5	1.021	-0.2316E-01
2.0	1.039	-0.4948E-01
1.5	1.077	-0.1146E 00
1.0	1.164	-0.2405E 00
0.8	1.217	-0.2929E 00
0.6	1.280	-0.3223E 00
0.4	1.343	-0.2994E 00
0.2	1.394	-0.1915E 00

KR	OMEGA	V GROUP
5.0	2.006	-0.3206E-02
4.5	2.008	-0.4696E-02
4.0	2.011	-0.7124E-02
3.5	2.015	-0.1124E-01
3.0	2.022	-0.1847E-01
2.5	2.034	-0.3134E-01
2.0	2.055	-0.5178E-01
1.5	2.085	-0.6469E-01
1.0	2.106	0.3479E-02
0.8	2.099	0.6930E-01
0.6	2.078	0.1389E 00
0.4	2.046	0.1738E 00
0.2	2.014	0.1290E 00

KR	OMEGA	V GROUP
5.0	3.008	-0.4075E-02
4.5	3.010	-0.5737E-02
4.0	3.014	-0.8221E-02
3.5	3.019	-0.1189E-01
3.0	3.026	-0.1691E-01
2.5	3.036	-0.2174E-01
2.0	3.046	-0.1763E-01
1.5	3.048	0.1587E-01
1.0	3.028	0.5936E-01
0.8	3.016	0.5533E-01
0.6	3.007	0.3644E-01
0.4	3.002	0.1470E-01
0.2	3.000	0.2287E-02

KR	OMEGA	V GROUP
5.0	4.009	-0.4259E-02
4.5	4.012	-0.5630E-02
4.0	4.015	-0.7339E-02
3.5	4.019	-0.9095E-02
3.0	4.024	-0.9630E-02
2.5	4.028	-0.5243E-02
2.0	4.027	0.9762E-02
1.5	4.017	0.2762E-01
1.0	4.004	0.1842E-01
0.8	4.002	0.9626E-02
0.6	4.000	0.3306E-02
0.4	4.000	0.5835E-03
0.2	4.000	0.4143E-04

KR	OMEGA	V GROUP
5.0	5.010	-0.3802E-02
4.5	5.012	-0.4552E-02
4.0	5.014	-0.5050E-02
3.5	5.017	-0.4563E-02
3.0	5.018	-0.1552E-02
2.5	5.017	0.5749E-02
2.0	5.012	0.1451E-01
1.5	5.005	0.1317E-01
1.0	5.001	0.3263E-02
0.8	5.000	0.1059E-02
0.6	5.000	0.2033E-03
0.4	5.000	0.1907E-04
0.2	5.000	0.2682E-04

BERNSTEIN MODES - NUMERICAL SOLUTIONS

Density factor = 3.0

KR	OMEGA	V GROUP
5.0	1.009	-0.4760E-02
4.5	1.011	-0.6988E-02
4.0	1.016	-0.1065E-01
3.5	1.023	-0.1700E-01
3.0	1.034	-0.2873E-01
2.5	1.053	-0.5222E-01
2.0	1.090	-0.1041E 00
1.5	1.168	-0.2239E 00
1.0	1.333	-0.4505E 00
0.8	1.434	-0.5584E 00
0.6	1.556	-0.6582E 00
0.4	1.695	-0.7343E 00
0.2	1.847	-0.7704E 00

KR	OMEGA	V GROUP
5.0	2.016	-0.8764E-02
4.5	2.021	-0.1266E-01
4.0	2.029	-0.1888E-01
3.5	2.041	-0.2925E-01
3.0	2.060	-0.4722E-01
2.5	2.091	-0.7943E-01
2.0	2.143	-0.1350E 00
1.5	2.228	-0.2018E 00
1.0	2.326	-0.1436E 00
0.8	2.343	-0.6303E-02
0.6	2.323	0.2161E 00
0.4	2.255	0.4632E 00
0.2	2.142	0.6509E 00

KR	OMEGA	V GROUP
5.0	3.022	-0.1138E-01
4.5	3.029	-0.1594E-01
4.0	3.039	-0.2278E-01
3.5	3.052	-0.3310E-01
3.0	3.073	-0.4819E-01
2.5	3.101	-0.6667E-01
2.0	3.137	-0.7094E-01
1.5	3.159	0.6330E-02
1.0	3.109	0.1935E 00
0.8	3.067	0.2139E 00
0.6	3.029	0.1557E 00
0.4	3.007	0.6416E-01
0.2	3.000	0.9833E-02

KR	OMEGA	V GROUP
5.0	4.026	-0.1223E-01
4.5	4.033	-0.1626E-01
4.0	4.043	-0.2151E-01
3.5	4.055	-0.2759E-01
3.0	4.070	-0.3178E-01
2.5	4.085	-0.2396E-01
2.0	4.088	0.1868E-01
1.5	4.061	0.8886E-01
1.0	4.016	0.6702E-01
0.8	4.006	0.3500E-01
0.6	4.001	0.1187E-01
0.4	4.000	0.2062E-02
0.2	4.000	0.1594E-03

KR	OMEGA	V GROUP
5.0	5.028	-0.1127E-01
4.5	5.034	-0.1374E-01
4.0	5.042	-0.1582E-01
3.5	5.050	-0.1554E-01
3.0	5.056	-0.8142E-02
2.5	5.055	0.1385E-01
2.0	5.040	0.4544E-01
1.5	5.015	0.4454E-01
1.0	5.002	0.1098E-01
0.8	5.000	0.3536E-02
0.6	5.000	0.6729E-03
0.4	5.000	0.6020E-04
0.2	5.000	0.8762E-04

BERNSTEIN MODES - NUMERICAL SOLUTIONS

Density factor = 5.0

KR	OMEGA	V GROUP
5.0	1.013	-0.7185E-02
4.5	1.018	-0.1037E-01
4.0	1.024	-0.1547E-01
3.5	1.034	-0.2404E-01
3.0	1.049	-0.3929E-01
2.5	1.075	-0.6858E-01
2.0	1.123	-0.1305E 00
1.5	1.218	-0.2675E 00
1.0	1.409	-0.5119E 00
0.8	1.522	-0.6194E 00
0.6	1.656	-0.7041E 00
0.4	1.800	-0.7249E 00
0.2	1.935	-0.5681E 00

KR	OMEGA	V GROUP
5.0	2.026	-0.1338E-01
4.5	2.034	-0.1907E-01
4.0	2.045	-0.2802E-01
3.5	2.062	-0.4265E-01
3.0	2.089	-0.6763E-01
2.5	2.133	-0.1120E 00
2.0	2.207	-0.1901E 00
1.5	2.329	-0.3021E 00
1.0	2.500	-0.3469E 00
0.8	2.563	-0.2686E 00
0.6	2.599	-0.5409E-01
0.4	2.576	0.2802E 00
0.2	2.500	0.4051E 00

KR	OMEGA	V GROUP
5.0	3.035	-0.1769E-01
4.5	3.046	-0.2462E-01
4.0	3.061	-0.3502E-01
3.5	3.082	-0.5087E-01
3.0	3.113	-0.7487E-01
2.5	3.158	-0.1081E 00
2.0	3.220	-0.1345E 00
1.5	3.278	-0.6301E-01
1.0	3.234	0.2799E 00
0.8	3.164	0.4111E 00
0.6	3.080	0.3903E 00
0.4	3.020	0.1878E 00
0.2	3.001	0.2839E-01

KR	OMEGA	V GROUP
5.0	4.042	-0.1946E-01
4.5	4.054	-0.3596E-01
4.0	4.069	-0.3471E-01
3.5	4.089	-0.4565E-01
3.0	4.114	-0.5595E-01
2.5	4.142	-0.5196E-01
2.0	4.157	0.7987E-02
1.5	4.119	0.1500E 00
1.0	4.033	0.1396E 00
0.8	4.012	0.7360E-01
0.6	4.003	0.2457E-01
0.4	4.000	0.4190E-02
0.2	4.000	0.3064E-03

KR	OMEGA	V GROUP
5.0	5.046	-0.1846E-01
4.5	5.056	-0.2286E-01
4.0	5.068	-0.2712E-01
3.5	5.083	-0.2853E-01
3.0	5.095	-0.1942E-01
2.5	5.098	0.1562E-01
2.0	5.075	0.7724E-01
1.5	5.030	0.8447E-01
1.0	5.003	0.2083E-01
0.8	5.001	0.6637E-02
0.6	5.000	0.1253E-02
0.4	5.000	0.1109E-03
0.2	5.000	0.1836E-03

BERNSTEIN MODES - NUMERICAL SOLUTIONS

Density factor = 10.0

KR	OMEGA	V GROUP
5.0	1.023	-0.1152E-01
4.5	1.030	-0.1607E-01
4.0	1.040	-0.2305E-01
3.5	1.054	-0.3416E-01
3.0	1.075	-0.5286E-01
2.5	1.109	-0.8685E-01
2.0	1.167	-0.1554E 00
1.5	1.277	-0.3000E 00
1.0	1.484	-0.5345E 00
0.8	1.599	-0.6194E 00
0.6	1.729	-0.6585E 00
0.4	1.857	-0.6023E 00
0.2	1.959	-0.3855E 00

KR	OMEGA	V GROUP
5.0	2.045	-0.2188E-01
4.5	2.058	-0.3035E-01
4.0	2.076	-0.4321E-01
3.5	2.102	-0.6344E-01
3.0	2.141	-0.9669E-01
2.5	2.203	-0.1538E 00
2.0	2.302	-0.2525E 00
1.5	2.463	-0.3979E 00
1.0	2.696	-0.5115E 00
0.8	2.798	-0.5023E 00
0.6	2.893	-0.4296E 00
0.4	2.964	-0.2682E 00
0.2	2.997	-0.6433E-01

KR	OMEGA	V GROUP
5.0	3.063	-0.2992E-01
4.5	3.081	-0.3035E-01
4.0	3.105	-0.5738E-01
3.5	3.140	-0.8236E-01
3.0	3.190	-0.1211E 00
2.5	3.264	-0.1803E 00
2.0	3.373	-0.2584E 00
1.5	3.518	-0.3047E 00
1.0	3.637	-0.7456E-01
0.8	3.623	0.2407E 00
0.6	3.541	0.5318E 00
0.4	3.429	0.5359E 00
0.2	3.344	0.2831E 00

KR	OMEGA	V GROUP
5.0	4.077	-0.3452E-01
4.5	4.097	-0.4609E-01
4.0	4.124	-0.6228E-01
3.5	4.160	-0.8464E-01
3.0	4.210	-0.1132E 00
2.5	4.273	-0.1376E 00
2.0	4.338	-0.1033E 00
1.5	4.337	0.1675E 00
1.0	4.147	0.5033E 00
0.8	4.058	0.3514E 00
0.6	4.013	0.1203E 00
0.4	4.001	0.1873E-01
0.2	4.000	0.1410E-02

KR	OMEGA	V GROUP
5.0	5.085	-0.3481E-01
4.5	5.105	-0.4422E-01
4.0	5.130	-0.5529E-01
3.5	5.160	-0.6542E-01
3.0	5.194	-0.6406E-01
2.5	5.217	-0.1746E-01
2.0	5.193	0.1323E 00
1.5	5.089	0.2394E 00
1.0	5.010	0.6316E-01
0.8	5.002	0.1938E-01
0.6	5.000	0.3569E-02
0.4	5.000	0.3117E-03
0.2	5.000	0.3594E-03

Appendix II

The Analysis of Low-density Topside Ionograms

The reduction of topside ionograms taken in regions of space in which the plasma density near the vehicle is low introduces problems into N(h) analysis of both a theoretical and practical nature. Such ionograms show a very steep cusp on the X-trace at the low frequency end, corresponding to the wave travelling in a medium where its group velocity is extremely low, caused by the fact that f_{X_S} is only slightly above f_{H_S}. This condition is often met at night at low latitudes, and is very common over the polar caps. High altitude ionograms, such as those from Alouette II, will always show this effect. The theoretical problem consists of compensating adequately for variations in gyrofrequency with altitude, while the practical difficulty in analysis lies in the fact that the initial, near vertical section of the trace is often indistinct or absent, even though the remainder of the curve is perfectly clear. The result is generally a value of f_{X_S} which will almost certainly be in error, plus (h',f) pairs of normal accuracy from the cusp frequency upwards.

This appendix outlines the results of tests made on two N(h) programmes in use at Imperial College. More details, and the modifications made to one programme are given elsewhere (Andrews, 1969).

It is first necessary to construct a virtual depth profile. This has been done for the case of a pure exponential density versus height layer in the presence of a height dependent gyrofrequency $f_H(h)$. The latter feature necessitates some departures from the method outlined by Thomas and Westover (1963).

The plasma frequency f_N of the layer is related to the plasma frequency f_o at the satellite by

$$f_N^2 = f_o^2 \exp(h/H)$$

where h is the depth below the vehicle, and H the layer scale height, assumed constant. Define the corresponding frequency, f', by

$$f'^2 = f_x^2 - f_x f_H(h),$$

where f_x is the extraordinary wave frequency for which the virtual depth is required, and a quantity T by

$$T^2 = 1 - f_N^2(h)/f'^2(h) \qquad (A.1)$$

It can be shown that the virtual depth of reflection is given by

$$h'(f_x) = 2H \int_0^a \frac{G_x}{(1-T^2)\, z(h)}\, dT \qquad (A.2)$$

where $G_x = cT/v_g$, v_g being the X-ray group velocity

and $$z(h) = 1 + \frac{3Hf_x f_{Hs}}{7370\, f'(h)\, (1-h/7370)^4}$$

for a vehicle altitude of 1000 km. Expressions for G_x have been given by Becker (1960). The limits of the integration correspond to the height of the satellite, where T = a, and the point of reflection, T = 0. At each value of T, (A.1) must be solved for a depth h, before the weighting function z(h), containing the effect of the varying gyrofrequency, can be found.

Table A.1 gives the theoretically constructed (h',f) data pairs. The N(h) programme tests consisted of omitting the virtual depth of 1149.7 km on the near-vertical section of the trace, and varying the value of f_{x_s} above and below its true value of 1.0385 Mc/s to simulate a real ionogram. The results of the test are shown in Fig. A.1. Differences in the accuracies of the programmes lie entirely in the type of f_H compensation used. The contiguous parabola programme (Doupnik and Schmerling, 1965) compensated in continuous fashion for f_H variations; the Ames Research Centre overlapping polynomial programme used post reduction correction. The latter consists of evaluating the whole profile

TALLE A.1 - Virtual depths for test ionograms

Extra-ordinary wave Dip = 70° H = 200 km

Vehicle Height = 1000 km f_{H_s} = 1.0 Mc/s f_o = 0.20 Mc/s

Frequency, Mc/s	Depth, km	Frequency, Mc/s	Depth, km
1.0385	0.0	1.9000	1238.5
1.0685	1149.7	2.0000	1248.4
1.1185	1310.8	2.1000	1259.5
1.1685	1319.6	2.2000	1271.4
1.2000	1310.1	2.3000	1283.5
1.3000	1271.2	2.4000	1295.9
1.4000	1243.5	2.5000	1308.4
1.5000	1228.8	2.6000	1320.8
1.6000	1223.7	2.7000	1333.2
1.7000	1225.0	2.8000	1345.4
1.8000	1230.3		

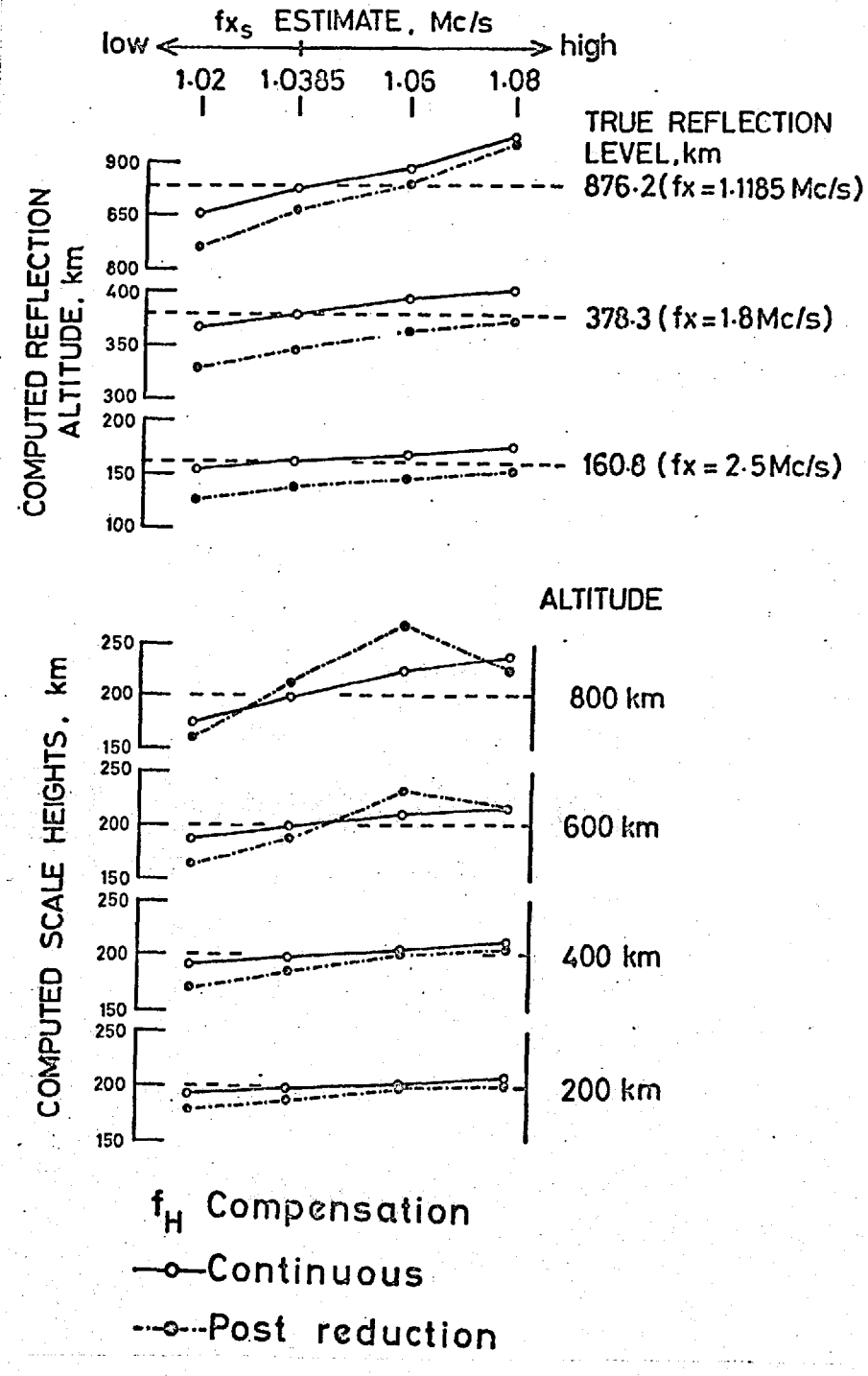


Fig. A.1 The results for different N(h) programmes in the ionogram tests, when f_{xs} was varied above and below its true value of 1.0385Mc/s. Differences are solely due to the type of f_H compensation used, and post reduction correction is clearly inadequate for such low density ionograms. Errors in the computed scale height due to an incorrect starting frequency are small below 600km.

assuming $f_H = f_{H_S}$ to obtain a set of real depths of reflection, after which the densities at these altitudes are recomputed using the true value of f_H at the reflection level. The gyrofrequency enters the computation in two places for the X-ray; in the limits of the virtual height integral, and in the group refractive index. The success of the post-reduction correction lies in the fact that these two errors very nearly cancel themselves under normal (mid-latitude) conditions, when the probing frequency f_x is not close to f_H. The overlapping polynomial programme has been extensively modified to incorporate the full f_H correction, which must be done on an iterative basis.

Referring to the figure, even when the correct points are used as input, post-reduction correction gives depths which are seriously in error, by typically 25 km, while the complete f_H compensation is unaffected by the omission of points on the near vertical portion of the trace. Clearly the latter type compensation is essential at high latitudes. When an error is introduced into the value f_{x_S}, the errors in the remainder of the profile are minimised with continuous f_H compensation, and significantly, they decrease with increasing reflection depth. By 600 km altitude, the error in the scale height produced by typical starting errors is only 10 km, or 5%, which is acceptably small.

It is concluded therefore that N(h) analysis is reliable under the conditions outlined at the start of this appendix, provided adequate allowances are made for the gyrofrequency variation, and sufficient points are read from the accurate portions of the trace to enable the profile computed to correct itself.

Publications

Changes in the topside ionosphere during a large magnetic storm.
Planet. Space Sci., 15, 1157, 1967,
J. E. Titheridge and M. K. Andrews.

Work based on this thesis:

The transpolar exospheric plasma, 1: Plasmasphere termination.
JGR, 73, 7407, 1968,
J. O. Thomas and M. K. Andrews.

Electron density distribution above the winter pole.
Nature, 221, 223, 1969,
M. K. Andrews and J. O. Thomas.

The transpolar exospheric plasma, 3: A unified picture.
Planet. Space Sci., 17, 433, 1969,
J. O. Thomas and M. K. Andrews.

Resonances observed by radio pulse sounders and their application to measurements in space.
Proc. Nato Advanced Study Institute, Røros 1968, Edinburgh University Press,
J. O. Thomas and M. K. Andrews.

References

Anderson, K. A., H. K. Harris and R. J. Paoli, JGR 70, 1039, 1965.

Andrews, M. K., Tests on and modification to a polynomial N(h) programme for the analysis of low density topside ionograms, Imperial College Report, March 1969.

Angerami, J. J. and J. O. Thomas, JGR 69, 4537, 1964.

Axford, W. I., Revs. Geophys. 7, 1-2, 421, 1969.

Banks, P. M., Plasma transport in the topside polar ionosphere, To appear in Proc. NATO A.S.I., Skeikampen, 1969.

Banks, P. M. and T. E. Holzer, JGR 73, 6846, 1968.

Banks, P. M. and T. E. Holzer, JGR 74, 3734, 1969.

Becker, W., Max-Plank-Institute Für Aeronome, No 4, 1960.

Bekefi, G. and E. B. Hooper, App. Phys. Lett. 4, 135, 1964.

Bellchambers, W. H., L. W. Barclay and W. R. Piggott, The Royal Society IGY Expedition Halley Bay 1955-59, 179, Roy. Soc., London, 1962.

Bennett, S. M. and T. M. Noel, p. 77 in Geomag. and Aeron., A.G.U. Ant. Res. Series 4, 1965.

Benson, R. F., NASA preprint X-612-67-287, June 1967.

Bernstein, I. B., Phys. Rev. 109, 10, 1958.

Block, L. P. and C. G. Fälthammar, JGR 73, 4807, 1968.

Bohme, D. K., P. P. Ong, J. B. Hasted and L. R. Megill, Planet. Sp. Sci. 15, 1777, 1967.

Bowen, P. J., R. L. F. Boyd, W. J. Raitt and A. P. Willmore, Proc. Roy. Soc. A281, 504, 1964.

Brace, L. H. and B. M. Reddy, JGR 70, 5783, 1965.

Buchsbaum, S. J. and A. Hasegawa, Phys. Rev. 143, 303, 1966.

Buckley, R., R.F. characteristics of a plane-grid capacitor immersed in a hot collision-free plasma with a uniform magnetic field parallel to the grid plates, R.S.R.S. preprint, Slough, 1968.

Bullen, J. M., J.A.T.P. 28, 879, 1966.

Burch, J. L., JGR 73, 3585, 1968.

Burch, J. L., Ph.D. Thesis, Rice University, Texas, 1968.

Burch, J. L., Aurora I observations of low energy particle fluxes over the poles. Paper presented at NATO A.S.I., Skeikampen, 1969.

Calvert, W., Proc. NATO A.S.I., Finse, Norway, 281, ed. J. Frihagen, North Holland, 1966.

Calvert, W. and G. B. Goe, JGR 68, 6113, 1963.

Carpenter, D. L., JGR 71, 693, 1966.

Clinckemaille, A., Propagation of longitudinal cyclotron plasma waves in a finite plasma column. Institut für Plasmaphysik report, Munich, 1968.

Cole, K. D., Aust. J. Phys. 16, 423, 1963.

Cole, K. D., Planet. Sp. Sci. 15, 873, 1967.

Coroniti, S. C. and R. Penndorf, JGR 64, 5, 1959.

Crawford, F. W., M. L. Rep. 1273, Stanford University, 1964.

Crawford, F. W., Nuc. Fusion 5, 73, 1965.

Crawford, F. W., Laboratory Plasma Wave Measurements, in Proc. NATO A.S.I., Røros 1968, Edinburgh University Press.

Crawford, F. W., R. S. Harp and T. D. Mantei, JGR 72, 57, 1967.

Crawford, F. W., G. S. Kino and H. H. Weiss, Phys. Rev. Lett. 13 (7), 229, 1964.

Dalgarno, A., J.A.T.P. 26, 939, 1964.

Dayharsh, T. I. and W. W. Farley, JGR 70, 5361, 1965.

Dessler, A. J. and P. A. Cloutier, JGR 74, 3730, 1969.

Dieminger, W., Sber. finn. Akad. Wiss. 199, 1959.

Donley, J. L., Observations of the polar ionosphere in the altitude range 2000 - 3000 km by means of satellite-borne electron traps, NASA preprint X-615-67-335, July 1967.

Dougherty, J. P. and J. J. Monaghan, Proc. Roy. Soc. London, A289, 214, 1965.

Doupnik, J. and E. Schmerling, J.A.T.P. 27, 917, 1965.

Duncan, R. A., JGR 67, 1823, 1962.

Dungey, J. W., Phys. Rev. Lett. 6, 47, 1961.

Dungey, J. W., The theory of the quiet magnetosphere, in Solar-Terrestrial Physics, p. 91, Academic Press, London, 1967.

Eather, R. H., JGR 74, 153, 1969.

Evans, J. E., R. G. Johnson, E. G. Joki and R. D. Sharp, Space Res. 6, 773, 1966.

Evans, J. E., R. G. Johnson, R. D. Sharp and J. B. Reagen, Sp. Sci. Rev. 7, 263, 1967.

Evans, J. V., Ground-based measurements of Atmospheric and Ionospheric particle temperatures, Chapter IX in Solar-Terr. Physics, ed. King and Newman, Academic Press, London, 1967.

Eviatar, A., A. M. Lenchek and S. F. Singer, Phys. Fluids 7, 1775, 1964.

Fejer, J. A. and W. Calvert, JGR 69, 5049, 1964.

Feldstein, Y. I., Geomag. Aeron. 3, 183, 1963.

Fite, W. L. and R. T. Brackman, Phys Rev. 113, 815, 1959.

Frank, L. A., J. A. van Allen and J. D. Craven, JGR 69, 3155, 1964.

Freeston, I. L., J. Plasma Physics 2 part 3, 329, 1968.

Gross, E. P., Phys. Rev. 82, 232, 1951.

Grün, A. E., Zeit. Für Naturforschung 12a, 89, 1959.

Hagg, E. L., Can. J. Phys. 45, 27, 1965.

Hagg, E. L., Nature 210, 927, 1966.

Hagg, E. L., Can. J. Phys. 45, 27, 1967.

Hakura, V., Rep. Ion. Sp. Res. Jap. 19, 121, 1965.

Harp, R. S., App. Phys. Lett. 6, 51, 1965.

Hartman, P. L., Planet. Sp. Sci. 16, 1315, 1968.

Hartz, T. R. and N. M. Brice, Planet. Sp. Sci. 15, 301, 1967.

Hill, G. E., J. Atmos. Sci. 20, 492, 1963.

Hinteregger, H. E. and K. Watanabe, JGR 67, 3373, 1962.

Hoffman, J. H., Trans. Am. Geophys. Union 49, 253, 1968.

Hoffman, R. A., JGR 74, 2425, 1969.

Holt, O. and G. M. Lerfald, Rad. Sci. 2 (11), 1283, 1967.

Holzer, T. E., Effects of plasma flow on density and velocity profiles in the polar ionosphere, To appear in Proc. NATO A.S.I., Skeikampen, 1969.

Johnson, T. W. and J. Nuttall, JGR 69, 2305, 1964.

Kamiyama, H., Science Rep. of the Tohuku University, Series 5, Geophysics 18, 1, July 1966a.

Kamiyama, H., Rep. Ion. Sp. Res. Jap. 20, 2, 1966b.

King, J. W., H. Kohl, D. M. Preece and C. Seabrook, J.A.T.P. 30, 11, 1968.

King, J. W. and D. M. Preece, J.A.T.P. 29, 1387, 1967

Knecht, R. W., JGR 64, 1243, 1959.

Knecht, R. W. and S. Russell, JGR 67, 1178, 1962.

Knecht, R. W., T. E. van Zandt and S. Russell, JGR 66, 3078, 1961.

Landau, L. D., J. Phys. Moscow, 10, 25, 1946.

Landauer, G., Proc. 5th Int. Conf. on ionisation phenomena in gases, 1, 389, 1961, North Holland, Amsterdam, 1961.

Landauer, G., J. Nuc. Energy C4, 395, 1962.

Landauer, G., Bull. Am. Phys. Soc. 9 (3), 312, 1964.

Liszka, L., J.A.T.P. 27, 1243, 1967.

Lockwood, G. E. K., Can. J. Phys. 41, 190, 1963.

Lund, D. S., R. D. Hunsucker, H. F. Bates and W. B. Murcray, JGR 72, 1053, 1967.

McAfee, J. R., JGR 74, 802, 1969.

McDiarmid, I. B. and J. R. Burrows, JGR 70, 3031, 1965.

McIwain, C., JGR 65, 2727, 1960.

Maeda, K., Diffusion of auroral electrons in the atmosphere, NASA TN D-2612, February 1965.

Maelhum, B. N., Geophys. Publ. 20, 6, 1958.

Maelhum, B. N., JGR 73, 3459, 1968.

Maelhum, B. N., On the high latitude, universal time controlled F-layer, To appear in J.A.T.P., 1969.

Mantei, T. D., SUIPR rep. 194, Stanford University, 1967.

Mariani, F., J. Atmos. Sci. 20, 479, 1963.

Mead, G. D., JGR 69, 1181, 1964.

Mead, G. D. and L. J. Cahill, JGR 72, 2737, 1967.

Meek, J. H., JGR 54, 339, 1949.

Muldrew, D. B., JGR 70, 2635, 1965.

Muldrew, D. B., Nature 210, 471, 1966.

Muldrew, D. B. and E. L. Hagg, Can. J. Phys. 44, 925, 1966.

Nelms, G. L., Results from the Alouette/ISIS topside sounders, To appear in Proc. NATO A.S.I., Skeikampen, 1969.

Nelms, G. L. and G. E. K. Lockwood, Early results from the topside sounder in the Alouette II satellite, paper presented at COSPAR, Vienna, 1966.

Nelms, G. L. and G. E. K. Lockwood, Sp. Res. 6, 604, 1967.

Nisbet, J. S., I.R.L. Rep. 194, Penn. State University, 1963.

Nishida, A., JGR 71, 5669, 1966.

Nishida, A., JGR 72, 6051, 1967.

Nishida, A., JGR 73, 1795, 1968.

Obayashi, T., J. Radio Res. Lab. 5, 213, 1958.

Oguti, T. and K. Marubashi, Rep. Ion. Sp. Res. Jap. 20, 96, 1966.

Olson, W. P., The tilted magnetopause; its shape and associated current system, McDonnell Douglas preprint 10168, February 1969.

Parker, E. N., The dynamical theory of gases and fields in interplanetary space, Chapter II in Solar-Terr. Physics, ed. King and Newman, Academic Press, London, 1967.

Patton, D. E., V. L. Peterson, G. H. Stonehocker and J. W. Wright, p 47 in Geomag. and Aeron., Ant. Res. Series 4, AGU 1965.

Pavkovitch, J. and G. S. Kino, R.F. theory of plasma sheaths, Proc. 6th Int. Conf. on ionisation phenomena in gases, Paris, 3, 39, 1963.

Penndorf, R., p 1 in Geomag. and Aeron., Ant. Res. Series 4, AGU 1965.

Ranzi, I., Proc. XII Gen. Assembly URSI, XI, 3, 1957.

Rastogi, R. G. JGR 65, 585, 1960.

Reber, C. A. and M. Nicolet, Planet. Sp. Sci. 13, 617, 1965.

Rees, M. H., Planet. Sp. Sci. 11, 1209, 1963.

Rees, M. H., Planet. Sp. Sci. 12, 722, 1964.

Rees, M. H., Effects of low energy particle precipitation on the upper atmosphere, To appear in Proc. NATO A.S.I., Skeikampen, 1969.

Rothwell, P., Space Res. V, p 635, North Holland, Amsterdam, 1965.

Rycroft, M. J. and J. O. Thomas, The magnetospheric plasmapause and the electron density trough at the Alouette I orbit, Preprint, 1967.

Sandford, B. P., Optical emissions over the polar cap, To appear in Proc. NATO A.S.I., Skeikampen, 1969.

Sato, T., Rep. Ion. Sp. Res. Jap. 13, 91, 1959.

Sato, T. and L. Colin, JGR 74, 2193, 1969.

Sato, T. and G. F. Rourke, JGR 69, 4591, 1964.

Sayers, J., Proc. Roy. Soc. A281, 450, 1964.

Schield, M. A., J. W. Freeman and A. J. Dessler, JGR 74, 247, 1969.

Schmeltekopf, A. L., F. C. Fehsenfeld, G. I. Gilman and E. E. Ferguson, Planet. Sp. Sci. 15, 401, 1967.

Sharp, G. W., JGR 71, 1345, 1966.

Sharp, R. D., D. L. Carr and R. G. Johnson, Satellite observations of the average properties of auroral particles, Preprint 1969.

Smith, P. A. and B. A. Kaiser. J.A.T.P. 29, 1345, 1967.

Stix, T. H., The theory of plasma waves, McGraw-Hill, New York, 1962.

Tanaka, S., Y. Terumichi, K. Mitani and H. Kubo, J. Phys. Soc. Jap. 18 (12), 1810, 1963.

Tataronis, J. A., S.U.I.P.R. Report 205, Stanford University, December 1967.

Thomas, J. O., NASA Ames Research Center Note, 1964.

Thomas, J. O. and M. K. Andrews, Proc. NATO A.S.I., Røros 1968, Edinburgh Univ. Press.

Thomas, J. O. and S. W. Dufour, Nature 206, 567, 1965.

Thomas, J. O., M. J. Rycroft, L. Colin and K. L. Chan, Proc. NATO A.S.I. Finse, Norway (Ed. J. Frihagen) p 322, North Holland, Amsterdam, 1966.

Thomas, J. O. and A. Y. Sader, Alouette topside soundings monitored at Stanford University, S.E.L. rep. no. 6, 1963.

Thomas, J. O. and A. Y. Sader, JGR 69, 4561, 1964.

Thomas, J. O. and D. Westover, Stanford University Tech. Rep. S.E.L. - 63 - 130, 1963.

Thomas, L. and R. B. Norton, JGR 71, 227, 1966.

Titheridge, J. E., JGR 73, 2985, 1968.

Titheridge, J. E. and G. F. Stuart, J.A.T.P. 30, 85, 1968.

Torr, M. R. and D. G. Torr, A theoretical investigation of the F-region of the ionosphere, C.S.I.R. Rep. 271, Pretoria, South Africa, 1969.

Warren, E. S. and E. L. Hagg, Nature 220, 466, 1968.

Wharton, C. B., Proc. 4th International Conf. on ionisation phenomena in gases, Uppsala, 1959, 2, 737, North Holland, Amsterdam, 1960.

Yngvesson, K. O. and F. W. Perkins, JGR 73, 97, 1968.

Yonezawa, T., Sp. Sci. Rev. 5, 3, 1966.